

UNIVERSITY OF CALIFORNIA, SAN DIEGO

**Electromagnetic and Kinetic Effects on Blob-filamentary Plasma Structures in Magnetic
Confinement Devices**

A Dissertation submitted in partial satisfaction of the
requirements for the degree
Doctor of Philosophy

in

Engineering Sciences (Engineering Physics)

by

Wonjae Lee

Committee in charge:

Professor Sergei I. Krasheninnikov, Chair
Professor Farhat Beg
Professor Patrick Diamond
Professor Dan Dubin
Professor Daniel Tartakovsky

2017

Copyright
Wonjae Lee, 2017
All rights reserved.

The Dissertation of Wonjae Lee is approved, and it is acceptable in quality and form for publication on microfilm and electronically:

Chair

University of California, San Diego

2017

DEDICATION

To Sangmi.

EPIGRAPH

“Try not to become a man of success,

but rather try to become a man of value.”

—Albert Einstein

TABLE OF CONTENTS

Signature Page	iii
Dedication	iv
Epigraph	v
Table of Contents	vi
List of Figures	viii
Acknowledgements	xi
Vita	xiii
Abstract of the Dissertation	xv
Chapter 1 Introduction	1
1.1 Nuclear fusion	1
1.2 Tokamak and divertor	3
1.3 Plasma filamentary structure: blobs	4
1.4 Drift wave instability and blob dissipation	6
1.5 Dissertation Outline	7
1.5.1 Ch 2: Electromagnetic effects on dynamics of high-beta filamentary structures	9
1.5.2 Ch. 3: Electromagnetic drift wave dispersion for arbitrarily collisional plasma	10
1.5.3 Ch. 4: Verification of 5D continuum gyrokinetic code COGENT: studies of kinetic drift wave instability	11
Chapter 2 Electromagnetic effects on dynamics of high-beta filamentary structures	12
2.1 Introduction	13
2.2 Governing equations, initial and boundary conditions	14
2.2.1 Governing equations	14
2.2.2 Initial and boundary conditions	17
2.3 Electromagnetic effects on blob propagation	19
2.3.1 Electromagnetic effects and sheath boundary condition	19
2.3.2 Electromagnetic effects and inhomogeneous polarization	21
2.4 Electromagnetic effects on blob stability	27
2.5 Discussion	36
2.6 Conclusion	39

Chapter 3	Electromagnetic Drift Waves Dispersion for Arbitrarily Collisional Plasmas	41
3.1	Introduction	42
3.2	Model Equations and Derivation of Dispersion Relations	45
3.2.1	Kinetic description of electrons	46
3.2.2	Fluid description of electrons in collisional limit	50
3.2.3	Kinetic Description of Ions	52
3.2.4	Dispersion Relation and Normalization	54
3.3	Electromagnetic effects and Landau resonance	55
3.4	Finite ion temperature and stabilization of drift wave instability	59
3.5	Conclusion	62
Chapter 4	Verification of 5D continuum gyrokinetic code COGENT: studies of kinetic drift wave instability	64
4.1	Introduction	65
4.2	Development of 3D2V Gyrokinetic continuum code	66
4.2.1	Gyrokinetic equation set	66
4.3	Modeling drift-wave instability: simulation set-up	67
4.4	Result of numerical simulations	73
4.5	Conclusion	74
Chapter 5	Summary	79
Appendix A	Derivation of Eq. (3.4)	82
Appendix B	Dispersion equation for electromagnetic fluid equations with Landau closure	84
Appendix C	Mass Dependent Normalization and Velocity Space Truncation	90
Appendix D	Derivation and numerical solution of dispersion relation, Eq. (4.7)	95
Appendix E	Temperature dependent normalization for COGENT	101
Bibliography	104

LIST OF FIGURES

Figure 1.1: Schematic diagram of a tokamak with a divertor	4
Figure 1.2: Blob creation and propagation in the SOL of the NSTX tokamak.	5
Figure 1.3: Comparison of density contours from 2D (top) and 3D (bottom) simulation.	8
Figure 2.1: Comparison of the sheath limited high- β blob evolution from electromagnetic and electrostatic calculation for balanced size blob ($\delta/\delta_* = 1$).	20
Figure 2.2: Comparison of the dipole potential strength in the sheath limited high- β blobs for electromagnetic and electrostatic calculation.	21
Figure 2.3: Evolution of density (\tilde{n}/n_0) for the high- β filament in the varying curvature along the field line from electromagnetic (top) and electrostatic (bottom) calculations.	23
Figure 2.4: Comparison of the dipole potential evolution for (a) electromagnetic and (b) electrostatic calculation on high- β filament submerged in the inhomogeneous curvature field.	24
Figure 2.5: Evolution of parallel current ($j_{\parallel} \equiv J_{\parallel}/J_0$) for the high- β filament in the varying curvature along the field line from electromagnetic (top) and electrostatic (bottom) calculations.	25
Figure 2.6: Magnetic field line bending for the high- β filament in the varying curvature along the field line from electromagnetic calculation.	27
Figure 2.7: Normalized growth rate $\gamma/\hat{\omega}_*$ as function of Ω_A and χ for two different models: electromagnetic (EM) and electrostatic (ES) calculation.	31
Figure 2.8: Blob density (\tilde{n}/n_0) contours of high-beta plasma from EM (top) and ES (bottom) models.	32
Figure 2.9: Contour lines of normalized maximum growth rate as function of resistivity and $\tilde{\beta}^{-1}$ and a line (dotted) $k_{\parallel}\lambda_e = 1$ with respect to $\Omega_A(\gamma_{\max})$.	33
Figure 2.10: Contour lines of normalized real frequency of the corresponding maximum growth rate as function of resistivity and $\tilde{\beta}^{-1}$.	34
Figure 2.11: Maximum normalized growth rate $\gamma/\hat{\omega}_*$ as a function of resistivity parameter Ω_R for electromagnetic blobs of four different values of $\tilde{\beta}^{-1} = 0.1, 1.0, 10, 100$ and electrostatic blob with electron inertia neglected (blue solid line).	35
Figure 2.12: Stochastic magnetic field lines are calculated during the electron inertial instability with slightly reduced $\tilde{\beta}$.	38

Figure 3.1: Plasma regimes for drift wave instabilities in different beta, $\tilde{\beta}_e = 8\pi n T_e M_i / (B^2 m_e)$ and collisionality, $\hat{v} = 2v\delta/c_s$.	44
Figure 3.2: Contour plots of normalized maximum growth rates, $\hat{\gamma}_{\max}$, for (a) EM fluid model, (b) EM kinetic collisionless model, (c) EM kinetic with arbitrary collision model, (d) ES fluid model, (e) ES kinetic collisionless model and (f) ES kinetic with arbitrary collision model.	56
Figure 3.3: Contour plots of real frequency at the maximum growth rate for (a) EM fluid model, (b) EM kinetic collisionless model, (c) EM kinetic with arbitrary collision model, (d) ES fluid model, (e) ES kinetic collisionless model and (f) ES kinetic with arbitrary collision model.	58
Figure 3.4: Contour plots of normalized maximum growth rates, $\hat{\gamma}_{\max}$, for electromagnetic (EM) models.	61
Figure 3.5: The ratio of estimated turbulent diffusivity of EM kinetic model to that of EM fluid mode for $T_i/T_e = 1$. The turbulent diffusivity is estimated by $D \simeq \gamma_{\max}/k_{\perp}^2$.	62
Figure 4.1: Illustration of 5D phase space mesh.	68
Figure 4.2: Implementation of a 5D phase space in COGENT. (a) Electron density distribution in the 3D configuration space. The electron density are normalized to $n_0 = 10^{20} \text{ m}^{-3}$. Normalization number (ref_t) for the time variable is $5.11 \times 10^{-6} \text{ s}$.	69
Figure 4.3: Implementation of a 5D phase space in COGENT. Electron distribution function in the 2D velocity space.	70
Figure 4.4: Example of initial density perturbation with second harmonics in y and z direction. The first harmonic perturbations are used in the simulation. The amplitude of perturbation is exaggerated for visualization.	71
Figure 4.5: 3D electrostatic potential distribution normalized to $\phi_0 = 400\text{V}$. The normalization number (ref_t) for the time variable is $5.11 \times 10^{-6} \text{ s}$.	72
Figure 4.6: Evaluation of the linear growth rate (red line) from the potential perturbation history (blue curve) obtained in the COGENT simulations of the drift wave instability.	73
Figure 4.7: COGENT simulations results compared to the analytical predictions in Eq. (4.7) without collisions.	75
Figure 4.8: COGENT simulations results compared to the analytical predictions in Eq. (4.7): includes the effects of electron collisions described by the Krook model.	76

Figure 4.9: Pronounced deviations of the electron distribution function from the Maxwellian background are observed for the collisionless case near the drift-wave phase velocity due to wave-particle resonance.	76
Figure 4.10: Development of the collisionless drift wave instability on a blob-filamentary plasma structure extended along the magnetic field lines. Plotted is the normalized plasma density iso surfaces.	77
Figure 4.11: Development of helical electrostatic potential perturbations inside the blob-filamentary structure. The helical perturbations rotate around the blob axis with the electron drift speed.	78
Figure B.1: Contour plots of maximum growth rate for (a) electromagnetic (EM) fluid model, (b) EM Landau fluid model, (c) EM kinetic with arbitrary collision model, (d) electrostatic (ES) fluid model, (e) ES Landau fluid model and (f) ES kinetic with arbitrary collision model.	88
Figure B.2: Contour plots of normalized maximum growth rates, $\hat{\gamma}_{\max}$, for electromagnetic (EM) models.	89
Figure C.1: A sample mesh of velocity space for a continuum gyrokinetic code.	93
Figure C.2: A sample Maxwellian distribution function deposited in a velocity space grid. .	93
Figure C.3: The complementary error function from the truncated Maxwellian distribution function.	94
Figure D.1: Magnetic field vector, \mathbf{B} , and the decomposition of wave vector, \mathbf{k}	96
Figure D.2: An example of root finding for dispersion relation. The positions of the circles represent complex solutions of the dispersion relation for given wave numbers. The closed circle corresponds to the solution with the highest growth rate.	99
Figure D.3: A contour plot depicts imaginary roots of dispersion relation for given perpendicular and parallel wave numbers.	100

ACKNOWLEDGEMENTS

Firstly, I would like to express my sincere gratitude to my advisor Prof. Krasheninnikov for the continuous support of my Ph.D study and related research, for his patience, motivation, and immense knowledge. His guidance helped me in all the time of research and writing of this thesis. I could not have imagined having a better advisor and mentor for my Ph.D study.

Besides my advisor, I would like to thank the rest of my thesis committee: Prof. Beg, Prof. Diamond, Prof. Dubin, and Prof. Tartakovsky for their insightful comments and encouragement.

My sincere thanks also goes to Dr. Umansky, Dr. Angus, Dr. Dorf, Dr. R. Cohen, Dr. Rognlien, Dr. Dorr and Dr. B. Cohen who provided me an opportunity to join their team as Lawrence scholar. Without their precious support it would not be possible to conduct this research.

I would like to thank my English tutor, Mr. Erenfeld, for coming to UCSD to teach me English every Wednesday for years. Last but not the least, I would like to thank my family: my parents and to my sisters. In particular, I am grateful to my wife for enlightening and for supporting me spiritually throughout writing this thesis and my life in general.

Chapter 2, in full, is a reprint of the material as it appears in *Electromagnetic effects on dynamics of high-beta filamentary structures* in Physics of Plasmas 22, 012505 by Wonjae Lee, Maxim V. Umansky, J. R. Angus, and Sergei I. Krasheninnikov, 2015. The dissertation author was the primary investigator and author of this paper.

Chapter 3, in full, is a reprint of the material as it appears in *Electromagnetic drift waves dispersion for arbitrarily collisional plasmas* in Physics of Plasmas 22, 072113 by Wonjae Lee, J. R. Angus, and Sergei I. Krasheninnikov, 2015. The dissertation author was the primary investigator and author of this paper.

Chapter 4, in full, is a reprint of the material as it appears in *Verification of 5D continuum gyrokinetic code COGENT: studies of kinetic drift wave instability* submitted in Contribution

to Plasma Physics, 2017, by Wonjae Lee, M.A. Dorf, M.R. Dorr, R.H. Cohen, T.D. Rognlien, J.A. Hittinger, M.V. Umansky, and S.I. Krasheninnikov. The dissertation author was the primary investigator and author of this paper.

VITA

2009	B. S. in Nuclear Engineering <i>summa cum laude</i> Seoul National University, Seoul, South Korea
2011	M. S. in Energy System Engineering Seoul National University, Seoul, South Korea
2012	Jacobs Fellow University of California, San Diego, La Jolla, CA
2013-2016	Graduate Research Assistant Sergei Krasheninnikov's group Department of Mechanical and Aerospace Engineering University of California, San Diego, La Jolla, CA
2014	Teaching Assistant MAE118: Introduction to Energy Systems Department of Mechanical and Aerospace Engineering University of California, San Diego, La Jolla, CA
2015-2017	Livermore Graduate Scholar Lawrence Livermore National Laboratory, Livermore, CA
2017	Ph. D. in Engineering Sciences (Engineering Physics), University of California, San Diego, La Jolla, CA

PUBLICATIONS

Secondary electron emission and the bifurcation of the heat flux to the targets in fusion plasmas, Wonjae Lee, Sergei I. Krasheninnikov, Physics of Plasmas 20, 122501 (2013).

Electromagnetic effects on plasma blob-filament transport, Wonjae Lee, J.R. Angus, Maxim V. Umansky, Sergei I. Krasheninnikov, , Journal of Nuclear Materials 463, 765 (2014)

Physics of the edge plasma and first wall in fusion devices: Synergistic effects, Sergei I. Krasheninnikov, A. Pigarov, Wonjae Lee, Plasma Physics and Controlled Fusion 57, 044009 (2015)

Electromagnetic effects on dynamics of high-beta filamentary structures, Wonjae Lee, Maxim V. Umansky, J. R. Angus, Sergei I. Krasheninnikov, Physics of Plasmas 22, 012505 (2015)

Electromagnetic drift waves dispersion for arbitrarily collisional plasmas, Wonjae Lee, J. R. Angus, Sergei I. Krasheninnikov, Physics of Plasmas 22, 072113 (2015)

Observation of the intrinsic rotation in KSTAR Ohmic L-mode plasmas, D.H. Na, Yong-Su Na, S.G. Lee, C. Angioni, S.M. Yang, H.-S. Kim, T.S. Hahm, W.H. Ko, H. Jhang, W.J. Lee and KSTAR Team, Nuclear Fusion 56, 036011 (2016)

Edge and divertor plasma: detachment, stability, and plasma-wall interactions, S.I. Krasheninnikov, A.S. Kukushkin, Wonjae Lee, A.A. Phsenov, R.D. Smirnov, A.I. Smolyakov, A.A. Stepanenko and Yanzeng Zhang, Nuclear Fusion 57, 102010 (2017)

Macroscopic motion of sheath-connected blobs in magnetic fields with arbitrary topology, A.A. Stepanenko, Wonjae Lee, S.I. Krasheninnikov, Physics of Plasmas 24, 012301 (2017)

Dynamics of sheath-connected plasma filaments in magnetic field with arbitrary geometry, A.A. Stepanenko, Wonjae Lee, S.I. Krasheninnikov, Nuclear Materials and Energy 12, 887 (2017)

Verification of 5D continuum gyrokinetic code COGENT: studies of kinetic drift wave instability Wonjae Lee, M.A. Dorf, M.R. Dorr, R.H. Cohen, T.D. Rognlien, J.A. Hittinger, M.V. Umansky, and S.I. Krasheninnikov, Contribution to Plasma Physics, submitted (2017)

ABSTRACT OF THE DISSERTATION

Electromagnetic and Kinetic Effects on Blob-filamentary Plasma Structures in Magnetic Confinement Devices

by

Wonjae Lee

Doctor of Philosophy in Engineering Sciences (Engineering Physics)

University of California, San Diego, 2017

Professor Sergei I. Krasheninnikov, Chair

Plasma blobs (filamentary structures extended along the magnetic field lines) are meso-scale turbulent structures that are usually observed in the scrape-off layer (SOL) of magnetic confinement devices. Electromagnetic fluid simulations for seeded high-beta blobs demonstrate that inhomogeneity of magnetic curvature or plasma pressure along the filament leads to bending of the filaments and magnetic field lines due to increased Alfvén time. Moreover, the drift wave instabilities inside the filaments are modified by electromagnetic effects. A local linear analysis on an electromagnetic drift-kinetic equation with BGK-like collision operator proves to be valid for describing the linear growth rate of drift wave instabilities in a wide range of plasma parameters

showing convergence to reference models for limiting cases. Finally, the development of the 5D version of the full-f gyrokinetic code COGENT and its application to the collisionless drift wave simulation are presented with discussion of the disturbance of the distribution function from the collisionless drift wave instability and the formation of a helical mode structure within the plasma filament.

Chapter 1

Introduction

1.1 Nuclear fusion

Controlled nuclear fusion could be the ultimate energy source to substitute traditional fossil fuels [1, 2, 3]. Fusion energy can address many of the shortcomings of conventional fossil fuels, such as carbon dioxide generation, global climate change, sea level rise, public pollution, and finite fuel reserves [4, 5]. Moreover, unlike other non-fossil fuel energy sources, such as wind, solar / photovoltaic and nuclear fission energy, nuclear fusion energy has the following advantages [1]:

- Fusion energy is less dependent on climate and location than wind or solar energy.
- Fusion power generation requires less space than solar or wind energy generation because of its high energy density.
- Fusion power generation is inherently safer than nuclear fission power generation because it does not use chain reactions with a critical mass.
- The half-life of radioactive waste generated by fusion reactions is shorter than that of the fission reactions.

In a fusion reaction, two or more nuclei are fused together in a collision to form heavier nuclei and other reaction products. The fusion energy is released owing to the difference between the initial binding energy and the final binding energy of the nuclear components. The difference in binding energy released during a fusion reaction is related to the difference in the rest mass of the reactant components and products [1, 3]. In other words, the mass sum of the fusion reaction products is smaller than that of the reactants causing the fusion, and the difference is released as the kinetic energy of the reaction products, depending on the mass-energy equivalence relation ($\Delta E = \Delta mc^2$).

In order to initiate the fusion reaction, positively charged nuclei must have sufficiently high energy and they must be kept in a space where they can collide with each other. Even the easiest fusion reaction (deuterium-tritium fusion) requires an energy in the order of 10 keV, which is equivalent to 100 million degrees Celsius [3]. At this high temperature, the reaction atoms are almost fully ionized, and unbounded electrons and nuclei are mixed together forming a ‘plasma’ state [6, 7, 8, 9]. As a method of maintaining the high-temperature plasma, a magnetic fusion approach has been studied extensively [2]. The magnetic fusion approach is a method of applying a magnetic field to plasma, so that the charged particles constituting the plasma are subjected to the Lorentz force. The charged particles will have a cyclotron motion with a radius that is inversely proportional to the magnetic field intensity in the direction perpendicular to the magnetic field, but are free to move in the direction parallel to the magnetic field. Therefore, magnetic confinement devices having a donut-like toroidal magnetic field shape have been considered to minimize the particle loss along the open field lines.

1.2 Tokamak and divertor

Among toroidal magnetic confinement devices, one of the most promising devices is a tokamak [10]. A typical schematic diagram of a tokamak is shown in Fig.1.1. To meet both the radial pressure balance and the toroidal force balance, the plasma equilibrium requires a helical magnetic field, which is the combination of the toroidal magnetic field supplied by external magnet coils and the poloidal magnetic field induced mainly by the plasma current in the toroidal direction [10, 11].

In addition, most modern tokamak devices have divertor configurations (see Fig. 1.1). The divertor configuration is created by an extra coil that creates a null point of the poloidal magnetic field near the edge plasma [10, 12]. Then, plasma in a tokamak is divided into the region of dense and hot core plasma with closed magnetic fluxes and the region of scrape-off layer (SOL) plasma with open magnetic fluxes. The particles and energy from the core plasma exiting the last closed flux surface flow along the open magnetic field lines in the SOL region and are deposited on the divertor target plates where magnetic field lines intersect. Because the divertor plates are located remotely from the closed flux surfaces, the diverted configuration is good for isolating the plasma core from impurities coming from the material surface. The use of the diverter configuration facilitates easier access to a high-confinement (H-mode) operation, which increases the energy confinement time, τ_E , by a factor of two [13]. Moreover, there have been recent studies on improving the divertor configurations (super-x [14] and snow-flake divertors[15]) to solve problems such as concentration of divertor heat load and inward diffusion of high-z impurities.

However, despite the divertor configuration design, the radial flux in the SOL plasma region is dominated by turbulent (anomalous) transport, which is much faster than neoclassical or collisional diffusion processes. Thus, the heat exhaust from the core plasma, and hence, the plasma-material interaction are not only concentrated on the divertor target, but also on the tokamak main vessel wall (first wall) and RF antennae components. The degradation of the first wall material, which is located

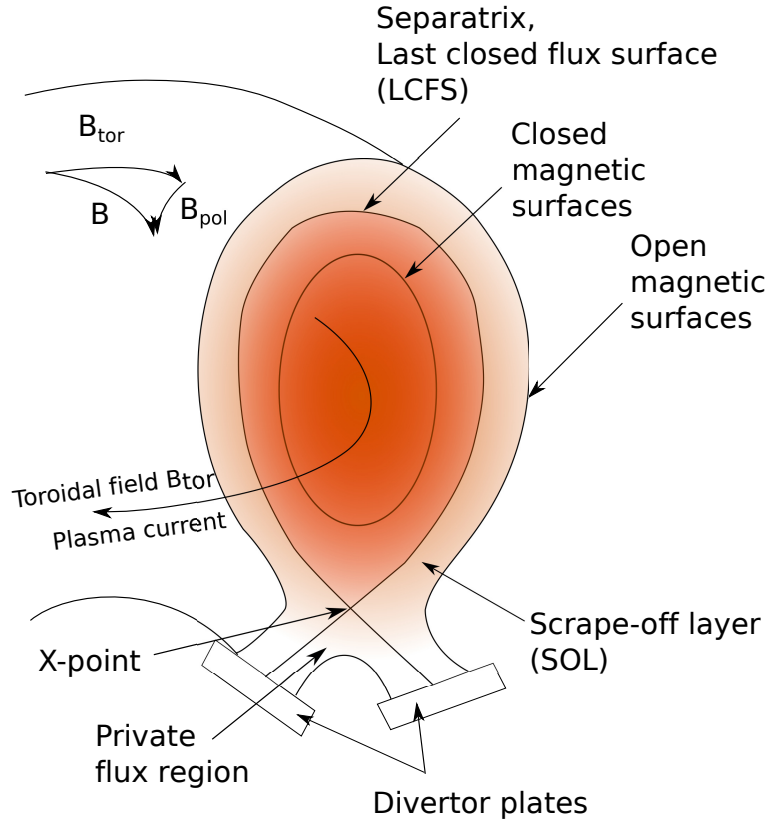


Figure 1.1: Schematic diagram of a tokamak with a divertor

closely to the core plasma, and sputtered impurity particles from the wall material, adversely affect both integrity of the tokamak components and performance of fusion grade plasma.

1.3 Plasma filamentary structure: blobs

Thorough studies in the last decade clearly demonstrated that most of anomalous transport fluxes in the SOL region, and thus enhanced plasma-wall interactions at the first wall, are caused by radial advection of coherent filamentary structures [16, 17, 18]. These structures are called “blobs” because of their cross-sectional shape on the drift plane. These structures are also called “filaments” or “blob-filaments” because of their three-dimensional thin filamentary shape aligned along the magnetic field lines [18]. Experimentally, the plasma filaments corresponding to plasma fluctuations

in the SOL region are observed intermittently in time and space, and this coherent fluctuation is known to be formed by the nonlinear saturation of the turbulence [19]. Plasma filaments are also referred to as mesoscale turbulent structures because of their cross-sectional size ($\sim 1\text{-}3$ cm), which is larger than the size of gyroradius (microscale) and smaller than the confinement scale length (macroscale). The filamentary structure is identified by its enhanced plasma density, which is (typically 2-3 times) larger than the surrounding background plasma density [18].

Plasma filaments are aligned along the magnetic field lines and observed in boundary plasma regions of various types of magnetic confinement devices including tokamaks [20, 21], stellarators [22], and linear plasma devices [23]. Figure 1.2 shows an example of blob propagation observed in the SOL of the NSTX tokamak [24].

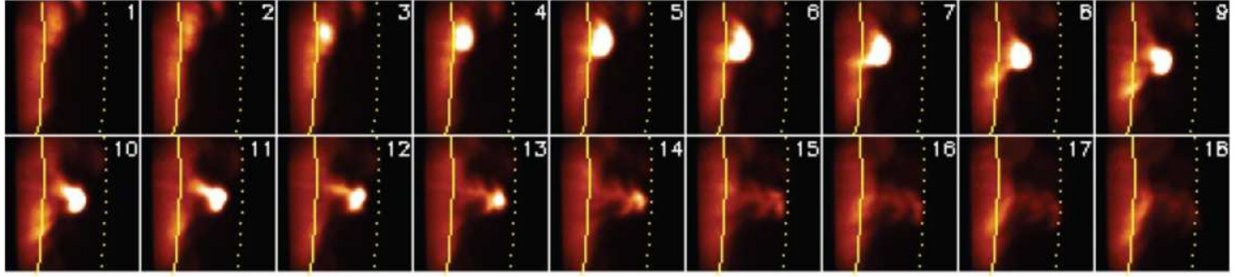


Figure 1.2: Blob creation and propagation in the SOL of the NSTX tokamak [24]. The images are produced from GPI diagnostics. The radius of the blob is approximately ~ 2 cm, and the propagation speed is in the order of ~ 1 km/s.

The filamentary structures are expelled from the plasma bulk and ballistically propagate towards the wall with their speed reaching several percent of the plasma sound speed. This motion of a coherent structure is important for the SOL transport, because the process by which the plasma blob convects across the thin SOL has a shorter time scale than that when the plasma flows along the SOL to reach the divertor target plate.

Therefore, the plasma blob is the ingredient of the turbulence structure that explains the phenomenon of radial anomalous transport in the SOL region. As an example, the “main chamber

recycling regime,” in which the plasma flow at the SOL is dominated by the radial convective motion of the plasma filament rather than the divertor target, is found in the Alcator C-Mod tokamak [25]. In addition, in the DIII-D tokamak, it was experimentally found that about 50 % of the SOL transport is due to the blob convection [26, 27].

The basic theory of the cross-field convective motion of a plasma blob was introduced in Ref. [16]. Comprehensive reviews on blobs can be found in Refs. [18] and [17]. The charge separation caused by effective gravity (i.e., curvature and grad(B) effects) results in a radial ExB convection of plasma. A simple model describing the dynamics of these plasma filaments consists of a vorticity equation and a density continuity equation derived from the laws of conservation of charge and density, respectively [17]. The vorticity equation describes the balance of the polarization current fed from the curvature and Grad(B) force by the parallel loss and vorticity increase in the plasma filament. For any given polarization force, the ExB convection velocity due to the dipole charge polarization accumulated in the blob is determined by the parallel current flowing along the filament and has different transport characteristics depending on the model describing the parallel current [17, 28]. For example, in the sheath connected closure model, which is known as the simplest model of parallel current, the current flowing through the filament is limited to the current through the sheath. In this case, the blob deformation according to the blob velocity scaling depends on the blob size and represents a mushroom-like deformation, finger-like deformation, or a balanced shape during the blob propagation [28].

1.4 Drift wave instability and blob dissipation

The drift wave is a kind of an ion acoustic wave that shows a three-dimensional structure existing in magnetized nonuniform plasma [29, 30, 8]. The wave exhibits a phase moving at the electron diamagnetic drift speed in the binormal direction of the magnetic field and the plasma

density gradient. This drift wave is important in magnetized fusion plasma because the wave becomes unstable easily because of the phase shift between the potential and the density perturbations by either electron collisions or wave-particle interactions [8]. When the electron collision is the onset mechanism, drift wave instability is called resistive drift wave instability (RDWI), whereas if the wave-particle interaction is the onset mechanism, it is called collisionless drift wave instability or universal instability.

Drift waves are also important for blob stability because the microscale drift wave perturbation inside the blob-filaments can become unstable and dissipates the blob structure. In particular, a recent study of the impact of plasma instabilities on blob dynamics within the electrostatic fluid approximation shows that the coherency of a blob can be substantially limited by the onset of the RDWI, resulting in blobs dispersion [28]. This means that blobs can lose their radial advection drive by the instability mechanism before they arrive at the surface of the wall material. Figure (1.3) from Ref. [28] demonstrates this phenomenon well. The drift wave is not simulated from a 2D simulation (Fig. 1.3(top)) due to the lack of the wave vector along the magnetic field direction, whereas in a 3D simulation (Fig. 1.3(bottom)), the original blob shape and the polarization drive are lost due to RDWI.

1.5 Dissertation Outline

Despite the growing interest in dynamics of blobs, most of previous studies on blob filaments have been limited to the electrostatic approximation [31, 32, 33, 34, 35, 36, 28, 37, 38], which is only adequate for low beta ($\beta = 8\pi p/B^2 < m_e/m_i$) plasmas. The electromagnetic effects are envisioned to be particularly important for future magnetic confinement devices, such as International Thermonuclear Experimental Reactor (ITER) and DEMOnstration Power Station (DEMO). In the large machines, the impact of particles and heat transported by blobs to plasma-facing components

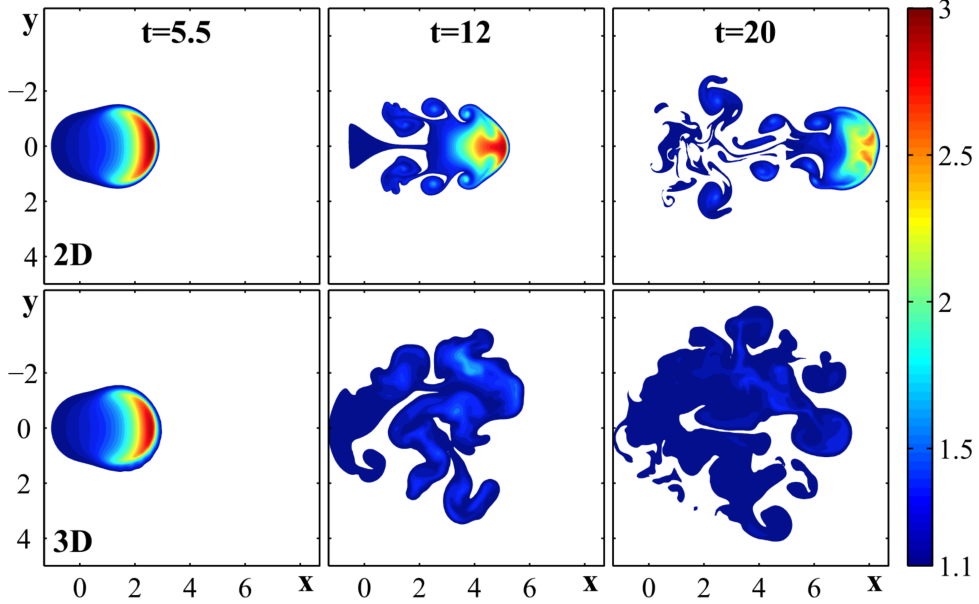


Figure 1.3: Comparison of density contours from 2D (top) and 3D (bottom) simulation [28]. The 3D simulation exhibits significant dissipation of the blob structure due to RDWI.

becomes more significant as the pressure of plasma in the blob increases. In particular, when a plasma beta is larger than the electron and ion mass ratio, the electromagnetic effects become important. In this thesis, a high plasma beta implies that the value of the plasma beta is larger than the electron-ion mass ratio.

In addition, parallel electron dynamics in terms of collisionless wave-particle interaction becomes important specifically in high temperature plasma. For example, a study on drift wave instability that is not limited by the fluid approximation was considered in Ref. [39]. In the kinetic approach, the electrostatic drift-kinetic equation with a Bhatnagar-Gross-Krook(BGK-like) collision operator [40] and the Vlasov equation were used to describe electron and ion dynamics, respectively. It was shown that the wave-particle interaction also exhibits growth rates on the order of the fundamental drift wave frequency.

However, a model that describes plasma regimes considering high beta and weak collisionality together was not studied comprehensively. In addition, the numerical simulation of a collisionless

drift wave inside of the blob filaments is required for the study of nonlinear dynamics of edge plasma turbulence. Therefore, to better understand how electromagnetic effects and parallel wave-particle kinetic interactions will change the characteristics of blob dynamics, an in-depth research on the electromagnetic and parallel electron kinetic effects on the dynamics and stability of blobs is needed for high-beta and weakly collisional plasma in future machines.

The questions investigated in this thesis include: (i) How the electromagnetic effects modify the dynamics and stability of high-beta blobs within fluid approximations. (ii) How electromagnetic effects and kinetic effects change drift waves in both collisional and weakly collisional regimes. (iii) How to numerically simulate collisionless and weakly collisional drift wave instability using a continuum gyrokinetic simulation code to investigate the nonlinear saturation of the wave instability inside blob filaments. An overview of each chapter of this thesis is as follows:

1.5.1 Ch 2: Electromagnetic effects on dynamics of high-beta filamentary structures

Most studies on plasma blobs have been made using only electrostatic approximations that are appropriate for low-beta plasma. However, in future large tokamak devices, such as ITER, the electrostatic model cannot be used because large tokamaks will have large plasma beta values in SOL plasma. The impact of the electromagnetic effect on the propagation and stability of a high-beta plasma filament is examined in this chapter. The terms of magnetic vector potential, electron inertia, and magnetic field line bending are considered in the electromagnetic model. The electromagnetic fluid model is implemented in a BOUT++ code, and the electromagnetic effects on the high-beta filaments are studied from the BOUT++ simulation. Owing to the electromagnetic effects, the plasma filament shows macroscopic effects such as bending due to the delayed parallel propagation speed of the plasma potential perturbation caused by the newly introduced Alfvén wave time scale.

This chapter also discusses how RDWI in plasma is changed by the electromagnetic effect and how it affects the stability of high-beta plasma filaments.

1.5.2 Ch. 3: Electromagnetic drift wave dispersion for arbitrarily collisional plasma

One of the main results in Chapter 2 is that the effect of dissipation of the blob structure is reduced owing to the electromagnetic effect, which reduces the growth rate of collisional RDWI. However, the plasma description model based on the fluid approximation only applies to the limited condition of plasma regimes. In order to describe stability of SOL plasma filaments expected in the future tokamaks, a model satisfying both high-beta and weakly collisional plasma is required. While the effect of reducing the RDWI due to electromagnetic effects appears in the fluid model, the collisionless drift wave instability due to the kinetic effect of wave-particle interactions may still be present.

This chapter discusses how a drift wave in weakly collisional plasma will change due to electromagnetic effects. To accomplish this, the local linear stability analysis in the plasma slab is expanded using an electromagnetic model for arbitrarily collisional electrons and an electromagnetic model of general kinetic ions. The analysis of the electromagnetic drift-kinetic equation for electrons with the Vlasov-Maxwell equation for ions provides a unique opportunity to assess the effects of the electromagnetic and finite ion temperature stabilization of drift waves.

1.5.3 Ch. 4: Verification of 5D continuum gyrokinetic code COGENT: studies of kinetic drift wave instability

The collisional mean free path in the plasma boundary region can sometimes exceed the wave length of microinstability (e.g. drift wave instabilities). In this case, the distribution function of the plasma species deviates from the Maxwellian distribution function during the instability process. To describe the stability of such weakly collisional plasma, an electrostatic gyrokinetic model is considered with an Eulerian finite-volume code, COGENT. The COGENT code was extended to 5D phase space from the previous 4D phase space. The extended code was verified by comparing the simulation result with the analytic result through the linear stability analysis method performed in the previous chapter. The nonlinear saturation of the collisionless drift wave and its transition to the collisional regime, change of the distribution function by the Landau resonance, and helical mode structure of the collisionless drift wave in plasma filaments are discussed in this chapter.

Chapter 2

Electromagnetic effects on dynamics of high-beta filamentary structures

The impacts of the electromagnetic effects on blob dynamics are considered. Electromagnetic BOUT++ simulations on seeded high-beta blobs demonstrate that inhomogeneity of magnetic curvature or plasma pressure along the filament leads to bending of the blob filaments and the magnetic field lines due to increased propagation time of plasma current (Alfvén time). The bending motion can enhance heat exchange between the plasma facing materials and the inner scrape-off layer (SOL) region. The effects of sheath boundary conditions on the part of the blob away from the boundary are also diminished by the increased Alfvén time. Using linear analysis and BOUT++ simulations, it is found that electromagnetic effects in high temperature and high density plasmas reduce the growth rate of resistive drift wave instability when resistivity drops below a certain value. The blobs temperature decreases in the course of its motion through the SOL and so the blob can switch from the electromagnetic to the electrostatic regime where resistive drift waves become important again.

2.1 Introduction

Plasma blobs (filamentary structures extended along the magnetic field lines) are meso-scale turbulent structures usually observed in the scrape-off layer (SOL) of magnetic confinement devices. They are characterized by their convective behavior propagating with velocity V_b reaching several percent of sound speed. Typical blob size is $\sim 1 - 3$ cm and plasma density in the blob is significantly higher than that of the ambient plasma. In tokamaks, blobs appear on the outer side of the torus.

Blobs, which are an inherent part of edge plasma turbulence and transport, controlling plasma-wall interactions, have been extensively studied in last decade. Comprehensive reviews on blobs can be found in Ref. [17] and Ref. [18]. The basic theory of blob physics was introduced in Ref. [16]. The charge separation caused by effective gravity (i.e., curvature and grad(B) effects) results in a radial $E \times B$ convection of plasma. The blob dynamics is sensitive to the interplay between cross field polarization current and the current along the field lines which is the subject of various closures.[17] A recent study of the impact of plasma instabilities on blob dynamics show that the coherency of the blob can be substantially limited by the onset of the resistive drift wave instability resulting in blobs dispersion.[28] However, only electrostatic limit was considered in Ref. [28].

The impact of particles and heat transported by blobs on plasma-facing components becomes more significant as the pressure of plasma in the blobs increases. These large-pressure blobs can be formed by the edge localized mode (ELM) crashes or by turbulent activities in the SOL of large confinement machines. In the case of the increased plasma beta ($\tilde{\beta} \equiv \beta M_i/m_e > 1$, $\beta = 8\pi nT/B^2$) the electromagnetic effects become important. Theoretical work on such electromagnetic blob regimes and their effects on the blob dynamics can be found in Refs. [41, 42, 17, 43]. In addition, the effects of magnetostatic forces on the dynamics of current-carrying filaments have been investigated in Ref. [44]. Recently, the finite ion temperature effects on blob-filament and their implications to

the drift-Alfvén waves have been examined in Ref. [45]. Although some electromagnetic turbulent simulations[46, 47] on tokamak SOL also have been performed, there has been not enough attention to the electromagnetic effects on high- β blob dynamics.

In this paper, we present the result of our studies of the electromagnetic effects on the seeded high- β blob dynamics and stability with BOUT++ framework.[48] The three-dimensional electromagnetic simulations on the high- β blob will be compared with the results from the electrostatic calculation. In addition, we supplement our numerical simulations with analytic estimates of blob stability in the electromagnetic regime.

The paper is organized as follows: In Section 2.2, the equations used to describe blob dynamics are presented; The impact of electromagnetic effects on macroscopic blob dynamics are considered in Section 2.3; The electromagnetic effects on blob dynamics due to the resistive drift wave instability are discussed in Section 2.4; A discussion of the results and conclusions are presented in Sections 2.5 and 2.6, respectively.

2.2 Governing equations, initial and boundary conditions

2.2.1 Governing equations

We present our simple model for the electromagnetic effects on blob propagation. The blob's plasma dynamics are considered using fluid approximation and a three-dimensional Cartesian geometry with z -coordinate aligned to magnetic field, \mathbf{B} , and x -, y -coordinate correspond to the radial and effective poloidal direction, respectively. Under fluid approximation, the fundamental equations for describing the blob dynamics are: the density conservation of plasma species, current conservation, the equation of motions and Maxwell equations for electromagnetic fields. These equations can be simplified to coupled equations of vorticity, density, and parallel component

of vector potential with approximations of isothermal electron temperature and quasi-neutrality of plasma.[28] A derivative-like term in the vorticity equation can be further simplified to $\nabla \cdot d/dt(n\nabla_{\perp}\phi) \approx nd/dt(\nabla_{\perp}^2\phi)$ by Boussinesq approximation. The Boussinesq approximation gives reasonably accurate results for blobs with moderate blob to ambient plasma density ratio.[49]

Finite ion temperature effects can enhance polarization drift modifying the blob propagation speed.[45] For the case of large blob to ambient plasma density ratio, \tilde{n}/n_0 , the finite ion temperature may dominate standard vorticity term, $\nabla \cdot [en\nabla_{\perp}\phi + \nabla_{\perp}(nT_i)]$, breaking the dipole vorticity structure in blobs.[50] However, the Alfvén wave physics, which is important for electromagnetic high- β blob dynamics, will not be affected by the ion temperature. Therefore, we simplify our model using cold ion temperature approximation.

Parallel ion dynamics in the form of sound waves can be important when the variation of plasma density along the magnetic field line is significantly large. However, we consider a case where the propagation time of ions in parallel direction is much larger than the radial advection time. Therefore, the parallel ion dynamics can be ignored.[28]

Using approximations described above, we have the following set of simplified equations[28, 48]

$$\frac{e\rho_s^2}{T_e}n \frac{d}{dt}(\nabla_{\perp}^2\phi) = \frac{1}{e}\nabla_{\parallel}J_{\parallel} - \frac{g}{\Omega_i} \frac{\partial n}{\partial y}, \quad (2.1)$$

$$\frac{dn}{dt} = \frac{1}{e}\nabla_{\parallel}J_{\parallel} - \frac{g}{\Omega_i} \frac{\partial n}{\partial y}, \quad (2.2)$$

$$\frac{dA_{j\parallel}}{dt} = \frac{e}{m_e} \frac{\partial \phi}{\partial z} - \frac{T_e}{m_e} \nabla_{\parallel} \ln n + \frac{e}{\sigma_{\parallel} m_e} J_{\parallel}, \quad (2.3)$$

where n is the plasma density, ϕ is the electrostatic potential, and T_e , m_e and $-e$, are the electron temperature, mass and charge, respectively. We introduce gyro-Bohm radius, $\rho_s = c_s/\Omega_i$, where $c_s = (T_e/M_i)^{1/2}$ is the ion sound speed, Ω_i is the ion gyro-frequency and M_i is the ion mass.

$g = 2c_s^2/R$ is the effective gravitational acceleration representing polarization drive due to the magnetic curvature and $\text{grad}(B)$ effects, and R is the tokamak major radius. $\sigma_{\parallel} = 1.96 n_e e^2 \tau_e / m_e$ is the plasma electric conductivity along the magnetic field, where $\tau_e = 3.44 \times 10^5 T_e^{3/2} / (n_e \ln \Lambda)$ is the electron collision time with a coulomb logarithm $\ln \Lambda \simeq 10$. The derivative operators are defined as $d/(dt) = \partial/(\partial t) + (c/B)\hat{b}_0 \times \nabla \phi \cdot \nabla$ and $\nabla_{\parallel} = \partial/(\partial z) + (\nabla A_{\parallel}/B_0) \times \hat{b}_0 \cdot \nabla$, and where \hat{b}_0 is the unit vector along the unperturbed magnetic field. $A_{j\parallel}$ is defined as summation of the parallel component of vector potential and an electron inertia term,[51]

$$A_{j\parallel} \equiv -\frac{eA_{\parallel}}{m_e c} - \frac{J_{\parallel}}{ne}, \quad (2.4)$$

where c is the speed of light. The parallel vector potential A_{\parallel} is calculated by the inversion of following relation,

$$J_{\parallel} = -\frac{c}{4\pi} \nabla_{\perp}^2 A_{\parallel}. \quad (2.5)$$

Note that we also have neglected diffusivity and viscosity terms in Eqs. (2.1) and (2.2). Reynolds numbers for the diffusivity and viscosity terms are estimated as $R_D \sim (V_b/c_s)(M_i/m_e)$ $(\lambda_c \delta / \rho_s^2) \gg 1$ and $R_{\mu} \sim (V_b/c_s)(\lambda_c \delta / \rho_i^2) \gg 1$, respectively. V_b and δ are characteristic blob speed and size, λ_c is collisional mean free path for ion. Within the large Reynolds number orderings, the diffusivity and viscosity terms become small. In this case, the radial motion of blob is dominated by the interchange drive, and dissipative effects due to diffusion and viscous collisions are ignored.

Comparing the parallel vector potential equation (or generalized Ohm's law), Eq. (2.3), with the electrostatic collisional Ohm's law,

$$J_{\parallel} = \sigma_{\parallel} \left(\frac{T_e}{e} \nabla_{\parallel} \ln n - \nabla_{\parallel} \phi \right), \quad (2.6)$$

we notice that the main differences between the electromagnetic model and the electrostatic model[28] are the time derivatives of the parallel vector potential and the electron inertia ($dA_{j\parallel}/dt$) and the field line bending ($\nabla \times A_{\parallel}/B_0$) terms. The validity of the electrostatic approximation is supported by $\tilde{\beta} < 1$, which provides $v_A^2 \equiv B^2/(4\pi n M_i) > v_{Te}^2$ condition.

Equations (2.1-2.5) provide three coupled equations for ϕ , n and $A_{j\parallel}$ governing the electromagnetic blob dynamics. For the electrostatic calculations, Eqs. (2.1,2.2,2.6) with $\nabla_{\parallel} \approx \partial/(\partial z)$ are used to solve for ϕ , n and J_{\parallel} .[28]

2.2.2 Initial and boundary conditions

Solving the given system of Eqs. (2.1-2.5), requires boundary and initial conditions of all variables. Following Refs. [28, 52] we consider initial plasma density as a homogeneous background and with a bump on it, $n = n_0 + \tilde{n}(\mathbf{x})$, with $\tilde{n}(\mathbf{x}) = \tilde{n}_b \exp[-((x-x_0)^2 + (y-y_0)^2)/\delta^2]$, where (x_0, y_0) is the initial location of blob's center of mass in transverse plane and δ is a characteristic blob radius. All other variables are set to zero at the beginning of the simulations.

The conditions of electric potential, density and current density at the domain boundary along the magnetic field lines play important roles in blob dynamics. We apply Neumann conditions at the upper (+) and the lower (−) boundaries in z -directions for density, $\partial n/(\partial z)|_{\pm} = 0$. The lower and upper boundaries correspond to the points $z = 0$ and $z = L$, respectively. The sheath limited boundary condition for electric potential is one possible choice because parallel magnetic fields end at a material surface in an open magnetic configuration such as the SOL. The condition that the current in the z -direction is sheath limited at the parallel boundaries is

$$J_{sh\pm} = \pm \frac{c_s e^2}{T_e} n_{\pm} \phi_{\pm}, \quad (2.7)$$

where n_{\pm} and ϕ_{\pm} are the density and the electric potential at the upper and the lower sheath boundaries, respectively. ϕ_{\pm} is taken with respect to the floating potential $\phi_f \approx 3T_e/e$.[28] Assuming field line bending is small at the boundary region, the current density from the generalized Ohm's law, Eq. (2.3), near the boundary region is represented as

$$J_{\parallel\pm} = \sigma_{\parallel} \frac{\partial \phi}{\partial z} \Big|_{\pm} - \frac{\sigma_{\parallel}}{c} \frac{\partial A_{\parallel}}{\partial t} \Big|_{\pm}. \quad (2.8)$$

The sheath limited boundary condition for ϕ is found by equating the limiting conditions of parallel currents at the material surfaces, Eq. (2.8), with the plasma conditions for parallel currents at the parallel boundaries, Eq. (2.7). We use constant gradient conditions at the sheath boundaries for parallel current, i.e. $\partial J_{\parallel}/(\partial z)|_{sh\pm} = \partial J_{\parallel}/(\partial z)|_{\pm}$ assuming continuous polarization.

It is worthwhile noting here that the boundary conditions of high- β filaments may not have the sheath limited condition. In other words, the physical locations of the longitudinal terminal points of the filaments can be actually inside the separatrix not on the material surfaces.[18] In this case determining exact boundary conditions along the field line is difficult because the conditions are to be coupled to the plasma parameters near the interface between the core and edge region.

Therefore, in addition to the sheath limited boundary condition that describes the parallel interface between a filament and material surface, we can also consider a simple boundary condition that disconnects the filament from the surface. This free boundary condition is given as Neumann condition on electric potential and density, $\partial\phi/(\partial z)|_{\pm} = \partial n/(\partial z)|_{\pm} = 0$, and a Dirichlet boundary condition on the parallel current density, $J_{\parallel}|_{\pm} = 0$. The situation where $J_{\parallel}|_{\pm}$ is zero corresponds roughly to the case where the filament is located near the X-point of magnetic topology in magnetic confinement devices. Increasing effective resistivity in the X-point region hinders parallel currents and the filament regime is electrically disconnected from the sheath boundary and approaches the resistive ballooning regime.[18, 42]

2.3 Electromagnetic effects on blob propagation

2.3.1 Electromagnetic effects and sheath boundary condition

As stated in Section 2.1, blob dynamics are determined by the dipole potential that results from the balance between the perpendicular polarization current and the parallel current. Therefore, boundary conditions for the parallel current become an important factor in blob dynamics. In electrostatic approximations, boundary conditions (e.g. sheath limited conditions) have immediate effects on blob dynamics throughout the entire filamentary length, whereas in electromagnetic calculations the boundary effects are reduced due to the slower Alfvén speed at high- β plasmas.

For the purpose of comparing boundary effects on electromagnetic and electrostatic high- β blobs, we perform 3D simulation using BOUT++ code[48]. Considering an ITER relevant edge plasma, the radius of curvature and the connection length are set to $R \sim 6$ m and $L \sim 100$ m respectively. As an initial condition we seed a blob with a Gaussian function, $n/n_0 = 1 + (\tilde{n}_b/n_0) \exp[-(x^2 + y^2)/\delta^2]$, where the relative blob amplitude is set as $\tilde{n}_b/n_0 = 2$. The plasma is considered to have high- β as $\tilde{\beta} \sim 3$ for $T_e = 200$ eV, $n_0 = 1 \times 10^{14}$ cm⁻³ and $B = 5.3$ T. Note that these plasma parameters are somewhat higher than those predicted by two-dimensional modeling on core-edge plasma for the ITER machine.[53] The parameters for the high- β filament correspond to a plasma with a collisional regime satisfying $\lambda_e/L \sim 0.02 \ll 1$. The cross sectional blob size is set to the characteristic size $\delta = \delta_* \equiv \rho_s (gL^2/(4c_s^2 \rho_s))^{1/5}$ as in Refs. [28, 17].

The results from electromagnetic and electrostatic calculations for the sheath boundary condition using the high- β parameters with blob size $\delta/\delta_* = 1$ are shown in Fig. 2.1. The 2D density contours are obtained by taking average along the field line. Notice that the averaged density contours from the electromagnetic simulation (top) develop “mushroom” shape and propagate in radial direction with faster speed while electrostatic simulation (bottom) shows virtually no

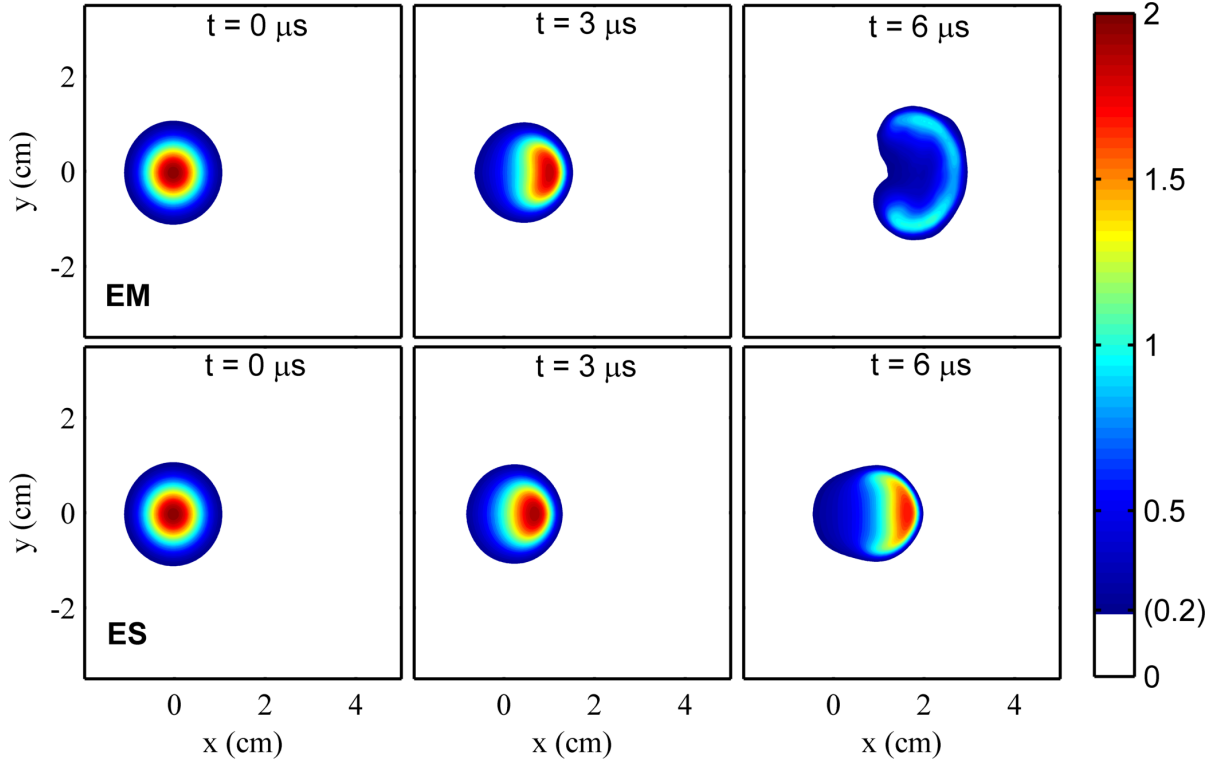


Figure 2.1: Comparison of the sheath limited high- β blob evolution from electromagnetic (top) and electrostatic calculation (bottom) for balanced size blob ($\delta/\delta_* = 1$). The 2D contours are the averaged value of \tilde{n}/n_0 along the field line. The electromagnetic simulation (top) gives higher blob speed, which finally causes the “mushrooming”. However, the electrostatic simulation (bottom) shows the “balanced” motion of blob.

“mushrooming”.

The reason for this discrepancy is that the parallel current development mechanism is different in the two calculations. Due to immediate formation of the Ohmic current along the magnetic field lines, the electrostatic calculation causes polarized charges to quickly flow to sheath boundary. However in electromagnetic case, parallel current propagates toward the sheath with Alfvén speed. As a result, for the case where Alfvén time, $\tau_A = L/v_A$, is larger than characteristic blob propagation time, $\tau_b = \delta/V_b$, electromagnetic simulations give higher polarization potential (see Fig. 2.2) and, consequently, higher speed, which finally causes “mushrooming” (see Fig. 2.1). Estimating τ_b for structurally stable blob size,[17] $\delta = \delta_*$, we find $\tau_A/\tau_b = \beta^{1/2}(L^4/\rho_s^2/R^2)^{1/5}$. For the parameters

we used for our simulations $\tau_A/\tau_b \sim 4$. We also note that the slow development of parallel current dipole structure may lead to the bending of filament. Further explanation on this electromagnetic bowing of filamentary structure will be given in following subsection.

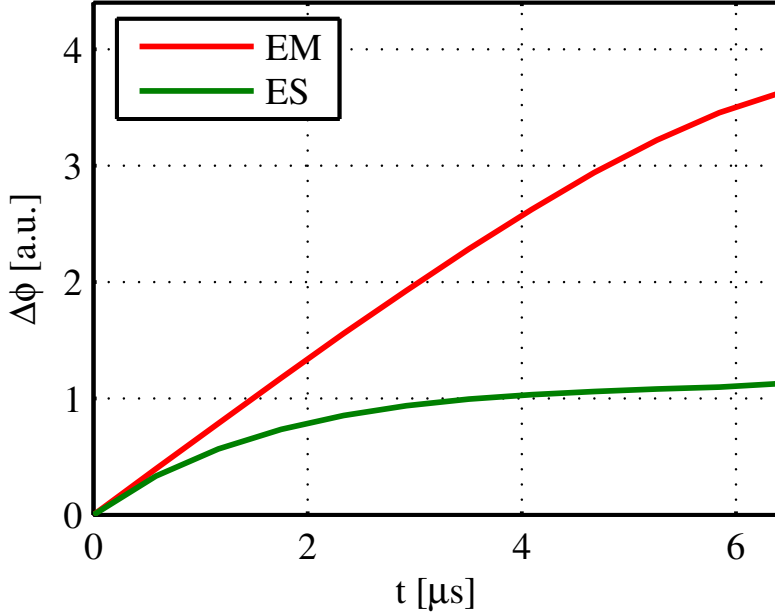


Figure 2.2: Comparison of the dipole potential strength in the sheath limited high- β blobs for electromagnetic (red) and electrostatic calculation (green). Electromagnetic simulation shows higher dipole potential strength because the charge loss to the sheath boundary is decreased due to the increased parallel current development (or Alfvén) time.

2.3.2 Electromagnetic effects and inhomogeneous polarization

In previous sub-Section we consider the case of homogeneous initial blob density along the magnetic field lines and constant g . However, in practice both blob plasma density and g can vary along the magnetic field lines (e.g. recall that g has different sign on outer and inner torus sides in a tokamak). This will cause non-homogeneous polarization of blob resulting in variation of velocities of different parts of blob and blobs shape bending along the magnetic field lines. We also notice that non-uniform blob plasma density distribution along the field line can cause blob spinning.[28]

We performed three dimensional numerical simulations of high- β seeded blobs in a varying curvature for the electromagnetic and the electrostatic calculations. For the demonstration of filament bending, we consider a simple curvature variation in a form $\kappa_x \sim -\sin^2(\pi z/L)/R$ in the Cartesian computational frame. Under this condition, the value of the curvature has zero (neutral) at the end points and the maximum (unfavorable) at the mid-point of the filament. The free boundary conditions were used in the z -direction. The Neumann and the periodic boundary conditions were applied for x and y -direction respectively. A cylindrical blob with cross sectional size $\delta \sim 0.5$ cm is seeded at $t = 0$. And other blob parameters are the same as those of the sheath limited blob simulation.

The sequence of normalized blob density from the electromagnetic and the electrostatic simulation is shown in Fig. 2.3. The comparison between electromagnetic and electrostatic simulations demonstrates how the filamentary structure is bent by electromagnetic effects. The electromagnetic simulation shows a non-uniform motion along the filament: a strong radial movement in the most unfavorable curvature location and a rather delayed radial motion near the neutral curvature region. Meanwhile for electrostatics, the radial motion shows uniform distribution along the filament despite the inhomogeneous curvature field.

The reason for such discrepancy between the electromagnetic and electrostatic simulation is the large ratio $\tau_A/\tau_b \sim 4$, which slows down the parallel current propagation which could equilibrate potential along the magnetic field lines. In Fig. 2.4, one can see the evolution of maximum potential difference distribution along the field line from the two simulations. The non-uniform potential distribution in the electromagnetic filament slowly becomes uniform, while in the electrostatic calculation it is macroscopically uniform from the beginning. It is also interesting to see that the electromagnetic simulation did not produce instability at the time when the electrostatic approximation showed the resistive drift wave instability sometime around $t \sim 5 \mu\text{s}$. More details on this microscopic effects will be discussed in Sec. 2.4.

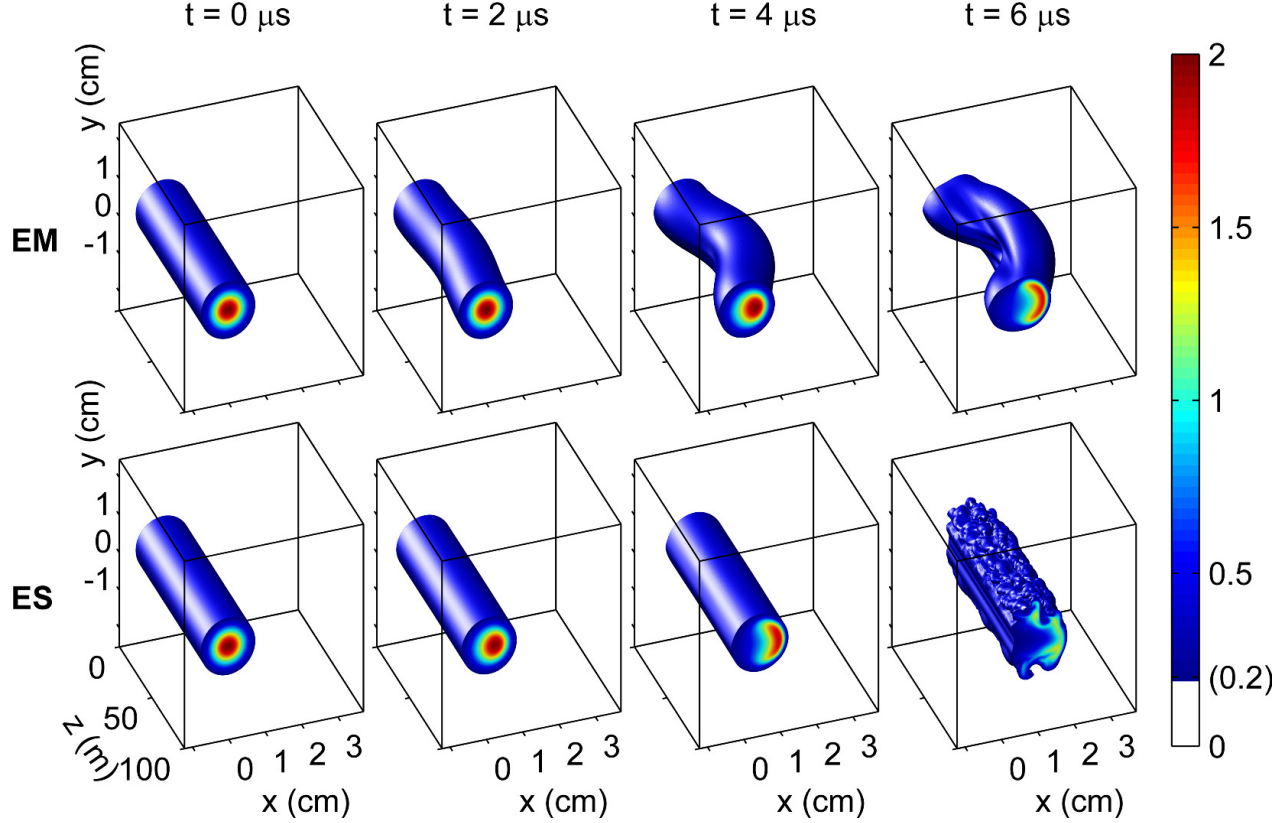


Figure 2.3: Evolution of density (\tilde{n}/n_0) for the high- β filament in the varying curvature along the field line from electromagnetic (top) and electrostatic (bottom) calculations. The z -axis is not to scale.

The maximum difference of convection speed can be estimated by normalization of the vorticity equation with Alfvén time. From the vorticity equation, Eq. (2.1), the maximum difference of $E \times B$ velocity between center and boundary region of Alfvén wave emitting blob is estimated as

$$\Delta v_x(t) \simeq \beta^{1/2} \frac{L}{R} c_s G(\kappa, n) \frac{t}{\tau_A} + F(J_{\parallel}(t)), \quad (2.9)$$

where $G(\kappa, n) = 1 - \kappa_{z=L} n_{z=L} / (\kappa_{z=L/2} n_{z=L/2})$ is a geometrical weighting factor with order of ~ 1 considering the ratio of the most unfavorable ($z = L/2$) and most favorable ($z = L$) curvature and the ratio of inhomogeneous filament density along the field line. F is a function of parallel current that makes the velocity difference become small after $t \sim \tau_A$. Integrating the velocity difference, we get

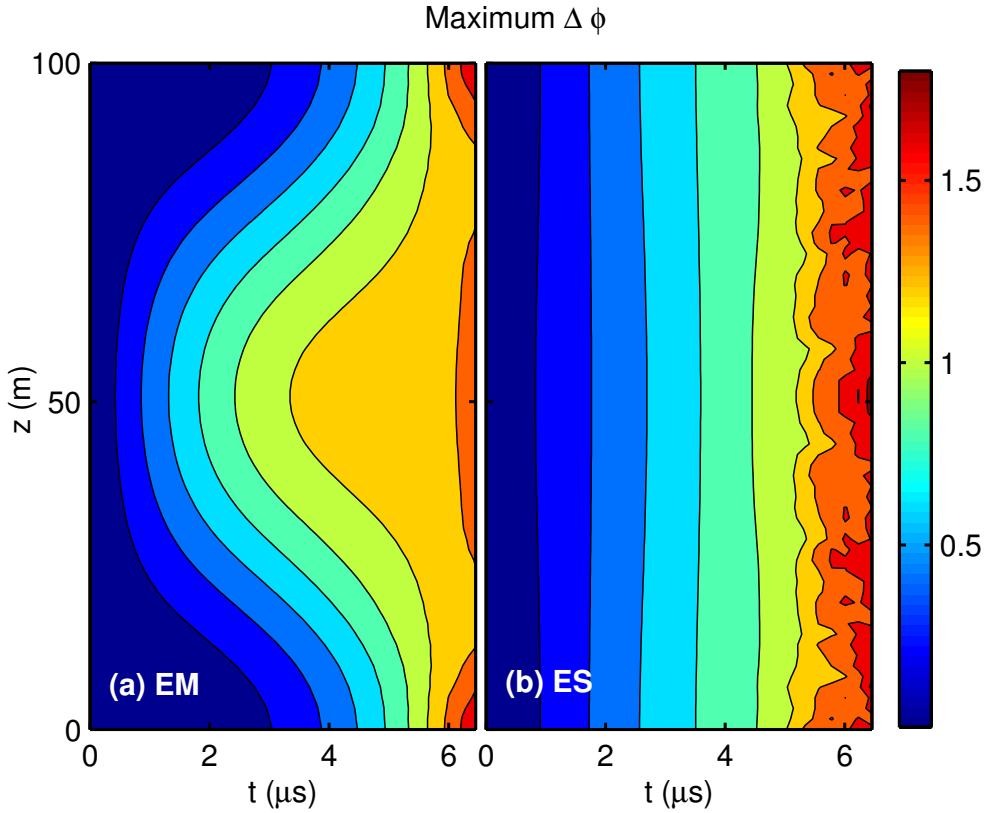


Figure 2.4: Comparison of the dipole potential evolution for (a) electromagnetic and (b) electrostatic calculation on high- β filament submerged in the inhomogeneous curvature field. The maximum value of potential difference (in arbitrary unit) is calculated over the drift (x, y) plane in location z at time t .

an expression for the filament bending

$$\Delta x_{\text{bending}} \lesssim \int_0^{\tau_A} \Delta v_x(t) dt \sim \frac{1}{16} \beta \frac{L^2}{R} G(\kappa, n). \quad (2.10)$$

Similar scaling of line bending for high plasma pressure filament was also obtained in Ref. [41].

The Alfvén wave emitting electromagnetic filament will also involve the bending of magnetic field as well as the bending of plasma filament. The inhomogeneous three dimensional polarization causes the development of current dipole for both the electromagnetic and electrostatic simulations. Fig. 2.5 shows the time slices of parallel current dipole in isosurface plots for an electromagnetic

simulation (top row) and for an electrostatic simulation (bottom row). The parallel current densities are normalized by $J_0 = en_0(T_e/M_i)^{1/2}$ and multiplied by scale factors for better visualization. Note that this kind of current dipole is also formed in the filaments with sheath boundary condition. Experimental measurements and 2D numerical simulation of asymmetric dipolar structures of the parallel currents are found in Ref. [54].

The magnetic field line bending caused by the parallel current dipole is estimated as

$$\Delta x_{\text{mag}} \sim \int_0^{L/2} \left| \frac{B_x}{B} \right| dz \lesssim \frac{1}{16} \beta \frac{L^2}{R} G(\kappa, n). \quad (2.11)$$

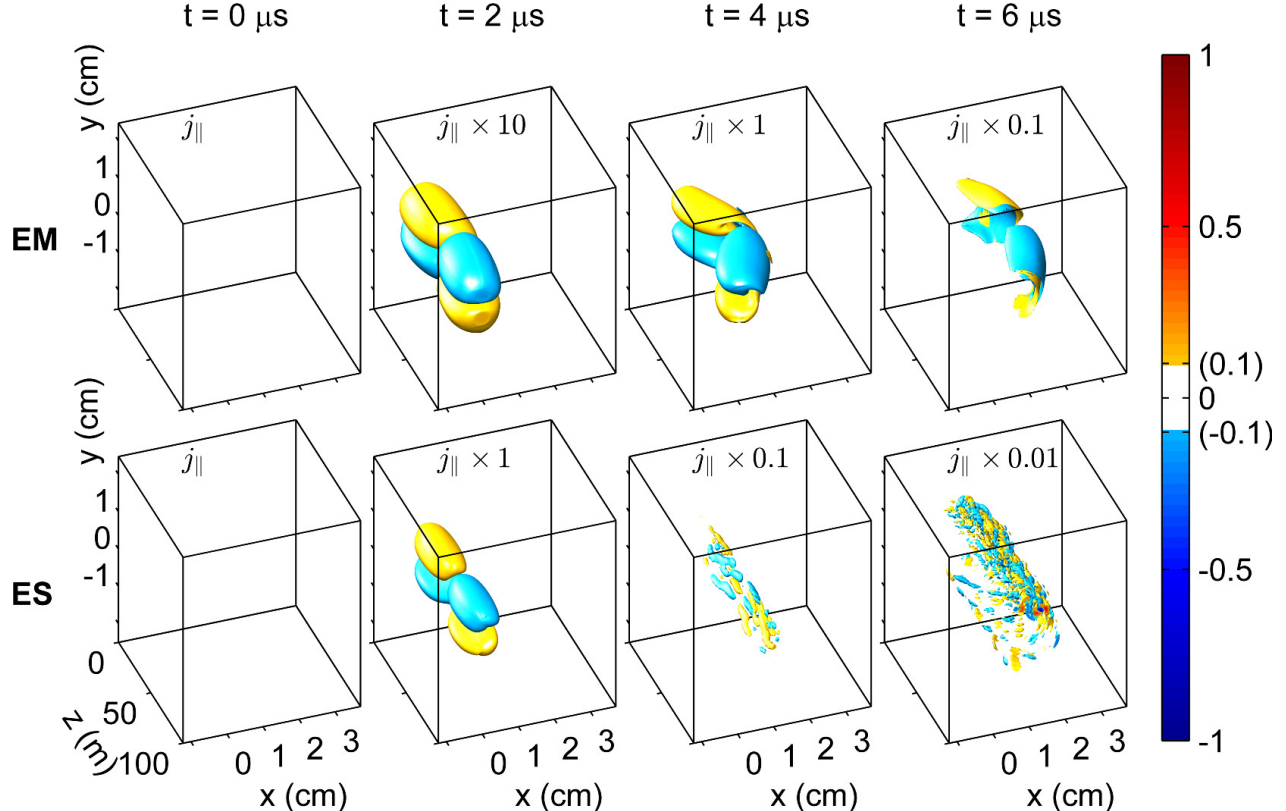


Figure 2.5: Evolution of parallel current ($j_{\parallel} \equiv J_{\parallel}/J_0$) for the high- β filament in the varying curvature along the field line from electromagnetic (top) and electrostatic (bottom) calculations. The parallel currents have been devided by a normalizing factor, $J_0 = en_0(T_e/M_i)^{1/2}$. The parallel current dipoles increase faster in the ES case than those of the EM case. The z -axis is not to scale.

The field line bending given in Eq. (2.11) follows the same form as the plasma bending given in Eq. (2.10). This suggests that the magnetic field lines will be “frozen-in” to the high- β filament. Fig. 2.6 shows the magnetic field lines with density contour slices in time. In the electromagnetic calculation (top row of Fig. 2.6), the magnetic field line (red curve online) threading the center of blob shows synchronized motion with peak density at $t = 2 \mu\text{s}$. In the electrostatic simulation, however, the virtual magnetic field lines (magnetostatic perturbations) are recomposed from the Ohmic current (Eq. 2.6) and they do not show the “frozen-in” motion.

The electrostatic (ES) calculation is essentially an approximation of the electromagnetic (EM) calculation. This results in stronger ES perturbations than the EM perturbations. However, such approximation is not physically valid in the case of high-beta filaments because the magnetic field perturbations cannot grow freely when they are coupled with (or frozen-into) plasma elements. The parallel current calculation (Eq. 2.6) in the electrostatic case does not account for the electromagnetic induction of the parallel component of vector potential ($\partial_t A_{\parallel}$). As a result, the parallel currents in the ES case develop faster than those in the EM case. (See Fig. 2.5).

The plasma pressure for given temperature and density ($T_e = 200 \text{ eV}$, $n_0 = 1 \times 10^{14} \text{ cm}^{-3}$) is high enough to make the magnetic field line bending. The z-axis is much longer than the perpendicular axes by about 10^4 times. Therefore, the ratio of the perturbed magnetic field (B_r) to the unperturbed magnetic field (B_0) is about 10^{-4} (Fig. 2.6). The ratio of the plasma pressure to the perturbed magnetic pressure is roughly $(B_0/B_r)^2 8\pi p/B_0^2 \sim 10^5$ for $\beta \sim 10^{-3}$. In addition, the ratio of the magnetic diffusion rate, $\omega_{\eta} = c^2/(4\pi\delta^2\sigma_{\parallel})$, to the rate of the blob convection, $\omega_b \sim V_b/\delta$, is found to be $\omega_{\eta}/\omega_b \sim 10^{-3}$ for given plasma temperature $T_e = 200 \text{ eV}$ and $\delta \sim 10^{-2} \text{ m}$. Therefore, within an isothermal approximation, the magnetic field line diffusion is negligible in the scale of blob size.

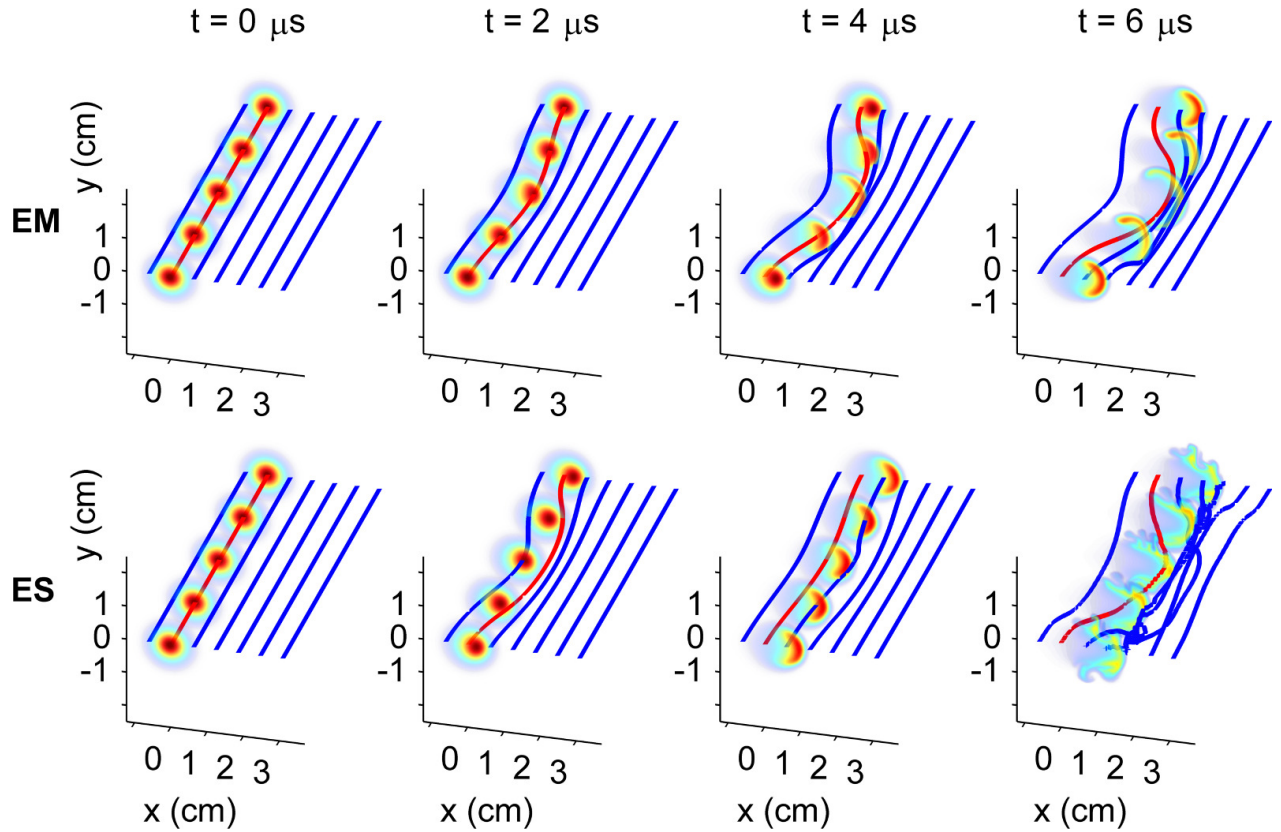


Figure 2.6: Magnetic field line bending for the high- β filament in the varying curvature along the field line from electromagnetic calculation (top). For the electrostatic calculation (bottom), the virtual magnetic field perturbations are calculated by inversion of electrostatic current. Blue and red lines are the total magnetic field lines initially aligned along the z -axis (not to scale). The red curve represents the magnetic field line with initial location of filament.

2.4 Electromagnetic effects on blob stability

So far we discussed on the macroscopic effects on blob dynamics. However, as we have seen in Figs. 2.3-2.6, there are also different behaviors in the microscopic activities between electrostatic and electromagnetic calculations. The resistive drift wave instability (RDWI) from the electrostatic approximation is modified by the electromagnetic and electron inertia perturbations. When the resistive effect becomes small due to increased electron temperature, the electrostatic approximation is not enough to describe the system and the wave instability should be described by electromagnetic

terms. In the high temperature plasmas, the wave instability can be either modified by electromagnetic drift-Alfvén wave with reduced growth rate or enhanced by the electron inertia instability.

To evaluate the onset of plasma turbulence of filamentary structures, we perform a local linear stability analysis. We consider exponentially decaying density $\partial \ln n / (\partial x) = -1/\delta$. This decaying density profile can represent the seeded blob with Gaussian density profile at the local point half radius away ($|x - x_0| \sim \delta/2$) from the center of blob. The normal mode perturbation of density, electric potential and parallel vector potential are assumed to have the form $\exp(i\mathbf{k} \cdot \mathbf{r} - i\omega t)$, where \mathbf{k} is wave number vector. Carrying out an analysis similar to that of Ref. [28], we get the following dispersion equation

$$\omega^2 + \omega_g^2 - \omega \frac{g\chi}{c_s} = -i\omega_{\parallel}^{\text{EM}} \left(\omega - \frac{\omega_*}{1 + \chi^2} \right), \quad (2.12)$$

where

$$\omega_{\parallel}^{\text{EM}} = i\omega_A^2 \frac{(1 + \chi^2)}{\left(\omega - \omega_* + \omega \frac{k_{\perp}^2 c^2}{\omega_{\text{pe}}^2} + i \frac{k_{\perp}^2 c^2}{4\pi\sigma_{\parallel}} \right)}, \quad (2.13)$$

and $\omega_g = \sqrt{g/\delta}$ is flute mode growth rate, $\omega_* = k_y c_s \rho_s / \delta$ is a drift frequency, $\omega_A = k_z v_A$ is the Alfvén frequency and $\chi = k_y \rho_s$ is a normalized perpendicular wave number with $k_x \rho_s \ll 1$ approximation.

When $\omega_g^2 \gg \omega_A^2$ is satisfied, the wave instability is dominated by flute mode, $\omega \sim i\omega_g$. This radial motion driven by the gravitational (curvature) force will significantly modify the initial approximation of the local density profile, $n \sim \exp(-x/\delta)$. Therefore, we simplify the dispersion relation neglecting gravity (curvature) effects by considering high parallel wave number case $k_z \gg \omega_g/v_A$.

Within a drift frequency ordering, it is useful to normalize the previous dispersion relation with a frequency scale free from wave number. If we consider a normalizing parameter $\hat{\omega}_* \equiv c_s/\delta =$

ω_*/χ , we get the representation of perpendicular and parallel wave number by χ and ω_A respectively.

Then, the normalized dispersion relation is

$$\Omega^2 \left[\Omega - \chi + \frac{\Omega \chi^2}{\tilde{\beta}} + i \Omega_R \chi^2 \right] = \Omega_A^2 [\Omega(1 + \chi^2) - \chi], \quad (2.14)$$

where $\Omega \equiv \omega/\hat{\omega}_*$ is a normalized wave frequency, $\Omega_R = c^2/(4\pi\sigma_{\parallel}\rho_s^2\hat{\omega}_*)$ is a normalized collision frequency and $\Omega_A = \omega_A/\hat{\omega}_*$ is a normalized Alfvén frequency.

In the LHS bracket of Eq. (2.14), the first two terms correspond to the electromagnetic responses; the first term originated from the time derivative of parallel vector potential, $\partial A_{\parallel}/\partial t$ and the second term correlate with the field line bending term, $\nabla A_{\parallel}/B_0 \times \hat{b}_0 \cdot \nabla \ln n$. On the other hand the third and fourth term correspond to two kinds of dissipation terms; the electron inertia term, $\tilde{\beta}^{-1}\chi^2\Omega$, describes the “unfrozenness” of magnetic field on a scale length of the order of collisionless skin depth and the fourth term, $i\Omega_R\chi^2$, explains the plasma resistivity.

Initially we begin the stability analysis of Eq. (2.14) by considering electrostatic limit as a reference. If the resistivity term, $i\Omega_R\chi^2$, dominates other electromagnetic and electron inertial terms in the drift wave frequency range, such that $\Omega_R \sim B^2\delta/T_e^3 \gg 1 + \tilde{\beta}^{-1}$ is satisfied, then we get the following electrostatic dispersion relation similar to the equation found in Ref. [28],

$$\Omega^2 \Omega_R \chi^2 + i \Omega_A^2 [\Omega(1 + \chi^2) - \chi] = 0. \quad (2.15)$$

In this case, this wave dispersion relation describes drift wave as $\Omega^2(\Omega_A^2 \rightarrow \infty) = (\chi/(1 + \chi^2))^2$. The growth rate of the resistive drift wave is found to be

$$\frac{\gamma}{\hat{\omega}_*} = \left\{ \sqrt{\frac{\xi^4}{4} + \left(\frac{\chi}{1 + \chi^2} \right)^2 \xi^2} + \frac{\xi^2}{2} \right\}^{1/2} - \xi, \quad (2.16)$$

where $\xi = (1 + \chi^2)\Omega_A^2/(2\chi^2\Omega_R)$. The growth rate shows asymptotic behaviours such $\gamma/\hat{\omega}_*(\xi \rightarrow 0) = \sqrt{\xi/2}$ and $\gamma/\hat{\omega}_*(\xi \rightarrow \infty) = 1/(8\xi)$. The maximum growth rate of the electrostatic resistive drift wave instability is found to be $\gamma_{\max}/\hat{\omega}_* \sim 0.15$ without a dependency on Ω_R for $\xi \simeq 0.24$ with $\chi = 1$.

We next consider following an ideal electromagnetic dispersion equation by neglecting dissipation terms ($\Omega\chi^2\tilde{\beta}^{-1} + i\Omega_R\chi^2$) from Eq. (2.14). This condition can be achieved from high beta ($\tilde{\beta}^{-1} \rightarrow 0$) and high temperature ($\Omega_R \rightarrow 0$) plasma. For $\chi \sim 1$, $\Omega_A^2 \gg 1$ limit, we get a drift wave with frequency, $\Omega = \chi/(1 + \chi^2) \leq 1 \ll \Omega_A$, and outward emitting kinetic Alfvén waves, $\Omega^2 = \Omega_A^2(1 + \chi^2)$. For $\Omega_A^2 \ll 1$, we get a drift wave ($\Omega = \chi$) and two Alfvén waves ($\Omega^2 = \Omega_A^2$). The dispersion equation has three distinctive real roots for $\chi > 1$, $\Omega_A > 0$. Therefore, all three waves are stable in the ideal electromagnetic case. However, a small resistive correction ($\Omega_R < 1$) can make the drift wave unstable. Neglecting the electron inertia term, we find that: for $\Omega_A^2 \gg 1$, the growth rate of the resistive drift wave is estimated as $\gamma/\hat{\omega}_*(\chi \sim 1) \sim \Omega_R\chi^4/(\Omega_A^2(1 + \chi^2)^3)$ and $\gamma/\hat{\omega}_*(\chi \gg 1) \sim \Omega_R/(\Omega_A\chi)^2$; for $\Omega_A^2 \ll 1$, the growth rate is approximately $\gamma/\hat{\omega}_*(\chi \gg 1) \sim (\Omega_A^2\chi\Omega_R/(1 + \Omega_R^2\chi^2))^{1/2}$. Thus, in contrast to the electrostatic case where $\gamma_{\max}/\hat{\omega}_* \sim O(1)$ and is independent of Ω_R , the electromagnetic case exhibits a strong reduction in the growth rate: $\gamma_{\max}/\hat{\omega}_* \leq \Omega_R \ll 1$.

Figure 2.7 shows contour lines of the normalized growth rate of drift wave instability from numerical calculation of the electromagnetic equation Eq. (2.14) and the electrostatic dispersion equation Eq. (2.15) for plasma parameters with $T_e = 200$ eV and $n_0 = 1 \times 10^{14}$ cm $^{-3}$. The maximum normalized growth rate of this drift-Alfvén wave is about 3.73 times smaller than that of the electrostatic resistive drift wave instability with maximum value 0.15. The value of the contour lines from the electromagnetic calculations are multiplied by a factor 3.73 for better visibility. This reduction of instability is also observed in fluid simulations using BOUT++ (See Fig. 2.8).

The interaction between the magnetic field lines and the high- β plasma plays a role in the

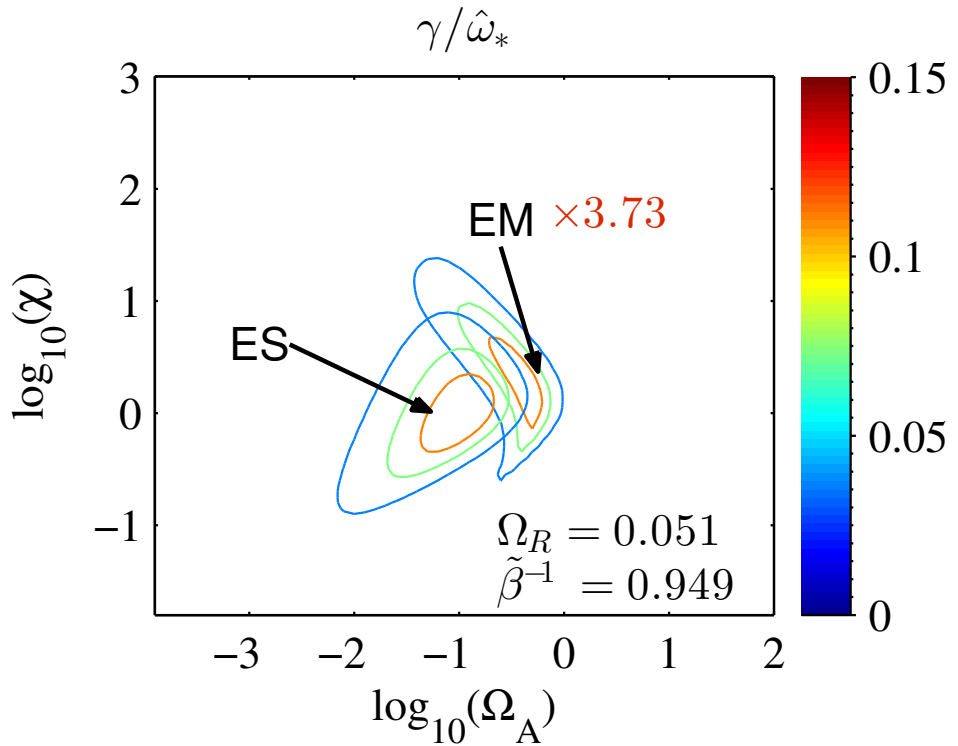


Figure 2.7: Normalized growth rate $\gamma/\hat{\omega}_*$ as function of Ω_A and χ for two different models: electromagnetic (EM) and electrostatic (ES) calculation. Note that the EM growth rate represents drift-Alfvén wave and is multiplied by 3.73 for clarity. The parameters Ω_R and $\tilde{\beta}^{-1}$ correspond to a high beta plasma with $T_e = 200$ eV, $n_0 = 1 \times 10^{14}$ cm $^{-3}$.

suppression of drift wave turbulence. When the density of filaments have sufficiently high value of β , the filament carries “frozen-in” magnetic field lines. When the resistive drift waves grow, the perturbed parallel currents due to the drift waves will induce perpendicular magnetic fields resulting in net helical field lines in low- β plasma. Unlike the electrostatic case, however, the perturbed magnetic field should move with plasma elements in electromagnetic high- β case. Because the free energy of instability should modify the whole system including magnetic fields and plasmas, the electromagnetic effects makes the instability grow much slower than the electrostatic case. Moreover, distorting motions of plasma element will cause local bending magnetic field and this bent magnetic field exert restoring force on the plasma perturbation.

Comparing the contour lines in Fig. 2.7 obtained with the electromagnetic and electrostatic

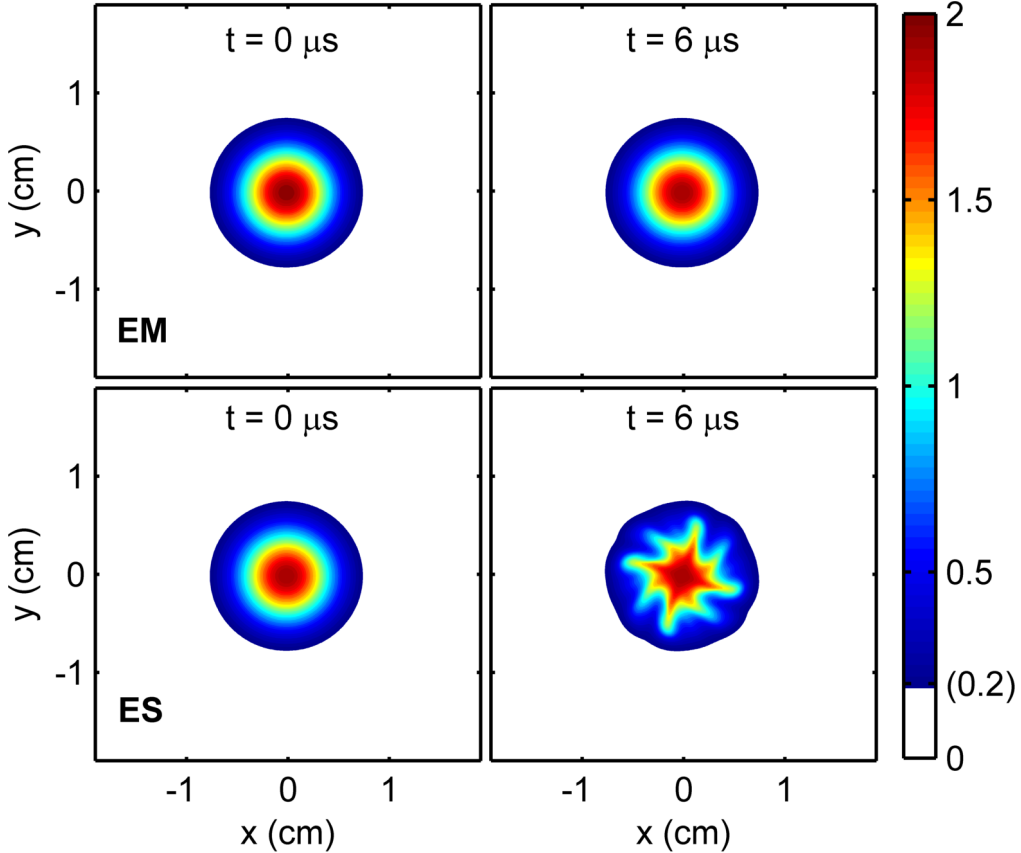


Figure 2.8: Blob density (\tilde{n}/n_0) contours of high-beta plasma from EM (top) and ES (bottom) models. The electrostatic model shows resistive drift wave. The effective gravity force is suppressed for simplicity.

models, we can see that the most unstable normalized perpendicular and parallel wave numbers are higher in the case of electromagnetic model. The dependencies of most unstable parallel wave numbers, which correspond to maximum growth rates, and resistivity are found to be $(\Omega_A)_{\gamma_{\max}} \sim \max[\Omega_R, \tilde{\beta}^{-1}]^{1/2}$. For $\tilde{\beta}^{-1} > 1$, the most unstable perpendicular wave number is $(\chi)_{\gamma_{\max}} \sim 1$, and for the conditions $\tilde{\beta}^{-1} < 1$ and $\Omega_R < 1$, the empirical relation is found to be $(\chi)_{\gamma_{\max}} \sim \Omega_R^{-1/2}$.

We note that in our analysis we assume zero ion temperature. In practice, ion temperature in edge plasma is often larger than electron one. Therefore, finite Larmor radius effect can become important for $\tilde{\beta}^{-1} < 1$ and $\Omega_R < 1$ where perpendicular wave length of the most unstable mode is relatively small.

Meanwhile, the electron inertial term can also make the dispersion relation have imaginary roots. The condition which increases the electron inertial effect will be achieved with high T_e but relatively low- β so that both $\Omega_R \chi^2 < \Omega$ and $\tilde{\beta}^{-1} \chi^2 \gg 1$ conditions are satisfied. In this case, the maximum growth rate of electron inertial instability is found to be $\gamma/\hat{\omega}_* \sim 0.3$ at $\Omega_A^2 \tilde{\beta} \sim 0.5$ with $\chi \sim 1$.

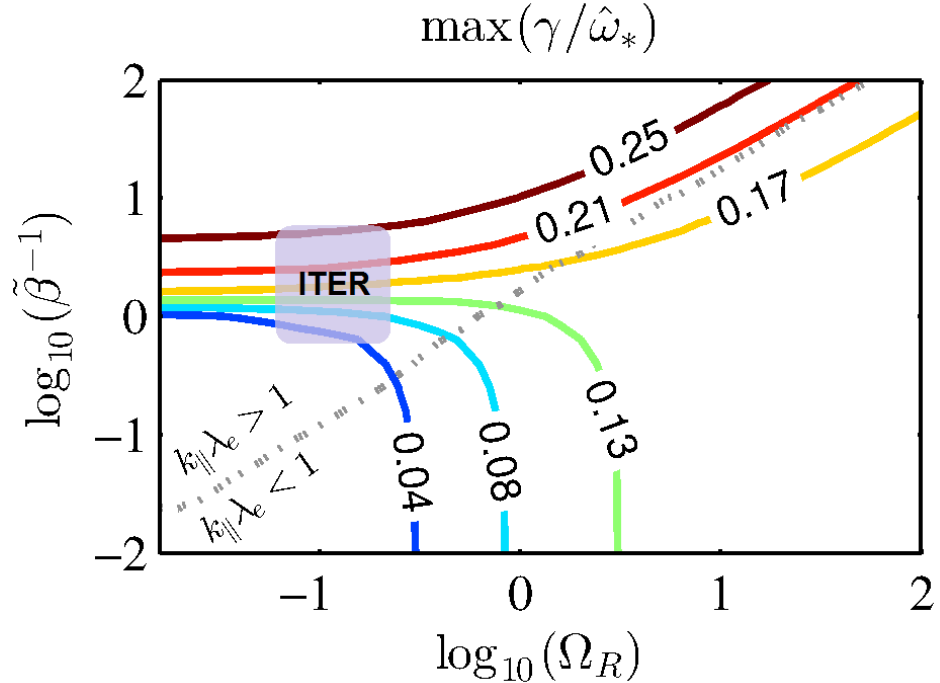


Figure 2.9: Contour lines of normalized maximum growth rate as function of resistivity and $\tilde{\beta}^{-1}$ and a line (dotted) $k_{\parallel} \lambda_e = 1$ with respect to $\Omega_A(\gamma_{\max})$.

Figure 2.9 shows the normalized maximum growth rate as a function of resistivity and plasma beta. The figure reveals three distinct instability regimes: Electromagnetic drift-Alfvénic suppression regime, electron inertial instability regime and electrostatic resistive drift wave instability regime. For high temperature ($\Omega_R \ll 1$) and high pressure ($\tilde{\beta} \gg 1$) regime, electromagnetic effects reduce the growth rate of the resistive drift wave instability. However, the electron inertial dissipation increases the growth rate of the electron inertial instability for relatively low pressure regime ($\log_{10} \tilde{\beta}^{-1} > 0$). In the high temperature regime, the density determines whether the drift wave instability become

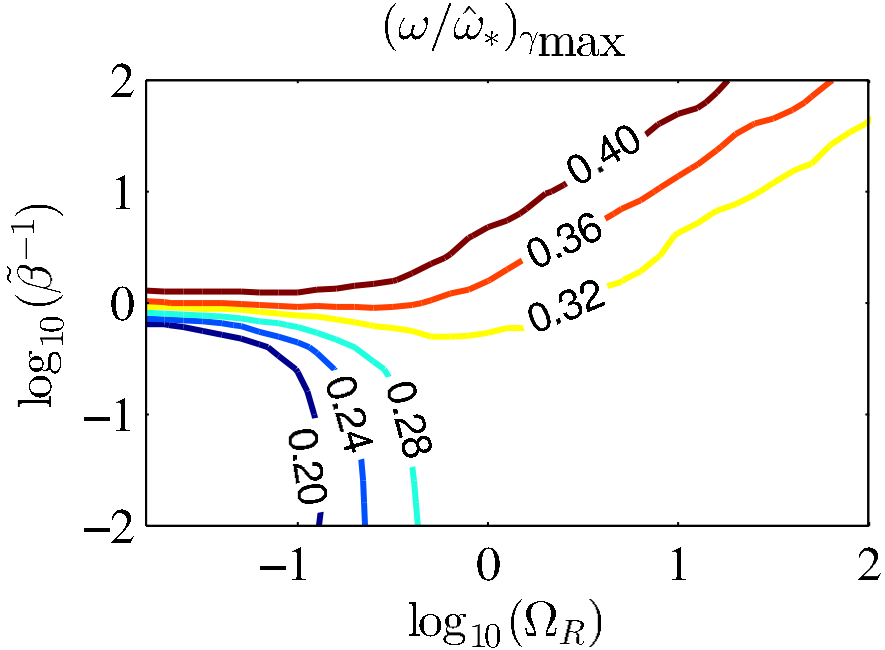


Figure 2.10: Contour lines of normalized real frequency of the corresponding maximum growth rate (Fig.2.9) as function of resistivity and $\tilde{\beta}^{-1}$.

suppressed or the electron inertial instability becomes unstable. For the electromagnetic regime $T_e > (B^2\delta)^{(1/3)}$, the electron inertial instability becomes important if the density is lower than certain value,

$$n < n_{\text{crit}}[\text{cm}^{-3}] \equiv 6.75 \times 10^{14} \frac{B[\text{T}]^2}{T_e[\text{eV}]} \quad (2.17)$$

When electron temperature decreases, we get the electrostatic resistive drift instability regime with the dominate resistive term.

We note that a range of plasma parameters, from the typical SOL plasmas ($T \sim 100 \text{ eV}$, $n \sim 3 \times 10^{13} \text{ cm}^{-3}$) for ITER[53] to some enhanced parameters with density ($n \sim 1 \times 10^{14} \text{ cm}^{-3}$) considering the ELM event, presents somewhat marginal regime between the two electromagnetic regimes. This suggests that turbulence produced blobs within the relatively less dense background plasmas are likely to have electron inertial instability while high-density plasmas from the ELM crash

or from pellet ablation will be less unstable. However, when the plasma is resistive, $\Omega_R \gg 1 + \tilde{\beta}^{-1}$, both electromagnetic suppression and the electron inertial instability effects become negligible and the system reduced to an electrostatic one. (See Fig. 2.11).

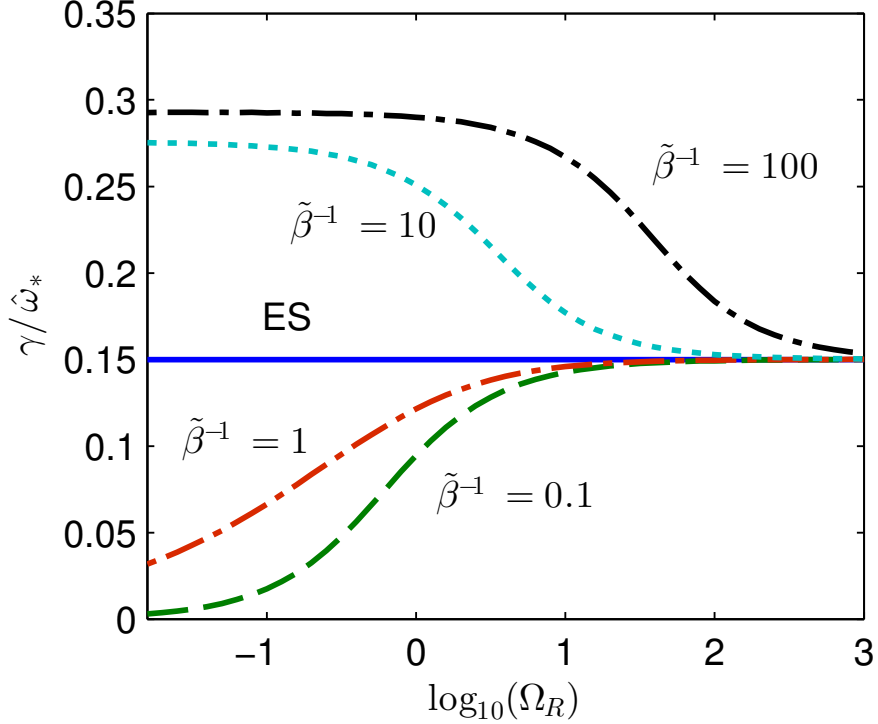


Figure 2.11: Maximum normalized growth rate $\gamma/\tilde{\omega}_*$ as a function of resistivity parameter Ω_R for electromagnetic blobs of four different values of $\tilde{\beta}^{-1} = 0.1, 1.0, 10, 100$ and electrostatic blob with electron inertia neglected (blue solid line).

There are some limitations on the applicability of the fluid approximation on electromagnetic regimes. First of all, the mean free path along the field line should be shorter than parallel wave length of the most unstable wave to make the fluid equations valid. In terms of stability analysis, this collisionality condition, $k_{\parallel, \gamma_{\max}} \lambda_e < 1$ (Fig. 2.9), sets more severe restriction to the validity of fluid approximation $\lambda_e/L \ll 1$. For example, if we use the relation $k_{\parallel, \gamma_{\max}} \lambda_e = \tilde{\beta}^{-1/2} (\Omega_A)_{\gamma_{\max}} / \Omega_R < 1$ with $(\Omega_A)_{\gamma_{\max}} \sim \max[\Omega_R, \tilde{\beta}^{-1}]^{1/2}$, then the required density for fluid approximation is $n[\text{cm}^{-3}] > 3 \times 10^{10} T_e[\text{eV}]^2 / \delta[\text{cm}]$. This relation has second order dependency in electron temperature. Considering

high temperature ($T_e > 100$ eV), the validity of fluid approximation in the stability analysis is questionable for typical densities in the SOL region.

Moreover, the collisionality condition regarding the ratio of the collision frequency to the wave frequency for the maximum growth rate ($v/\omega_{\gamma_{\max}} \gg 1$) is also required for the validity of fluid approximation. Because the wave frequency for the maximum growth rate is comparable to the drift frequency, $\omega_{\gamma_{\max}} \lesssim \hat{\omega}_*$, the collisionality condition becomes approximately $v/\hat{\omega}_* > 1$. This condition also results in similar density requirement as $k_{\parallel}\lambda_e < 1$ condition for the fluid approximation.

Consequently we remark that the kinetic approach is needed for more realistic analysis on the dynamics of SOL region and the kinetic effects may modify the stability of plasma away from the estimation made by fluid approximation.

It should be noted that the kinetic effects, such as Landau damping, are missing in our fluid approximation. Meanwhile, for the case where drift wave instability is related to the effects of electron inertia the ratio of the parallel wave phase speed of the most unstable mode to the electron thermal speed is $(v_{\text{ph}}/v_{Te})_{\gamma_{\max}} = (\Omega)_{\gamma_{\max}}/(\Omega_A)_{\gamma_{\max}}$, where the normalized frequencies $(\Omega)_{\gamma_{\max}} \sim 0.44$ and $(\Omega_A)_{\gamma_{\max}} \sim 0.71(\tilde{\beta}^{-1})^{1/2}$. For the case of $\tilde{\beta} \ll 1$, where the electron inertial effects dominate, the Landau damping effect is minimized. However, for the marginal plasma pressure $\tilde{\beta} \sim 1$, the waves with comparable magnitudes of wave phase velocity and electron thermal speed are susceptible to the Landau damping.

2.5 Discussion

We have demonstrated that there are two different types of electromagnetic effects on the high- β blob dynamics: one is the macroscopic field line bending and the other is the modification of microscopic instability. High- β filament with inhomogeneity along the field line (non-uniform curvature and density intensity or sheath boundary condition) makes such bowing of plasma filament

and magnetic field lines. The implications of the bending of large pressure plasma is also represented in Ref. [41]. As stressed in Ref. [41], the bending motion of such high- β filaments can enhance heat exchange between the plasma facing materials and the inner region of SOL forming parallel heat conduction channel.

The coherency of the filament with high temperature depends on the plasma density. According to Sec. 2.4, the plasma in ITER will be in the electromagnetic region (See Fig. 2.9) with reduced resistivity and its stability is determined by the drift-Alfvén wave or the electron inertial instability according to the density relations in Eq. (2.17). However, the effective gravity force is neglected in Sec. 2.4 in order to focus on how the drift wave instability is affected by electromagnetics. This assumption is only valid when the growth rate of instability for blob dissipation is larger than a critical time rate of the blob shape deformation due to the macroscopic effective gravitational force, i.e. $\gamma\tau_m > 1$. The critical blob macroscopic deformation time[55] is $\tau_m \sim (\tilde{n}_b\delta/(n_0g))^{1/2}$ for the case of no sheath dissipation effects. Then the condition for the negligible macro-dynamics is

$$\frac{\gamma}{\hat{\omega}_*} > \sqrt{\frac{n_0}{\tilde{n}_b} \frac{2\delta}{R}}. \quad (2.18)$$

Unless the resistive drift wave instability drive is reduced by large density such as filaments density created by pellet ablation, the condition (Eq. (2.18)) is usually satisfied for most filamentary structures envisioned for edge plasmas. For high- β blobs with reduced growth rate, however, the blobs will experience fast macroscopic deformation due to non-uniformities of blob density and effective gravity rather than due to microscopic dissipation.

High- β filaments with reduced growth rate can become more unstable by entering either the electron inertia regime or the electrostatic regime. The blob can move to the electron inertia regime as the blob pressure is reduced due to macroscopic deformation, and to the electrostatic regime as the temperature is decreased by heat conduction or by other energy loss processes such as inelastic

electron collisions with neutrals/impurities in far SOL. As the filament transits to the unstable regimes, cross-field heat conduction will be enhanced by stochastic fields due to the instabilities. See Fig. 2.12 for an example of such stochastic field lines.

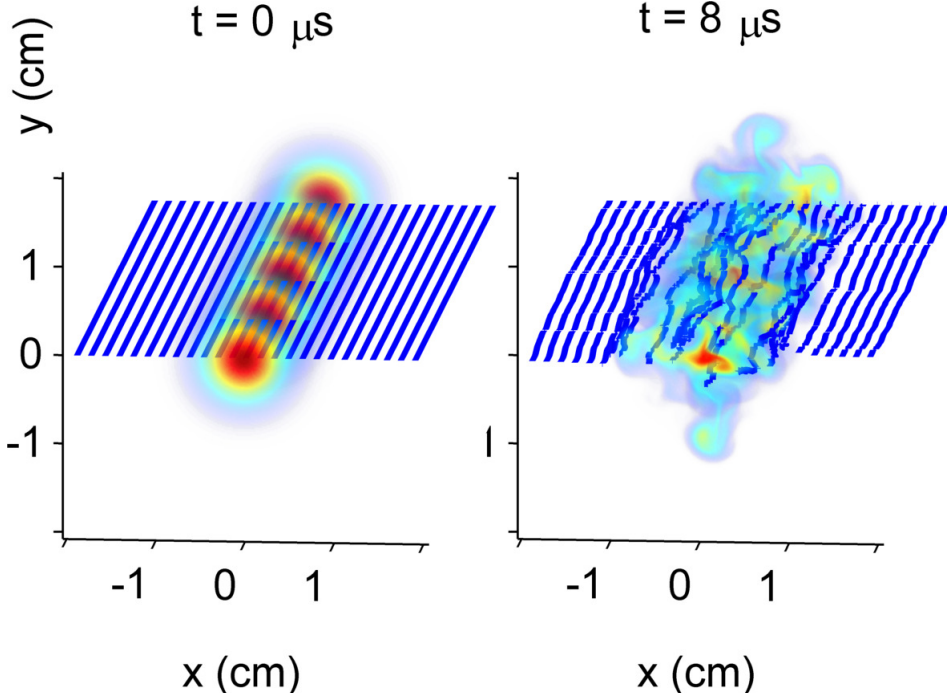


Figure 2.12: Stochastic magnetic field lines are calculated during the electron inertial instability with slightly reduced $\tilde{\beta}$. The electron temperature and density are $T_e = 200$ eV and $n_0 = 3 \times 10^{13} \text{ cm}^{-3}$ respectively.

Although our model was able to show some electromagnetic effects on high- β filamentary structures, there are still some features remained to be added to describe ELM filaments. First of all, the ELM filaments can carry significant amount of unidirectional plasma currents taken from the pedestal region.[56, 57, 58, 18] The ELM filaments carrying the zeroth order currents will also drift with order of $E \times B$ drift velocity in the curvature dominated zone.[44] However, the ELM filament can be influenced by repulsive magnetostatic forces from their current hole pair near edge or the image current near the wall chamber.[44] The current carrying ELM filaments will show greater coherency due to the attraction of parallel currents within the structure, but may also allow other

instabilities in three dimensions.[44, 18]

Moreover, ELM filaments can involve large amplitude bursts of plasmas. Such large amplitude filament simulation would require a nonlinear solution for the electric potential from the vorticity without using the Boussinesq approximation. A fully nonlinear simulation with the large blob-ambient plasma density ratio will produce Alfvén waves slowly propagating inside the filament surrounded by stiff magnetic fields due to dilute background density. Finally, we want to mention that a consideration of increased plasma temperature would require a kinetic rather than a fluid approach.

2.6 Conclusion

Electromagnetic blob-filaments properties were studied for high- β plasmas conditions relevant to ITER parameters. Governing equations based on the vorticity, density, and parallel component of vector potential equation are considered under assumptions of isothermal electron, cold ion temperature and also Boussinesq approximation with moderate blob-ambient plasma density ratio. Using BOUT++ simulations, we demonstrate the boundary effects on the part of the blob away from the boundary are reduced by the extended Alfvén time scale in high- β filaments. We also show that high pressure plasma filament can exhibit macroscopic bending along with the magnetic field lines because of delayed propagation of polarized potential.

The stability characteristics of plasma filaments with high electron temperature are modified by electromagnetic effects. The linear stability analysis shows that only a small growth rate proportional to resistivity remains for high beta regime. For relatively low beta regime, the electron inertial instability dominates for high temperature blobs. However, the electromagnetic regime reverts to electrostatic as the plasma temperature decreases.

The work presented in this chapter is a reprint of the material as it appears in *Electromagnetic*

effects on dynamics of high-beta filamentary structures in Physics of Plasmas 22, 012505 by Wonjae Lee, Maxim V. Umansky, J. R. Angus, and Sergei I. Krasheninnikov, 2015. The dissertation author was the primary investigator and author of this paper.

Chapter 3

Electromagnetic Drift Waves Dispersion for Arbitrarily Collisional Plasmas

The impacts of the electromagnetic effects on resistive and collisionless drift waves are studied. A local linear analysis on an electromagnetic drift-kinetic equation with BGK-like collision operator demonstrates that the model is valid for describing linear growth rates of drift wave instabilities in a wide range of plasma parameters showing convergence to reference models for limiting cases. The wave-particle interactions drive collisionless drift-Alfvén wave instability in low collisionality and high beta plasma regime. The Landau resonance effects not only excite collisionless drift wave modes but also suppress high frequency electron inertia modes observed from an electromagnetic fluid model in collisionless and low beta regime. Considering ion temperature effects, it is found that the impact of finite Larmor radius effects significantly reduce the growth rate of the drift-Alfvén wave instability with synergistic effects of high beta stabilization and Landau resonance.

3.1 Introduction

The plasma boundary region, which includes a scrape-off layer (SOL) and somewhere inside the last closed flux surface (edge region), in the magnetic fusion device has unique and important features [59]. Due to the fact that the boundary plasma region is where the hot, dense core plasmas are connected to material surfaces of the main chamber wall and divertor plates, the edge region has large variations of plasma parameters [60]. In this boundary plasma region with large gradient of plasma parameters, anomalous convective transport and various instability physics become especially important [17, 18].

The relation between the dynamics of coherent turbulent structures and the instabilities of plasma has been extensively studied. The meso-scale turbulent convective structures form filamentary shapes extended along the magnetic field lines and they are usually observed in the SOL region of the magnetic confinement devices [16, 17, 18]. The coherent plasma structures are often called “blobs” because they are spatially localized in the poloidal plane exhibiting enhanced density concentration. The effects of electrostatic (ES) and electromagnetic (EM) drift waves on the blobs were studied in Refs. [28, 61, 62, 63]. In addition, the process of the nonlinear saturation of edge instabilities can generate the blob and ELM filaments [18, 64, 65].

The onset of the electrostatic resistive drift wave instability can substantially limit the coherency of the blobs [28]. However, in Ref. [61, 39] it was shown that the dominant unstable drift wave modes that effect plasma blobs were found to exist in parameter regimes where the validity of the fluid equations are only marginally satisfied. The effects of electrostatic drift wave instability that is not limited by the fluid approximation was considered using the drift-kinetic equation with a BGK-like collision operator [39].

Furthermore, the electromagnetic effects of the drift-Alfvén wave instabilities for coherent structures with high- β ($\beta \equiv 8\pi nT/B^2$) plasmas, such as Edge Localized Mode (ELM) filaments or

blobs in future magnetic confinement devices, have been investigated considering electromagnetic fluid equations [62, 63]. The growth rates of the most unstable modes of the high- β and high-density plasma filaments are decreased by electromagnetic stabilizing effects. For the high-temperature with moderate beta ($\tilde{\beta}_e = 8\pi n T_e M_i / (B^2 m_e) \lesssim 1$) regime, the EM fluid equations predict another type of instability related with electron inertial effects [63].

However, the regime where the electromagnetic fluid description is valid are rather limited in narrow ranges of plasma parameters where high-beta and high-collision conditions are satisfied simultaneously (e.g. see region (c) of Fig. 3.1). Even though the electromagnetic fluid description can depict some effects such as electromagnetic stabilization in high-beta regime, the kinetic effects such as wave-particle interactions are not assessed properly in high temperature environments. Therefore, an electromagnetic-kinetic description is required for the ELM filaments or blobs in the future devices, because those filamentary structures will have the low collisionality and high-beta. Moreover, as the plasma temperature decreases in the course of blob convection, a general model with collision operator is required to describe the arbitrary collisionality and the high beta effects together.

In this paper, we present a general form of wave dispersion relation for the electromagnetic and arbitrarily collisional plasmas. The parallel electron dynamics is described by an electromagnetic drift-kinetic equation with a BGK-like collision operator [39, 40]. The growth rates from the general form of electromagnetic dispersion relation are compared with growth rates from the electrostatic approximation. We also compare the growth rates with the ones from the collisionless and collisional (fluid) limits and observe that the general electromagnetic model converges to simplified models as the plasma parameters (plasma beta, collisionality) approach the limiting cases. Furthermore, the impacts of finite ion temperature on the micro-instabilities are also considered for the edge-SOL plasmas where $T_i > T_e$ is typical [18].

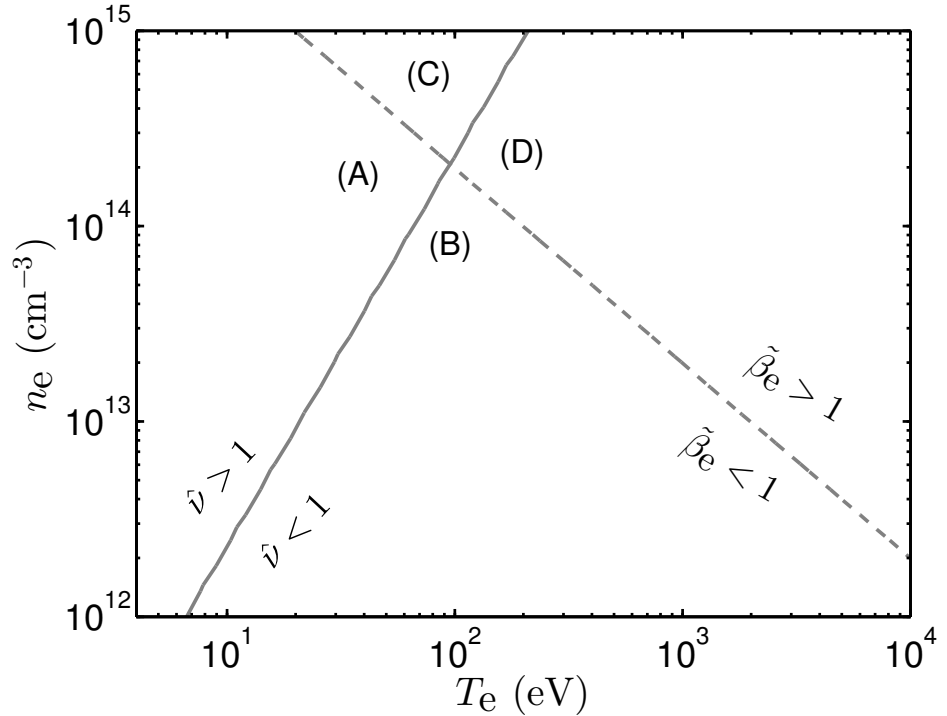


Figure 3.1: Plasma regimes for drift wave instabilities in different beta, $\tilde{\beta}_e = 8\pi n T_e M_i / (B^2 m_e)$ and collisionality, $\hat{v} = 2v\delta/c_s$. The density gradient scale length of deuterium plasma was set to $\delta \sim 1$ cm. The magnetic field strength was considered to be $B = 5.4$ T. Two contour lines for $\hat{v} = 1$ (solid) and $\tilde{\beta}_e = 1$ (dashed) divide the edge plasmas into four different regimes where four limiting models are valid: (A) Electrostatic (ES)-Fluid, (B) ES-Kinetic, (C) Electromagnetic (EM)-Fluid and (D) EM-Kinetic regime.

The paper is organized as follows: In Section 3.2, the model equations used to derive wave dispersion relations are presented; The impacts of electromagnetic perturbations and Landau resonance effects are considered in Section 3.3; The finite ion temperature effects on drift wave instability are discussed in Section 3.4; Conclusions are presented in Section 3.5.

3.2 Model Equations and Derivation of Dispersion Relations

We present a general form of dispersion relations for drift-waves in electromagnetic and arbitrary collisional plasmas. We find expressions for linear perturbations of electron and ion densities, \tilde{n}_e and \tilde{n}_i , in terms of electric potential perturbation, $\tilde{\phi}$. Using quasi-neutrality condition, these electron and ion response equations are equated for the dispersion relation. Because we are mainly interested in low frequency waves, $\omega \sim \omega_* = cT_e k_y / (eB\delta) \ll \omega_{pe}$, which affect both electron and ion dynamics, high frequency electron waves related with the electron plasma frequency, $\omega_{pe} = (4\pi n_e e^2 / m_e)^{1/2}$, are neglected simply by using quasi-neutrality approximation.

A local linear analysis is performed considering a three-dimensional Cartesian geometry with z -coordinate aligned to magnetic field, \mathbf{B} , and y -coordinate correspond to the effective poloidal direction. The plasma density is considered to be exponentially decreasing with scale length of $\delta = -[\partial \ln n_0 / \partial x]^{-1}$ in non-periodic x -direction as an effective radial coordinate. Additionally, the background plasma flow is taken to be zero.

3.2.1 Kinetic description of electrons

For the arbitrary collisional electrons in finite-beta plasmas, we use the following electro-magnetic drift-kinetic equation with BGK-like collision operator,[39, 40]

$$\frac{\partial f}{\partial t} + \mathbf{V}_E \cdot \nabla f + v_{\parallel} \nabla_{\parallel} f + a_{\parallel} \frac{\partial f}{\partial v_{\parallel}} = -\nu(f - f_M) \quad (3.1)$$

where f is the gyro-phase independent electron distribution function; $\mathbf{V}_E = c\hat{\mathbf{b}} \times \nabla\phi/B$ is the $E \times B$ drift velocity; $a_{\parallel} = (e/m_e)[\nabla_{\parallel}\phi + (1/c)\partial A_{\parallel}/\partial t]$ is the electron acceleration in parallel direction due to electrostatic potential and vector potential. The gradient operator in parallel direction, $\nabla_{\parallel} = \partial/(\partial z) + (\nabla A_{\parallel}/B_0) \times \hat{\mathbf{b}}_0 \cdot \nabla$, has been modified by electromagnetic field line bending. $f_M = n_e \exp[-v^2/(2v_e^2)]/(\sqrt{2\pi v_e^2})^3$ is the Maxwellian distribution function which considered as a equilibrium state of electron distribution, where $v_e = \sqrt{T_e/m_e}$ is the electron thermal speed. The collision operator on the right hand side of Eq. (3.1) leads to the equilibration of any perturbed distribution and the Maxwellian distribution by electron-ion collision processes. The electron-ion collision frequency is $\nu = 0.51/\tau_e$, and $\tau_e = 3.44 \times 10^5 T_e^{3/2}/(n_e \ln \Lambda)$ is the electron-ion collision time.

Assuming linear perturbations to be following $\exp[i k_{\parallel} z + i k_y y - i \omega t]$, the linearized form of Eq. (3.1) is

$$\tilde{f} = \frac{(\omega - k_{\parallel} v_z) \frac{e\tilde{\phi}}{T_e} f_{M0} - (\omega - \omega_*) \frac{e}{T_e} (\tilde{\phi} - \frac{v_z}{c} \tilde{A}_{\parallel}) + i\nu \tilde{f}_M}{(\omega + i\nu) - k_{\parallel} v_z}, \quad (3.2)$$

where f_{M0} is unperturbed background Maxwellian, $\tilde{\phi}$, \tilde{A}_{\parallel} are perturbed potentials, and \tilde{f}_M is a

perturbed Maxwellian distribution,

$$\tilde{f}_M = \left(\frac{\tilde{n}_e}{n_0} + \frac{1}{2} \left(\frac{v^2}{v_e^2} - 3 \right) \frac{\tilde{T}}{T_e} \right) f_{M_0}, \quad (3.3)$$

where \tilde{n}_e and \tilde{T} are perturbed electron density and temperature, respectively.

The electron distribution tends to the Maxwellian function by collisional friction of electrons with stationary ions and by collisional relaxation between electrons. Therefore, the linearized model collision operator, $-\mathbf{v}(\tilde{f} - \tilde{f}_M)$, represents both the frictional loss of momentum and the thermal energy relaxation. The model collision operator does not conserve the electron momentum by transferring it to the ion species with collisional friction momentum exchange rate, $\int [-\mathbf{v}m_e \mathbf{v}_\parallel (\tilde{f} - \tilde{f}_M)] d\mathbf{v}$, given the relaxation time \mathbf{v}^{-1} . However, the thermal energy transfer may be ignored because the thermal energy exchange rate between electrons and ions is slower than the momentum exchange rate by factor of $m_e/M_i \ll 1$. Therefore, the linearized collision operator has the desired property of conserving electron density and thermal energy density because the collision operator satisfies $\int [-\mathbf{v}(\tilde{f} - \tilde{f}_M)] d\mathbf{v} = 0$ and $\int [-\mathbf{v}\mathbf{v}^2(\tilde{f} - \tilde{f}_M)] d\mathbf{v} = 0$ [39].

The linear perturbation of electron density is obtained by integrating Eq. (3.2). Because the perturbed distribution function contains four variables, $(\tilde{n}_e, \tilde{\phi}, \tilde{T}, \tilde{A}_\parallel)$, we need three equations to find the relation between the density perturbation response to electric potential perturbation. We follow the same procedure described in Ref. [39] to handle the temperature perturbation dependency by taking the zeroth and second velocity moments of Eq. (3.2). The extra terms with vector potential perturbation are solved by considering the first velocity moment relation, $\frac{c}{4\pi e} \nabla_\perp^2 \tilde{A}_\parallel = \int v_\parallel \tilde{f} d\mathbf{v}$, which comes from Ampere's law. Solving the zeroth, first and second velocity moment equations together (see appendix A), we get the following density response to a electric potential perturbation in the

electromagnetic arbitrary collisional plasma,

$$\frac{\tilde{n}_e}{n_0} = \frac{g_{1*} g_2 - i\check{v} g_3 g_{4*}}{g_1 g_2 - i\check{v} g_3 g_4} \frac{e\tilde{\Phi}}{T_e}, \quad (\text{EM Kinetic Collisional}) \quad (3.4)$$

where g_n ($n = 1, 2, 3, 4, 1_*, 4_*$) are:

$$g_1 = h_1 C_1 - i\check{v} (\check{\omega} - \check{\omega}_*) \varepsilon^2, \quad (3.5)$$

$$g_{1*} = h_{1*} C_1 - (\alpha - \check{\omega}_*) (\check{\omega} - \check{\omega}_*) \varepsilon^2, \quad (3.6)$$

$$g_2 = h_2 C_1 - i\check{v} C_2 \alpha h_3, \quad (3.7)$$

$$g_3 = h_3 C_1 - h_3 \alpha (\check{\omega} - \check{\omega}_*) \varepsilon, \quad (3.8)$$

$$g_4 = h_4 C_1 - i\check{v} C_2 \varepsilon, \quad (3.9)$$

$$g_{4*} = h_{4*} C_1 - (\alpha - \check{\omega}_*) C_2 \varepsilon, \quad (3.10)$$

where ε is defined as $\varepsilon \equiv 1 + \alpha Z(\alpha)$, $Z(\alpha) = (1/\sqrt{\pi}) \int_{-\infty}^{\infty} \exp(-x^2)/(x - \alpha) dx$ is the plasma dispersion function with normalized complex frequency, $\alpha \equiv \check{\omega} + i\check{v} = (\omega + iv)/(\sqrt{2}v_e k_{\parallel})$. The “check” notation is used on the variables (ω, v, ω_*) to represent the normalizations with the frequency $\sqrt{2}v_e k_{\parallel}$. The coefficient C_1 and C_2 , which originated from the first and second velocity moments, are expressed as following,

$$C_1 = -\frac{\chi^2}{\tilde{\beta}_e} + (\check{\omega} - \check{\omega}_*) \alpha \varepsilon, \quad (3.11)$$

$$C_2 = (\check{\omega} - \check{\omega}_*) \left(\frac{3}{2} + \alpha^2 + \alpha Z(\alpha) + \alpha^3 Z(\alpha) \right), \quad (3.12)$$

where $\chi = k_y \rho_s$ is the normalized perpendicular wave number and $\rho_s = c \sqrt{T_e M_i} / (eB)$ is the gyro-

Bohm radius. Equations (3.5-3.10) contain the following electrostatic coefficients,

$$h_1 = 1 + i\check{v}Z(\alpha), \quad (3.13)$$

$$h_{1*} = 1 + (\alpha - \check{\omega}_*)Z(\alpha), \quad (3.14)$$

$$h_2 = \frac{3}{2} + i\check{v}(\alpha + \alpha^3 + \frac{1}{2}Z(\alpha) + \frac{\alpha^2}{2}Z(\alpha) + \alpha^4Z(\alpha)), \quad (3.15)$$

$$h_3 = \alpha + \left(\alpha^2 - \frac{1}{2}\right)Z(\alpha), \quad (3.16)$$

$$h_4 = \frac{3}{2} + i\check{v}[\alpha + (1 + \alpha^2)Z(\alpha)], \quad (3.17)$$

$$h_{4*} = \frac{3}{2} + (\alpha - \check{\omega}_*)[\alpha + (1 + \alpha^2)Z(\alpha)]. \quad (3.18)$$

One can show that the electrostatic approximation[39] of Eq. 3.2 results in

$$\frac{\tilde{n}_e}{n_0} = \frac{h_{1*}h_2 - i\check{v}h_3h_{4*}}{h_1h_2 - i\check{v}h_3h_4} \frac{e\tilde{\phi}}{T_e}. \quad (\text{ES Kinetic Collisional}) \quad (3.19)$$

This relation can also be obtained from Eq. (3.4) by dividing both numerator and denominator by C_1^2 and letting $\tilde{\beta}_e \rightarrow 0$.

For collisionless limit ($\check{v} \rightarrow 0$), we get the electromagnetic kinetic collisionless electron density perturbation,

$$\frac{\tilde{n}_e}{n_0} = \left[1 + (\check{\omega} - \check{\omega}_*)Z(\check{\omega}) + \frac{(\check{\omega} - \check{\omega}_*)^2(1 + \check{\omega}Z(\check{\omega}))^2}{\frac{\chi^2}{\tilde{\beta}_e} - \check{\omega}(\check{\omega} - \check{\omega}_*)(1 + \check{\omega}Z(\check{\omega}))} \right] \frac{e\tilde{\phi}}{T_e},$$

(EM Kinetic Collisionless) (3.20)

and electrostatic kinetic collisionless electron density perturbation, [39]

$$\frac{\tilde{n}_e}{n_0} = [1 + (\check{\omega} - \check{\omega}_*)Z(\check{\omega})] \frac{e\tilde{\phi}}{T_e}, \quad (\text{ES Kinetic Collisionless}) \quad (3.21)$$

respectively. Note that the third term in the bracket of Eq. (3.20) correspond to the electromagnetic correction which vanishes as plasma pressure decreases.

3.2.2 Fluid description of electrons in collisional limit

The plasma dynamics can also be described by equations using macroscopic variables [66]. We may use the macroscopic variables for density (n_e), momentum ($m_e \mathbf{V}_e$) and temperature (T_e) when the electron distribution function is thermalized by frequent collisions ($v \gg \omega$). Under the fluid approximation, we consider the following three conservation equations,

$$\frac{\partial n_e}{\partial t} + \mathbf{V}_E \cdot \nabla n_e = -\nabla_{\parallel}(n_e V_{\parallel}), \quad (3.22)$$

$$m_e n_e \frac{dV_{\parallel}}{dt} = e n_e \nabla_{\parallel} \phi + \frac{e n_e}{c} \frac{\partial A_{\parallel}}{\partial t} - \frac{0.51 m_e n_e}{\tau_e} V_{\parallel} - \nabla_{\parallel} P_e - 0.71 n_e \nabla_{\parallel} T_e, \quad (3.23)$$

$$\frac{3}{2} \frac{\partial T_e}{\partial t} + T_e \nabla_{\parallel} V_{\parallel} = -\frac{1}{n_e} \nabla_{\parallel} (0.71 n_e T_e V_{\parallel} - \kappa_{\parallel}^e \nabla_{\parallel} T_e), \quad (3.24)$$

where $V_{\parallel} = \mathbf{V}_e \cdot \hat{\mathbf{b}}_0$ is the parallel component of fluid velocity, $P_e = n_e T_e$ is the pressure of the electron fluid, and $\kappa_{\parallel}^e = 3.16 n_e T_e \tau_e / m_e$ is the parallel electron thermal conductivity.

Eqs. (3.22-3.24) are similar to the fluid descriptions for electrons in Ref. [39]. The differences come from the electromagnetic corrections: the time derivative of parallel vector potential, $\partial A_{\parallel} / \partial t$, and field line bending term in the parallel gradient operator, $\nabla_{\parallel} = \partial / (\partial z) + (\nabla A_{\parallel} / B_0) \times \hat{\mathbf{b}}_0 \cdot \nabla$. The parallel vector potential is calculated by Ampere's law, $J_{\parallel} = -c / (4\pi) \nabla_{\perp}^2 A_{\parallel}$.

Performing the linear analysis considering $n_e = n_0(x) + \tilde{n}_e$, $V_{\parallel} = \tilde{V}_{\parallel}$ and $T_e = T_{e0} + \tilde{T}$, we get the following electromagnetic response expression of electron fluid density,

$$\frac{\tilde{n}_e}{n_0} = \left[\frac{(\omega_* + i\omega_{\parallel}^*) \left(\frac{3}{2}\omega + i\kappa\omega_{\parallel} \right) + i\beta\omega_*\omega_{\parallel}^*}{(\omega + i\omega_{\parallel}^*) \left(\frac{3}{2}\omega + i\kappa\omega_{\parallel} \right) + i\beta\omega\omega_{\parallel}^*} \right] \frac{e\tilde{\phi}}{T_e}, \quad (\text{EM Fluid}) \quad (3.25)$$

with $\kappa = 1.61$, $\beta = (1.71)^2$ (not plasma beta). $\omega_{\parallel} = v_e^2 k_{\parallel}^2 / v$ and $\omega_{\parallel}^* = v_e^2 k_{\parallel}^2 / v_*$ are the characteristic electron parallel diffusion rate and its electromagnetic correction, respectively. As emphasized in Ref. [63], the collision frequency in the electromagnetic fluid equation is modified by electromagnetic terms. The effective collision frequency is

$$v_* = -i\omega - i\omega \frac{\omega_{pe}^2}{c^2 k_{\perp}^2} + i\omega_* \frac{\omega_{pe}^2}{c^2 k_{\perp}^2} + v, \quad (3.26)$$

where the first three terms correspond to the electromagnetic corrections; the first term correlated with the electron inertia, the second term originated from the time derivative of parallel vector potential and the third term derived from the effect of field line bending on plasma thermal forces. Note that the electrostatic approximation of Eq. (3.25) has the same form but with $\omega_{\parallel}^* \rightarrow \omega_{\parallel}$,

$$\frac{\tilde{n}_e}{n_0} = \left[\frac{(\omega_* + i\omega_{\parallel}) \left(\frac{3}{2}\omega + i\kappa\omega_{\parallel} \right) + i\beta\omega_*\omega_{\parallel}}{(\omega + i\omega_{\parallel}) \left(\frac{3}{2}\omega + i\kappa\omega_{\parallel} \right) + i\beta\omega\omega_{\parallel}} \right] \frac{e\tilde{\phi}}{T_e}. \quad (\text{ES Fluid})[39] \quad (3.27)$$

In the electrostatic response expression, Eq. (3.27), the effective adiabatic response is set by only collisions rather than by electron inertia and potential perturbations.

3.2.3 Kinetic Description of Ions

We next consider the Vlasov-Maxwell equation for distribution function of ions. Because of the large gyro radius of ion, we use the full kinetic equation rather then drift-kinetic equation. The perturbed ion distribution is found by integrating the Vlasov equation along the unperturbed orbits [8, 67]. Integrating the perturbed distribution over velocity space we get the following perturbation of ion density,

$$\begin{aligned} \frac{\tilde{n}_i}{n_0} = & -\frac{e\tilde{\phi}}{T_i} - (\omega - \omega_i^*) \frac{e^{-\Lambda_i} I_0(\Lambda_i)}{\sqrt{2}k_{\parallel}v_{T_i}} Z(\xi_i) \frac{e\tilde{\phi}}{T_i} \\ & + (\omega - \omega_i^*) \frac{e^{-\Lambda_i} I_0(\Lambda_i)}{\sqrt{2}k_{\parallel}v_{T_i}} (1 + \xi_i Z(\xi_i)) \frac{e}{T_i} \frac{\sqrt{2}v_{T_i}\tilde{A}_{\parallel}}{c}, \end{aligned} \quad (\text{EM Ion Density Perturbation}) \quad (3.28)$$

where $\xi_i = \omega/(\sqrt{2}k_{\parallel}v_{T_i})$, $\Lambda_i = k_{\perp}^2 \rho_i^2$, $\omega_i^* = -(T_i/T_e)\omega_*$ and I_0 is the modified Bessel function. Note that we have neglected higher order terms assuming $\xi_i > 1$ for simplicity.

The last term in the RHS of Eq. (B.18) represent the impact of electromagnetic perturbation on ions. The relation between the vector potential perturbation and the electrostatic potential perturbation,

$$\frac{\sqrt{2}v_e}{c}\tilde{A}_{\parallel} = H\tilde{\phi}, \quad (3.29)$$

can be found from parallel electron dynamics. The proportional coefficient, H , can be either kinetic, H_K , or fluid, H_F , depending on the model of description that is used for the closure relation. The

representations for the H_K and H_F are found to be

$$H_K = \frac{(h_{1*}h_2 - i\check{v}h_3h_{4*})(h_1\alpha - i\check{v}\epsilon) - (h_1h_2 - i\check{v}h_3h_4)(h_{1*}\alpha - (\alpha - \check{\omega}_*)\epsilon)}{(h_1h_2 - i\check{v}h_3h_4)(C_1 - \alpha(\check{\omega} - \check{\omega}_*)\epsilon) - (h_1\alpha - i\check{v}\epsilon)(i\check{v}h_3C_2 - h_2(\check{\omega} - \check{\omega}_*)\epsilon)}, \quad (3.30)$$

and

$$H_F = -\frac{m_e}{M_i} \frac{2\omega_{pe}^2}{c^2 k_\perp^2} \frac{\sqrt{2}v_e}{2c_s^2 k_\parallel} \frac{i(1 - \omega_*/\omega)}{\left(\frac{1}{\omega_\parallel^*} + \frac{i}{\omega} + \frac{i\beta}{\frac{3}{2}\omega + i\kappa\omega_\parallel}\right)}. \quad (3.31)$$

Because the plasma dispersion function follows $Z(\xi) \sim -1/\xi$ for $\xi \gg 1$, the impact of electromagnetic perturbation on ion dynamics vanishes for high frequency modes, $\omega \gg k_\parallel v_{T_i}$, leading the Eq. (B.18) to depend only on the electrostatic perturbation,

$$\frac{\tilde{n}_i}{n_0} = \frac{T_e}{T_i} \left[-1 - (\omega - \omega_i^*) \frac{e^{-\Lambda_i} I_0(\Lambda_i)}{\sqrt{2}k_\parallel v_{T_i}} Z(\xi_i) \right] \frac{e\tilde{\phi}}{T_e}. \quad (\text{ES Ion Density Perturbation}) \quad (3.32)$$

Eq. (3.32) is also obtained when the vector potential perturbation is neglected for low plasma beta.

So far we have derived linear perturbation relations for electron and ion densities as a function of electric potential. Six different models are used to derive expressions of the electron density perturbations. The most complete model corresponds to Eq. (3.4), the electron density perturbation governed by the electromagnetic drift-kinetic equation with collision term. Its collisionless and collisional (fluid) limit are also considered in Eq. (3.20) and (3.25) respectively. The electrostatic approximations of these three equations are also considered in Eqs. (3.19), (3.21) and (3.27). For ion dynamics, electromagnetic and electrostatic ion density perturbation equations are shown in Eq. (B.18) and (3.32) respectively.

3.2.4 Dispersion Relation and Normalization

For each of the electromagnetic and electrostatic models, the dispersion relation for low frequency waves are found by equating \tilde{n}_e and \tilde{n}_i under quasi-neutral plasma approximation. We adopt the drift wave frequency with $\chi = 1$ as a normalizing parameter [39]. Therefore, we consider following normalizations: $(\hat{\omega}, \hat{v}, \hat{\omega}_\parallel, \hat{\omega}_\parallel^*) = (\omega, v, \omega_\parallel, \omega_\parallel^*) 2\delta/c_s$, $\hat{\omega}_* = 2\chi$, $\hat{k}_\parallel = 2\delta\sqrt{2}v_e k_\parallel/c_s$, $\hat{I}_0 = e^{-\chi^2 T_i/T_e} I_0(\chi^2 T_i/T_e)$, $\hat{\xi} = \sqrt{M_i T_e / (m_e T_i)} \hat{\omega} / \hat{k}_\parallel$.

The electromagnetic dispersion relations, $D(\hat{k}_\parallel, \chi, \hat{\omega}) = 0$, are written for different models as following; for kinetic model with arbitrary collision:

$$D(\hat{k}_\parallel, \chi, \hat{\omega}) = 1 + \left(\hat{\omega} + 2\chi \frac{T_i}{T_e} \right) \frac{\hat{I}_0}{\hat{k}_\parallel} \left(\frac{\hat{\xi} \hat{k}_\parallel}{\hat{\omega}} Z(\hat{\xi}) - (1 + \hat{\xi} Z(\hat{\xi})) H_K \right) + \frac{T_i}{T_e} \frac{\left(g_{1*} g_2 - i \frac{\hat{v}}{\hat{k}_\parallel} g_3 g_{4*} \right)}{\left(g_1 g_2 - i \frac{\hat{v}}{\hat{k}_\parallel} g_3 g_4 \right)}, \quad (3.33)$$

for collisionless limit:

$$D(\hat{k}_\parallel, \chi, \hat{\omega}) = 1 + \left(\hat{\omega} + 2\chi \frac{T_i}{T_e} \right) \frac{\hat{I}_0}{\hat{k}_\parallel} \left(\frac{\hat{\xi} \hat{k}_\parallel}{\hat{\omega}} Z(\hat{\xi}) - (1 + \hat{\xi} Z(\hat{\xi})) H_K \right) + \frac{T_i}{T_e} \left[1 + \left(\frac{\hat{\omega} - 2\chi}{\hat{k}_\parallel} \right) Z(\hat{\omega}/\hat{k}_\parallel) + \frac{\left(\frac{\hat{\omega} - 2\chi}{\hat{k}_\parallel} \right)^2 \left(1 + \frac{\hat{\omega}}{\hat{k}_\parallel} Z(\hat{\omega}/\hat{k}_\parallel) \right)^2}{\chi^2/\tilde{\beta}_e - \frac{\hat{\omega}}{\hat{k}_\parallel} \left(\frac{\hat{\omega} - 2\chi}{\hat{k}_\parallel} \right) \left(1 + \frac{\hat{\omega}}{\hat{k}_\parallel} Z(\hat{\omega}/\hat{k}_\parallel) \right)} \right], \quad (3.34)$$

and for collisional (fluid) limit:

$$D(\hat{k}_\parallel, \chi, \hat{\omega}) = 1 + \left(\hat{\omega} + 2\chi \frac{T_i}{T_e} \right) \frac{\hat{I}_0}{\hat{k}_\parallel} \left(\frac{\hat{\xi} \hat{k}_\parallel}{\hat{\omega}} Z(\hat{\xi}) - (1 + \hat{\xi} Z(\hat{\xi})) H_F \right) + \frac{T_i}{T_e} \frac{(2\chi + i\hat{\omega}_\parallel^*) \left(\frac{3}{2}\hat{\omega} + i\kappa\hat{\omega}_\parallel \right) + i\beta 2\chi\hat{\omega}_\parallel^*}{(\hat{\omega} + i\hat{\omega}_\parallel^*) \left(\frac{3}{2}\hat{\omega} + i\kappa\hat{\omega}_\parallel \right) + i\beta\hat{\omega}\hat{\omega}_\parallel^*}. \quad (3.35)$$

One can show that the dispersion relations for electrostatic models[39] are recovered from the above equations by taking $g \rightarrow h$, $H \rightarrow 0$, $\tilde{\beta}_e \rightarrow 0$ and $\hat{\omega}_\parallel^* \rightarrow \hat{\omega}_\parallel$.

The dispersion relation from the electromagnetic drift-kinetic equation with arbitrary collisionality (Eq. (3.33)) contains three free parameters \hat{v} , $\tilde{\beta}_e$ and T_i/T_e . We solve the dispersion relations numerically for the maximum growth rate, $\hat{\gamma}_{\max}(\hat{v}, \tilde{\beta}_e, T_i/T_e)$, on various plasma parameters, (T_e, n_e) . The normalized plasma beta and collision frequency are considered as input parameters in a non-orthogonal coordinate system which is obtained by a mapping from plasma density and temperature space into the normalized space: $(\log_{10} T_e, \log_{10} n_e) \mapsto (\log_{10} \tilde{\beta}_e, \log_{10} \hat{v})$.

The characteristics of parallel electron dynamics are determined by parameters on the mapped coordinate $(\tilde{\beta}_e, \hat{v})$. The plasma beta $\tilde{\beta}_e$ determines if the system is electromagnetic or electrostatic. And \hat{v} shows whether the system is collisional (fluid) or collisionless (kinetic). On the other hand, T_i/T_e reflects the ion dynamics effects in terms of finite Larmor radius.

3.3 Electromagnetic effects and Landau resonance

We first consider a case when the finite ion temperature is suppressed, $T_i/T_e \rightarrow 0$, to separate the electron dynamics from the ion dynamics. Here, we focus on the parallel electron dynamics in terms of electromagnetic perturbations and the wave-particle interaction effects on the drift wave instability. The maximum growth rates, $\hat{\gamma}_{\max}$, of various models for $T_i/T_e = 0.0001$ are shown in Fig. 3.2. The top row of figure 3.2 shows the contour of maximum growth rate in the electromagnetic models. The solution of dispersion relation from the electromagnetic fluid model (Eq. (3.35)) as a collisional limit of Eq. (3.33) are shown in Fig. 3.2(a). Fig. 3.2(b) shows the growth rates from the electromagnetic collisionless kinetic model (Eq. (3.34)). The third column of the top row, Fig. 3.2(c), represents the result from the model of electromagnetic and kinetic description with collision operator, Eq. (3.33). And finally, the bottom rows are electrostatic counterparts of the

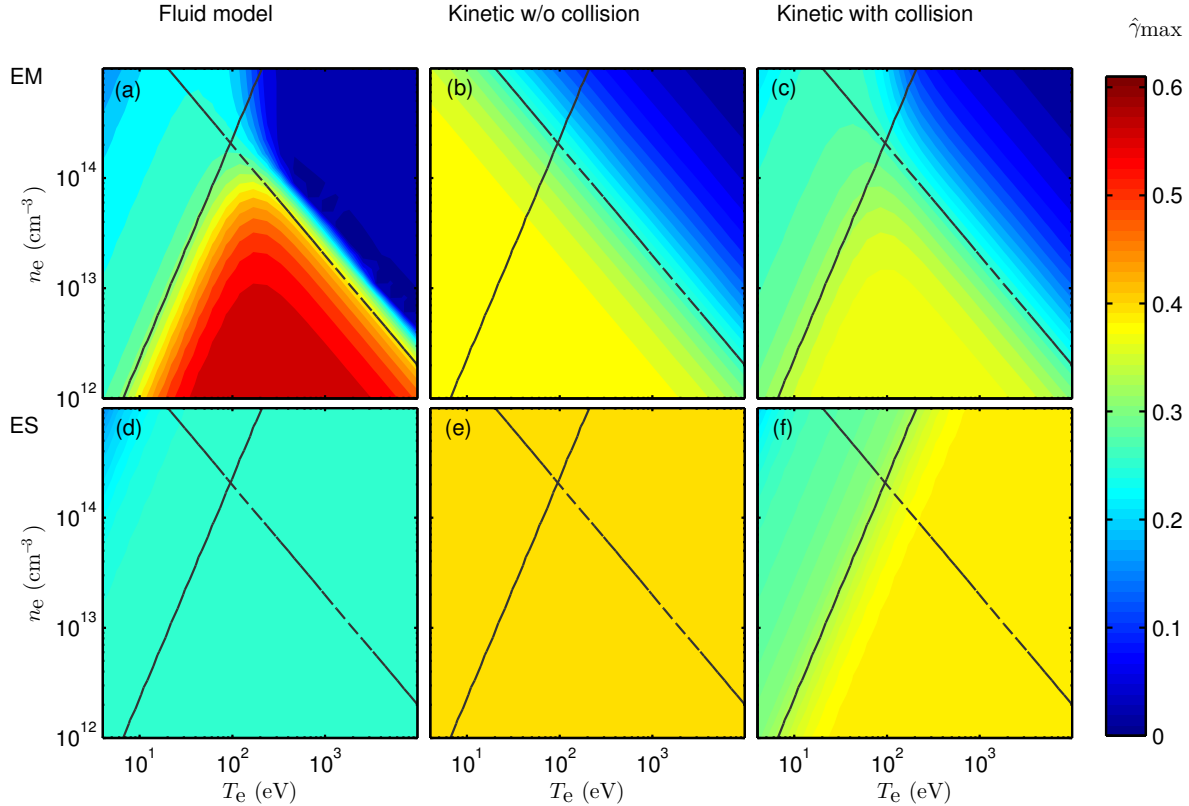


Figure 3.2: Contour plots of normalized maximum growth rates, $\hat{\gamma}_{\max}$, for (a) EM fluid model, (b) EM kinetic collisionless model, (c) EM kinetic with arbitrary collision model, (d) ES fluid model, (e) ES kinetic collisionless model and (f) ES kinetic with arbitrary collision model. The finite ion temperature effect was suppressed here by setting $T_i/T_e = 0.0001$. The solid and dashed line represent the contours for $\hat{\nu} = 1$ and $\tilde{\beta}_e = 1$, respectively.

previous three models.

First of all, comparing the results of Fig. 3.2(a) with those of Fig. 3.2(d), we observe the electromagnetic field perturbation decreases the growth rate of resistive drift wave instability in the EM fluid regime as predicted in Ref. [62, 63]. However, the validity regime of electromagnetic fluid takes only small region in the plasma density and temperature space (the (C) region of Fig. 3.1). If the EM fluid model is applied to collisionless plasmas, the model shows either of the enhancement growth rate or strong electromagnetic suppression of drift wave instability depending on the plasma beta. Due to small contribution of resistivity and negligible electromagnetic frozen-in effect in low- β ,

the electron dynamics from fluid equations results in higher growth rate ($\hat{\gamma}_{\max} \sim 0.6$) than that of electrostatic resistive drift wave ($\hat{\gamma}_{\max} \sim 0.25$).

The high growth rate ($\hat{\gamma}_{\max} \sim 0.6$), shown in the electromagnetic fluid model for the region of $\tilde{\beta}_e < 1$ and $\hat{v} < 1$, is attributed to the electron inertial term, $m_e n_e \partial V_{\parallel} / \partial t$. In the low- β and high temperature region, the electron inertial response becomes the main contribution to the effective collision frequency (Eq. (3.26)). The electron inertial term can make the dispersion relation (Eq. (3.35)) have imaginary roots causing the electron inertial instability [63]. However, the unstable high frequency waves are mostly damped by kinetic effects such as wave-particle interactions (see Fig. 3.2(b) and (c)). Meanwhile, the electrostatic fluid model does not show such high frequency modes, because the inertial term is not included in the electrostatic fluid model [39]. Only electrostatic resistive drift wave instability ($\hat{\gamma}_{\max} \sim 0.25$) occurs for the electrostatic fluid model.

As shown in the Ref. [63], the growth rates from the electromagnetic fluid equations are decreased to negligible value if both of the dissipative terms (electron inertia and resistivity) are decreased to small value in the regime of high beta ($\tilde{\beta}_e \gg 1$) and high temperature plasmas ($\hat{v} \ll 1$) (Fig. 3.2(a)). However, the kinetic effects such as Landau resonance can produce phase shift to cause the drift waves become unstable. The regime of $\hat{v} < 1$ and $\tilde{\beta}_e > 1$ in Fig. 3.2(b) and (c) shows the effects of wave-particle interaction to drive the kinetic drift-Alfvén wave instability. Comparing the growth rate of resistive drift wave instability, $\hat{\gamma}_{\max} \sim 0.25$ (Fig. 3.2(d)), with that of kinetic drift wave instability, $\hat{\gamma}_{\max} \sim 0.4$ (Fig. 3.2(e)), one can notice that the wave-particle resonance effect gives stronger instability drive than the resistivity but less than the electron inertial instability drive in the fluid model.

The wave-particle interaction effects not only drives the instability but may inhibit some high frequency waves from growing unstable by transferring the energy of waves to the kinetic energy of particles. Fig. 3.3 shows the real frequencies of the waves of the most unstable modes. In the ES-

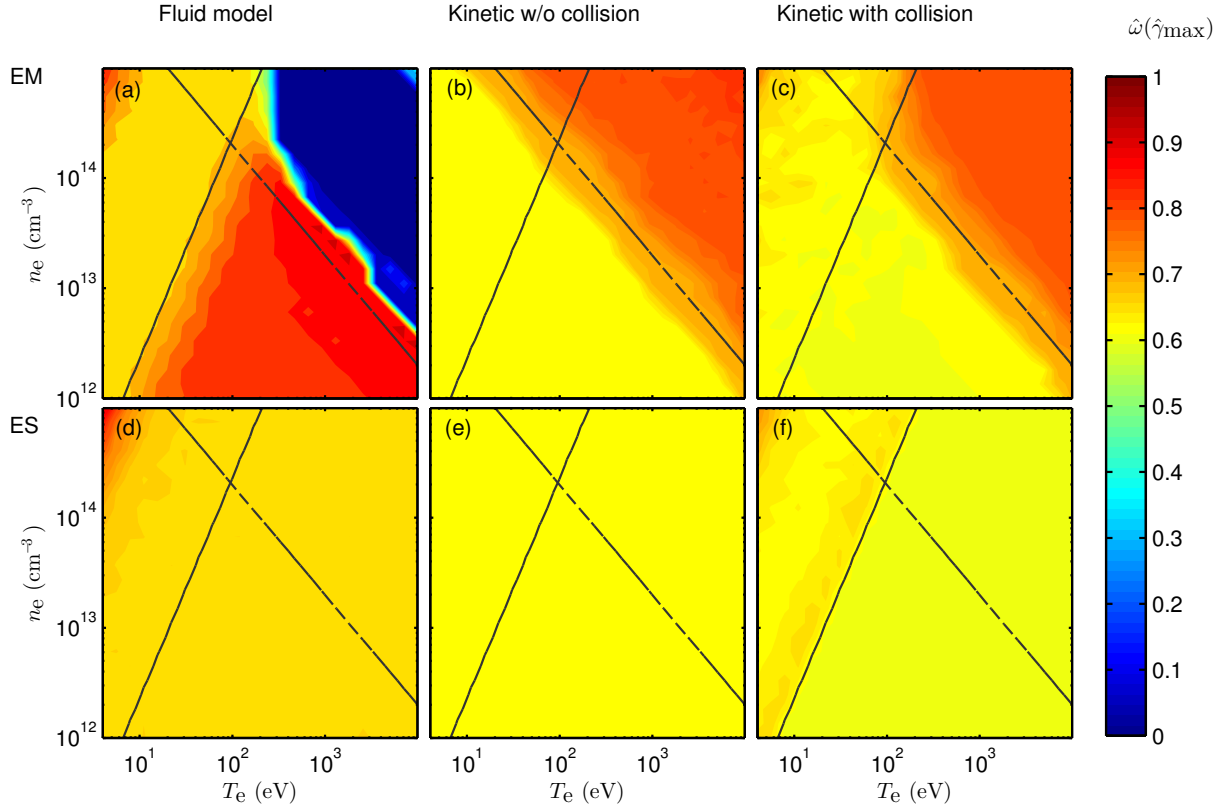


Figure 3.3: Contour plots of real frequency at the maximum growth rate for (a) EM fluid model, (b) EM kinetic collisionless model, (c) EM kinetic with arbitrary collision model, (d) ES fluid model, (e) ES kinetic collisionless model and (f) ES kinetic with arbitrary collision model. The finite ion temperature effect was suppressed here by setting $T_i/T_e = 0.0001$. The solid and dashed line represent the contours for $\hat{v} = 1$ and $\tilde{\beta}_e = 1$, respectively.

kinetic regime ($\hat{v} < 1$ and $\tilde{\beta}_e < 1$), the frequency, $\hat{\omega}(\hat{\gamma}_{\max}) \sim 0.85$, of the electron inertia instability (Fig. 3.3(a)) is higher than that of electrostatic drift wave instability ($\hat{\omega}(\hat{\gamma}_{\max}) \sim 0.65$). The Landau resonance occurs at slightly lower frequency ($\hat{\omega}(\hat{\gamma}_{\max}) \sim 0.61$) than the resistive drift waves in the low-beta kinetic regime, however, the Landau resonance frequency increases to $\hat{\omega}(\hat{\gamma}_{\max}) \sim 0.7 - 0.8$ as the plasma pressure increases. (see Fig. 3.3(b) and (c)).

One may use electrostatic models for analyses of edge-SOL plasma turbulences in conventional tokamaks. In the small or mid size magnetic confinement devices the plasma temperature and density in the edge region are found to be $T_e \sim 10 - 100$ eV and $n_e \sim 10^{12}$ to 10^{13} cm $^{-3}$, respectively

[68, 69, 70, 71, 72, 73, 74]. This parameter range is somewhat marginal between the collisional and the collisionless regime in $\tilde{\beta}_e \ll 1$ (see Fig. 3.2). Therefore, the model of electrostatic drift-kinetic electron with collision operator can describe the regime correctly [39].

However, the electrostatic approximation would not be applicable when the plasma temperature and density are significantly high so that the normalized plasma beta is larger than unity. For the ELM filaments or pedestal region of conventional tokamaks,[75] the electron temperature and density can be $T_e \sim 1 \text{ keV}$ and $n_e \sim 5 \times 10^{13} \text{ cm}^{-3}$. We notice that only kinetic electron models with electromagnetic correction (Fig. 3.2 (b) and (c)) can describe properly the drift wave instability in the regime of $\tilde{\beta}_e \gtrsim 1$ and $\hat{v} < 1$.

For example, electromagnetic fluid model predicts convective coherent structures (ELM filaments) to have small growth rate, $\hat{\gamma}_{\max} \sim 0.02$, in the high-beta regime so that the time scale of radial propagation is similar to the time scale of the drift wave instability growth, $\gamma\tau_{\perp} \sim 1$, where $\tau_{\perp} = L/V_{\perp}$ is radial convection time for the radial distance $L \sim 10\delta$ with radial velocity $V_{\perp} \sim 0.1c_s$. This means that, from the electromagnetic fluid model, the filamentary structure may maintain its coherency during the radial propagation into the plasma facing components. In practice, however, the Landau resonance effects increase the growth rate by about 10 times, $\hat{\gamma}_{\max} \sim 0.2$ in $\tilde{\beta}_e \gtrsim 1$ regime, causing the density bump of structure is dissipated by micro instabilities during radial propagation of the filamentary structure.

3.4 Finite ion temperature and stabilization of drift wave instability

In previous section we considered the case of negligible ion temperature, $T_i/T_e \sim 0$, to separate the electron dynamics from the ion dynamics. However, in edge region of confinement

devices the ratio of ion to electron temperature can be comparable or higher than unity [18]. We may use the same dispersion equations, Eqs. (3.33), (3.34) and (3.35) to include the finite ion temperature effects because the effects have been implemented in the general Vlasov equation for ion distribution function in the form of $2\chi T_i/T_e$, \hat{I}_0 and $\hat{\xi}$.

Figure 3.4 shows the maximum growth rates for different values of T_i/T_e for each electromagnetic models. For electrostatic regime where the normalized plasma beta is less than 1, the finite ion temperature has an effect of decreasing growth rates of drift wave instabilities. The reduction of maximum growth rate as a function of T_i/T_e is not significantly large for $T_i/T_e \lesssim 1$. However, the maximum growth rates decrease by a factor of two for $T_i/T_e = 10$. This stabilization effect of finite ion temperature also can be found in Refs. [76, 39].

The finite ion temperature effects on the stabilization of drift wave instability become dramatically strong as the plasma density and temperature are increased to high-beta and low collisionality regime. Examining the maximum growth rates near parameter regimes of pedestal or ELM filaments, $T_e \sim 1 \text{ keV}$ and $n_e \sim 5 \times 10^{13} \text{ cm}^{-3}$, Figs. 3.4 (c), (f) and (i) show $\hat{\gamma}_{\max}(T_i/T_e = 0.1) \simeq 0.19$, $\hat{\gamma}_{\max}(T_i/T_e = 1.0) \simeq 0.17$ and $\hat{\gamma}_{\max}(T_i/T_e = 10) \simeq 0.009$, respectively. This strong reduction (about factor of 20) of drift wave instability for $T_i/T_e = 10$ in the collisionless high beta regime is due to synergistic effects of finite ion temperature, electromagnetic suppression and collisionless Landau damping. We note that similar electromagnetic stabilization of tokamak ion temperature gradient (ITG) modes in a high-beta regime was also studied in Ref. [77].

Although the electromagnetic fluid model appears to be showing some finite growth rate in weak collisional regime (Fig. 3.4 (a) and (d)), it should be recognized that the fluid equation cannot describe plasma turbulences properly in the collisionless high-beta regime. The electromagnetic fluid model with $T_i/T_e \simeq 1$ seems to show finite growth rates in the region of $\hat{v} > 1$ and $\tilde{\beta}_e > 1$. For example, the growth rate from the fluid model at $T_e \sim 1 \text{ keV}$ and $n_e \sim 5 \times 10^{13} \text{ cm}^{-3}$ for $T_i/T_e = 1$

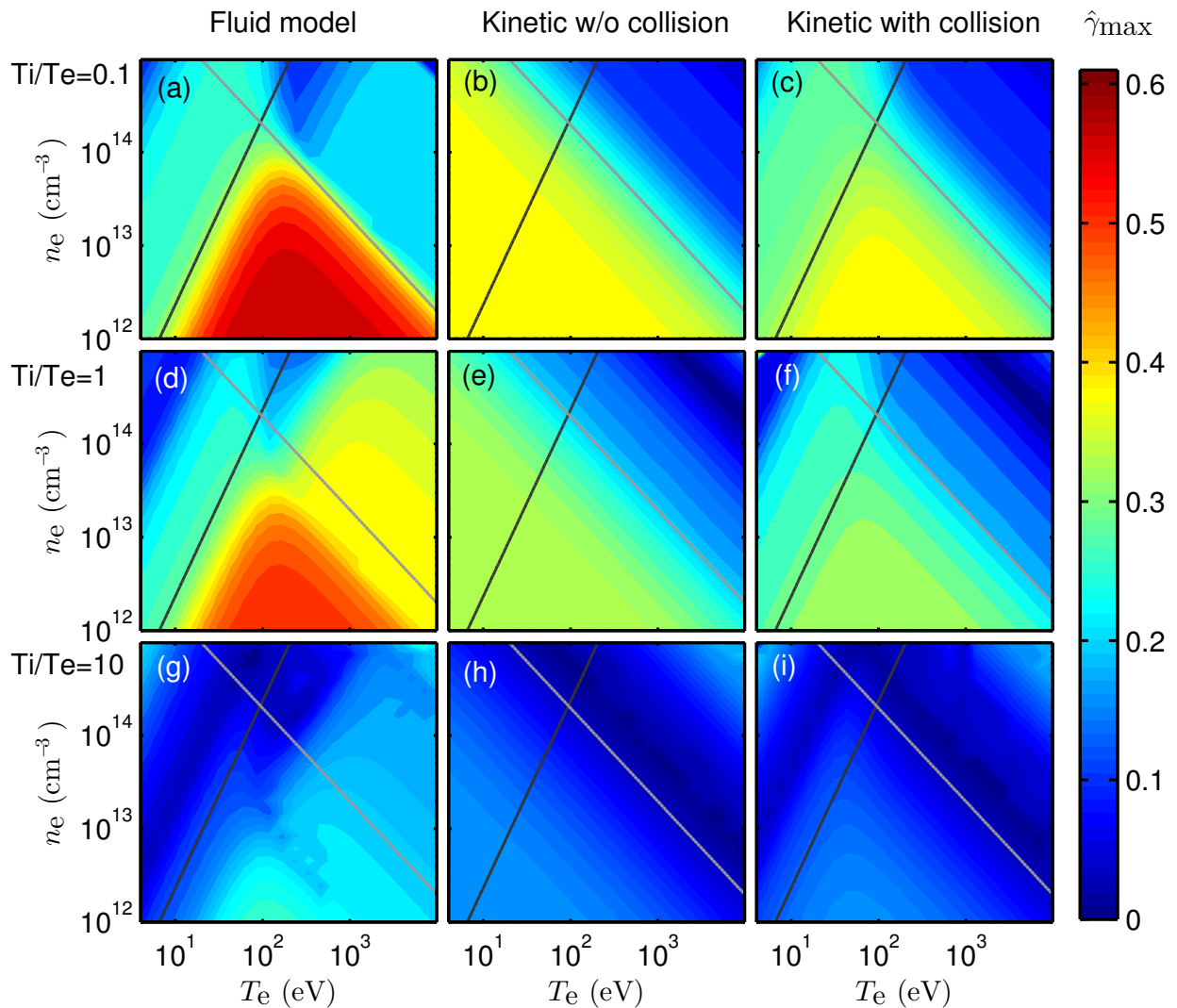


Figure 3.4: Contour plots of normalized maximum growth rates, $\hat{\gamma}_{\max}$, for electromagnetic (EM) models. The first, second and third row of subplots are obtained for $T_i/T_e = 0.1$, $T_i/T_e = 1.0$ and $T_i/T_e = 10.0$, respectively. The black and gray line represent the contours for $\hat{v} = 1$ and $\tilde{\beta}_e = 1$, respectively.

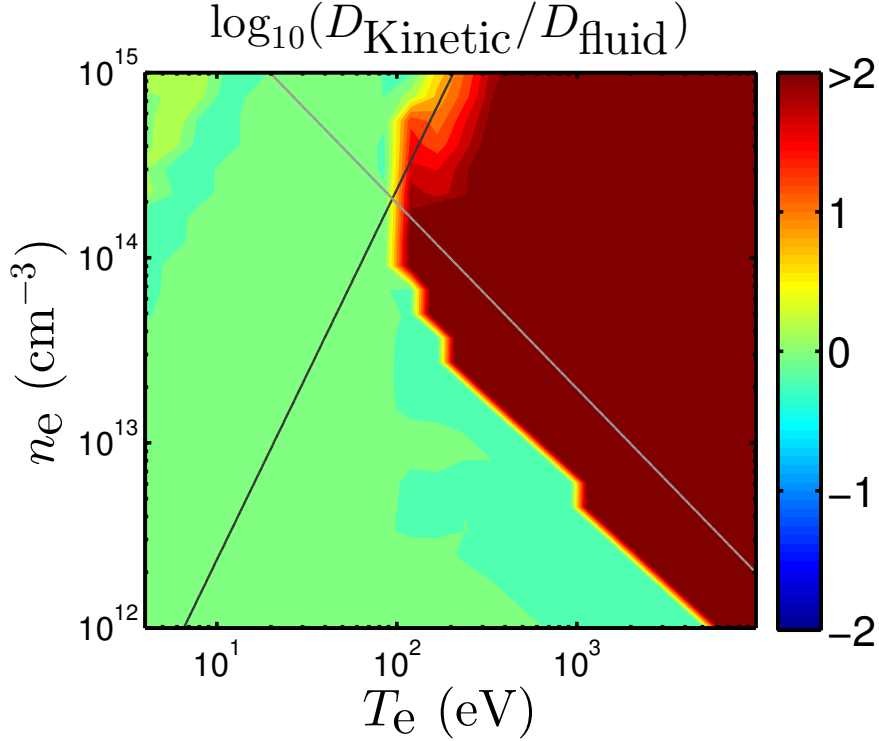


Figure 3.5: The ratio of estimated turbulent diffusivity of EM kinetic model to that of EM fluid mode for $T_i/T_e = 1$. The turbulent diffusivity is estimated by $D \simeq \gamma_{\max}/k_{\perp}^2$.

(Fig. 3.4(d)) is about twice higher than that from the kinetic models (Fig. 3.4(e) and (f)). However, the wave number of the most unstable mode from the fluid model is found to be much higher than the kinetic models. As a result, a turbulent diffusivity from a rough estimation, $D \simeq \gamma_{\max}/k_{\perp}^2$, shows significant difference between the fluid and kinetic models in collisionless high-beta regime (see Fig. 3.5). In this context, the extension of applicability of fluid models with kinetic closures (e.g. Landau-fluid operators[78]) is suggested for future study (See Appendix B).

3.5 Conclusion

Characteristics of electromagnetic parallel electron dynamics and finite ion temperature effects on density gradient driven drift wave instability were studied for wide range of plasma

parameters. Governing equations based on electromagnetic drift-kinetic equation with BGK-like collision operator and general Vlasov-Maxwell equation were used to describe the parallel electron dynamics and the ion dynamics respectively. Using local linear analysis, we demonstrated that the general dispersion relation derived from the kinetic equations shows consistency with two extreme models (fluid and collisionless kinetic models) in collision limiting cases and also with electrostatic models in low beta regime. We also showed that wave-particle resonance effects exhibit smoothed growth rates in weak collisional regime across the marginal plasma beta regime by damping high frequency electron inertia mode observed in EM fluid model in low-beta plasmas and by exciting drift waves in high-beta plasmas.

The stability characteristics of density gradient driven drift waves are modified by finite ion temperature effects. It was shown that the linear growth rate reduces slightly as ion temperature increases to $T_i/T_e \lesssim 1$. The growth rates is reduced by a factor of 20 as the ion temperature is an order of magnitude larger than the electron temperature. Moreover, the stabilization of drift waves from finite ion temperature effects becomes even stronger (order of magnitude) in finite beta regime due to synergistic effects of electromagnetic suppression and collisionless Landau damping.

The work presented in this chapter is a reprint of the material as it appears in *Electromagnetic drift waves dispersion for arbitrarily collisional plasmas* in Physics of Plasmas 22, 072113 by Wonjae Lee, J. R. Angus, and Sergei I. Krasheninnikov, 2015. The dissertation author was the primary investigator and author of this paper.

Chapter 4

Verification of 5D continuum gyrokinetic code COGENT: studies of kinetic drift wave instability

COGENT (Continuum Gyrokinetic Edge New Technology) is a kinetic plasma simulation code which is being developed by the edge simulation laboratory (ESL) collaboration. The original version of the code has been developed in 4D phase space (2D configuration space and 2D velocity space) to address kinetic plasma phenomena in complex magnetic field geometry including core, magnetic separatrix and scrape off layer region. This work is focused on extending the original 4D phase space to 5D phase space (3D2V) to address full kinetic turbulences in Tokamak edge region. Here, we report the current status of 5D COGENT employed for shear-less simple slab geometry. As a verification study, we use the problems of collisionless drift wave instability (universal instability) and collisional drift wave instability. The electrostatic gyrokinetic equations for two kinetic species (ions and electrons) are solved self-consistently and coupled to the long-wavelength limit of the Poisson equation. Simulation results show that the growth rate and the real frequency of the drift wave

correspond to the theoretical solution of the drift wave instability corresponding to the resonance wave-particle interaction in the magnetized inhomogeneous plasmas. Using the Krook collision operator in COGENT, we also found that the transition of the collisionless drift wave instability to the collisional drift wave instability shows good agreement with theoretical results for weakly collisional plasmas. Extensive 5D runs have been performed to address the effects of the drift-wave instability on blob/filamentary structures characteristic of a tokamak edge. A helical-shape potential perturbation is observed to grow exponentially in time while spinning around the filament axis with electron drift frequency. The nonlinear stage of the drift-wave instability is observed and analyzed as well.

4.1 Introduction

The boundary region of a tokamak encompasses plasma existing between a high-pressure core region and plasma facing materials. Plasma transport in the boundary region is dominated by instabilities driven by large gradients of the density or temperature. The collisional mean free path in the plasma boundary region can exceed the wave length of micro instabilities (e.g. drift wave instabilities), and as a result the plasma species distribution function may deviate from a Maxwellian distribution during instability phenomena. Therefore, a hydrodynamic approach which assumes a Maxwellian distribution function and is often used to describe axisymmetric edge plasma transport might not be valid for the edge plasma turbulence. In order to describe weakly collisional boundary plasmas, we consider a gyrokinetic model employed in the Eulerian (continuum) finite-volume code, COGENT [79, 80, 81, 82]. The code has been successfully used to model 4D axisymmetric plasma dynamics including pilot studies of the collisionless drift-wave instability with a fixed ratio of the parallel and perpendicular wave-numbers [?]. Here, we present initial results from the 5D version of the code, which has recently become operational in a shear-less slab geometry. Our studies include

verification of electrostatic simulations of the drift-wave instability for various collisionality regimes for the case of a uniform background magnetic field and temperature. In addition, development of the drift-wave instability on top of filamentary/blob structures is analyzed

In the absence of the magnetic field and temperature gradients the driving mechanisms for the drift wave instability is dissipation, which provides the phase shift between the density and potential perturbations and depends on the collisionality regime of the plasma. If collisions are negligible, the dissipation is provided by the Landau damping, in which case the instability is sometimes called universal. In the opposite limit of strong collisions, the instability is called resistive drift wave instability. An analytical analysis of the electrostatic drift wave instability including the effects of Krook collisions can be found in [39].

The present paper is organized as follows. The governing equations used by the COGENT code are summarized in Section 2. The drift simulation model used for initial verification studies is introduced in Section 3. Finally, the simulation results are presented in Section 4.

4.2 Development of 3D2V Gyrokinetic continuum code

4.2.1 Gyrokinetic equation set

The COGENT code uses full-f gyrokinetic model in conservative form [83]:

$$\frac{\partial(B_{\parallel\alpha}^* f_\alpha)}{\partial t} + \nabla_{\mathbf{R}} \cdot (\dot{\mathbf{R}}_\alpha B_{\parallel\alpha}^* f_\alpha) + \frac{\partial}{\partial v_{\parallel\alpha}}(\dot{v}_{\parallel\alpha} B_{\parallel\alpha}^* f_\alpha) = B_{\parallel\alpha}^* C_\alpha [f_\alpha], \quad (4.1)$$

where

$$\dot{\mathbf{R}}_\alpha = \dot{\mathbf{R}}_\alpha(\mathbf{R}, v_{\parallel\alpha}, \mu, t) = \frac{v_{\parallel\alpha}}{B_{\parallel\alpha}^*} \mathbf{B}_\alpha^* + \frac{1}{Z_\alpha e B_{\parallel\alpha}^*} \mathbf{b} \times \mathbf{G}_\alpha, \quad (4.2)$$

$$\dot{v}_{\parallel\alpha} = \dot{v}_{\parallel\alpha}(\mathbf{R}, v_{\parallel\alpha}, \mu, t) = -\frac{1}{m_\alpha B_{\parallel\alpha}^*} \mathbf{B}_\alpha^* \cdot \mathbf{G}_\alpha, \quad (4.3)$$

and

$$\mathbf{B}_\alpha^* = \mathbf{B}_\alpha^*(\mathbf{R}, v_{\parallel\alpha}) = \mathbf{B} + \frac{m_\alpha v_{\parallel\alpha}}{Z_\alpha e} \nabla_{\mathbf{R}} \times \mathbf{b}, \quad (4.4)$$

$$\mathbf{G}_\alpha = \mathbf{G}_\alpha(\mathbf{R}, v_{\parallel\alpha}, \mu, t) = Z_\alpha e \nabla_{\mathbf{R}} \Phi + \mu \nabla_{\mathbf{R}} B. \quad (4.5)$$

where $f_\alpha = f_\alpha(\mathbf{R}, v_{\parallel\alpha}, \mu, t)$ is the distribution function for the species $\alpha = \{i, e\}$ in the gyrocenter phase space coordinate $(\mathbf{R}, v_{\parallel\alpha}, \mu)$ (see Fig. 4.1). \mathbf{R} is the configuration (physical) space, $v_{\parallel\alpha}$ is parallel velocity space component for species α in the direction of magnetic field and μ is the magnetic moment. The electrostatic potential field Φ is calculated from the long-wavelength limit of the gyro-Poisson equation:

$$\nabla \cdot \left\{ \left[\epsilon_0 \mathbf{I} + e^2 \sum_i \frac{Z_i \bar{n}_i}{m_i \omega_{ci}^2} (\mathbf{I} - \mathbf{b} \mathbf{b}^T) \right] \nabla \Phi \right\} = e \left(n_e - \sum_i Z_i \bar{n}_i \right), \quad (4.6)$$

where \bar{n} is the ion gyrocenter density ω_{ci} is ion gyro frequency and \mathbf{b} is unit vector in the direction of magnetic field. The present version of 5D COGENT operates in the shearless slab geometry.

4.3 Modeling drift-wave instability: simulation set-up

The 5D version of the COGENT code is verified with simulations of drift-wave instability for the case of a uniform magnetic field and temperature background. The background electron

3D configuration mesh

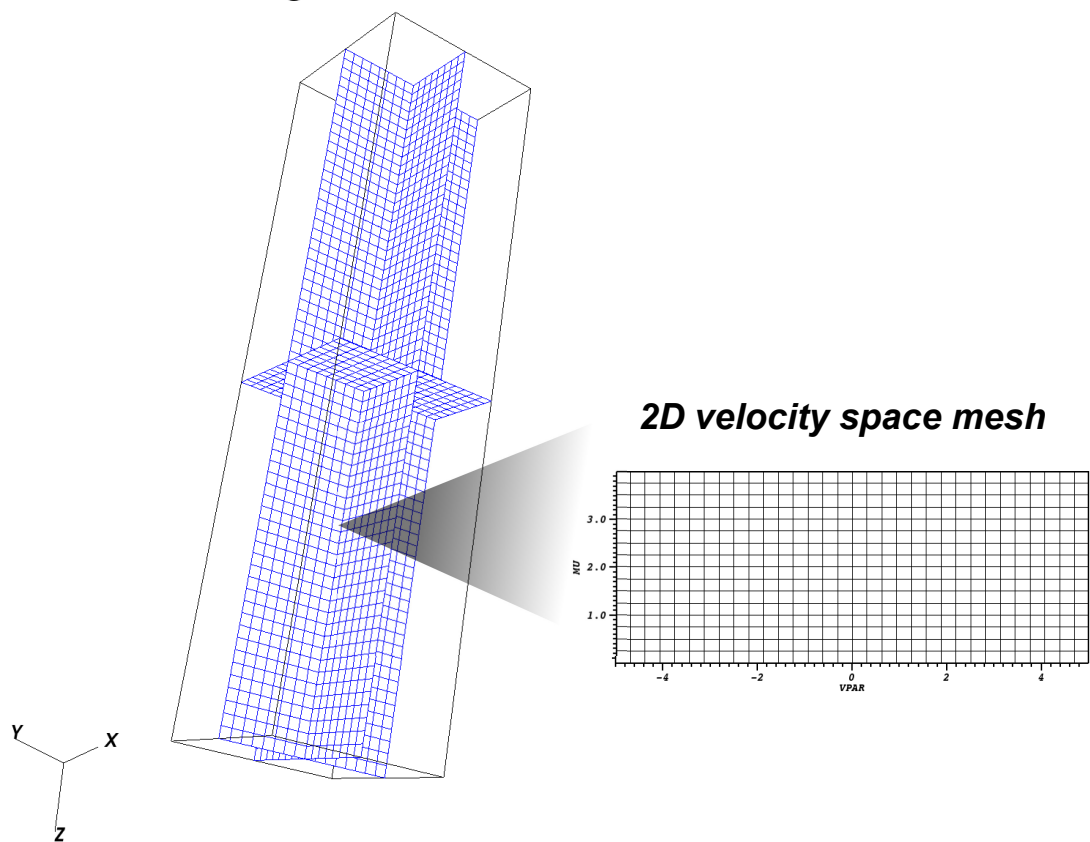


Figure 4.1: Illustration of 5D phase space mesh.

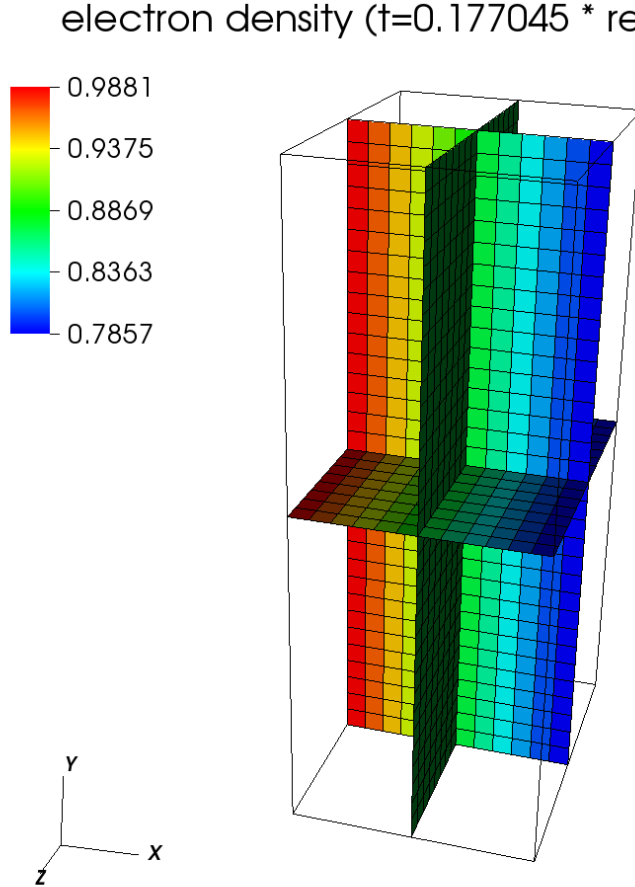


Figure 4.2: Implementation of a 5D phase space in COGENT. (a) Electron density distribution in the 3D configuration space. The electron density are normalized to $n_0 = 10^{20} \text{ m}^{-3}$. Normalization number (ref_t) for the time variable is $5.11 \times 10^{-6} \text{ s}$.

and ion densities decrease exponentially in the x-direction with gradient scaling length (L_n) in a three-dimensional slab geometry where the magnetic field ($B = 1 \text{ T}$) aligned along the z-direction (Fig.4.2). The three-dimensional Cartesian computational grid used here has $12 \times 32 \times 16$ cells. The length of physical domain in the x and y direction is 0.8 cm and the length in the z direction varies from 1.7 to 20 m depending on the simulation case. The electron and ion initial distribution functions are specified by Maxwellian distributions with uniform temperature ($T_i=T_e=400 \text{ eV}$) and zero mean velocity. The two-dimensional velocity space consisting of the parallel velocity and the magnetic moment coordinates is divided into 64×48 computation cells, where the computational parallel velocity coordinate $v_{\parallel\alpha}$ is normalized to $\sqrt{T_\alpha/m_\alpha}$ (see appendix C). Here, $\alpha=e,i$ denotes the

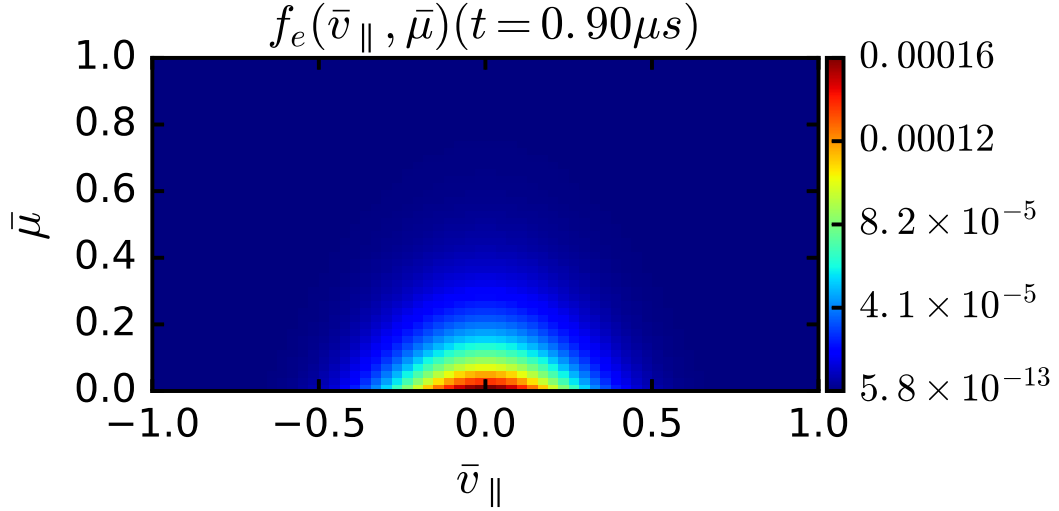


Figure 4.3: Implementation of a 5D phase space in COGENT. Electron distribution function in the 2D velocity space.

electron (e) and ion (i) species (Fig.4.3).

The initial density profiles of electrons and ions include a small perturbation corresponding to the first harmonic in the periodic (y and z) directions. The small density perturbation has a form of $\sin[m_y y/(2\pi) + m_z z/(2\pi)] \sin(0.5x/(2\pi))$ where $x, y, z = [0, 2\pi]$ and $m_y = m_z = 1$ for both electron and ion species (Fig. 4.4).

In order to reduce the boundary effect in the x direction, the initial perturbation is assumed to be negligible at the x-boundaries (Fig.4.5). The boundary conditions in the y and z direction is taken periodic for the species distribution function and electrostatic potential perturbations. The boundary conditions in the x-direction correspond to the zero Dirichlet boundary condition for the potential, and to the inflow-outflow boundary condition for the species, with $f_\alpha(x_{BC}, y, z, v_{||}, \mu, t) =$

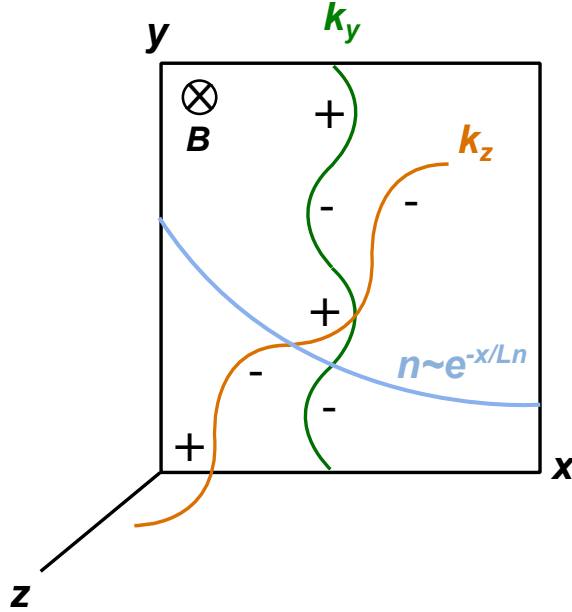


Figure 4.4: Example of initial density perturbation with second harmonics in y and z direction. The first harmonic perturbations are used in the simulation. The amplitude of perturbation is exaggerated for visualization.

$$f_\alpha(x_{BC}, y, z, v_{||}, \mu, t = 0).$$

The time integration algorithm utilizes the fourth-order explicit Runge-Kutta (RK4) method, restricted by the Courant constraint. To speed-up the simulations, we consider an artificial ion-to-electron mass ratio of 200. The calculated distribution functions of electrons and ions are integrated in the velocity space to form charge density in each cells of configuration space. The three-dimensional Poisson solver then calculates the electrostatic potential distribution using this charge distribution. The electrostatic potential is used to calculate the electric field for the next time step.

Here, we consider a simple Krook collision model for electrons, $C_e[f_e] = -v_e(f_e - f_{e0})$, where f_{e0} is initial electron distribution, v_e denotes the collision frequency which is assumed to be spatially constant, for simplicity purposes. Ion collisions are not included. Performing a straightforward linear analysis of Eqs. (4.1)-(4.6) (see Appendix D) we obtain the following drift-wave dispersion relation for the case of a uniform background magnetic field and temperature.

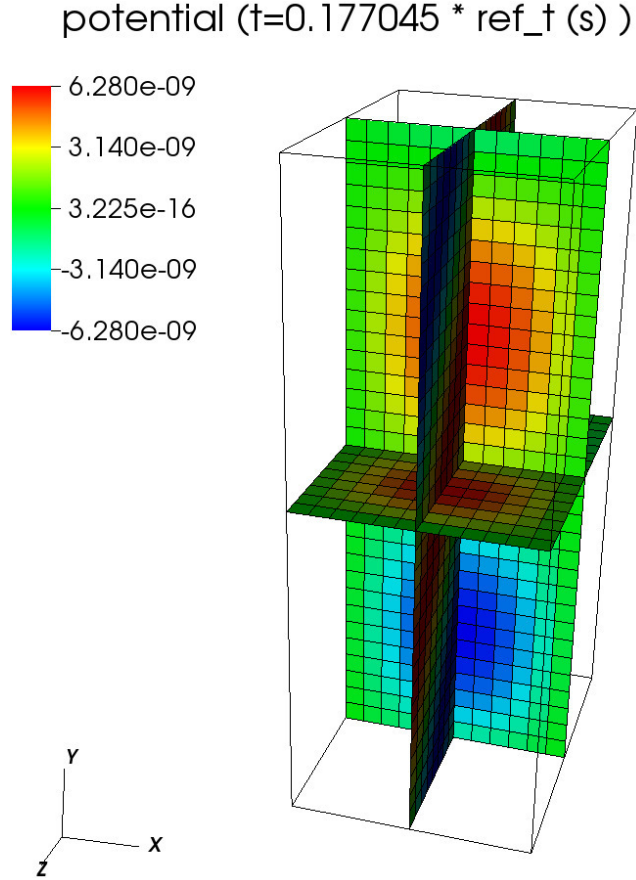


Figure 4.5: 3D electrostatic potential distribution normalized to $\phi_0 = 400\text{V}$. The normalization number (ref_t) for the time variable is $5.11 \times 10^{-6} \text{ s}$.

$$\begin{aligned}
 & \frac{T_i}{m_i} \frac{1}{\omega_{ci}^2} \left[-ik_x \frac{1}{L_n} - \left(\frac{\omega_{ci}^2}{\omega_{pi}^2} + 1 \right) k_x^2 - \left(\frac{\omega_{ci}^2}{\omega_{pi}^2} + b_z^2 \right) k_y^2 - \frac{\omega_{ci}^2}{\omega_{pi}^2} k_z^2 \right] \\
 &= 1 + \left[\frac{\hat{\omega}}{\hat{k}_z} + \frac{T_i}{T_e} \frac{\hat{k}_y}{\hat{k}_z} \right] \sqrt{\frac{m_i T_e}{m_e T_i}} Z \left(\frac{\hat{\omega}}{\hat{k}_z} \sqrt{\frac{m_i T_e}{m_e T_i}} \right) + \frac{T_i}{T_e} + \left[\frac{T_i}{T_e} \frac{\hat{\omega} + i\hat{v}_e}{\hat{k}_z} - \frac{T_i}{T_e} \frac{\hat{k}_y}{\hat{k}_z} \right] Z \left(\frac{\hat{\omega} + i\hat{v}_e}{\hat{k}_z} \right), \quad (4.7)
 \end{aligned}$$

where Z is plasma dispersion function, $\hat{\omega} = \omega L_n / c_s$, $\hat{v}_e = v_e L_n / c_s$, $\hat{k}_y = k_y \rho_s$, $\hat{k}_z = k_z (L_n v_{th,e}) / c_s$ and $\rho_s = c_s / \omega_{ci}$, and we assumed $k_x L_n \gg 1$. We solve this dispersion relation numerically to find the maximum growth rate and corresponding real frequency for the parameters of COGENT simulations.

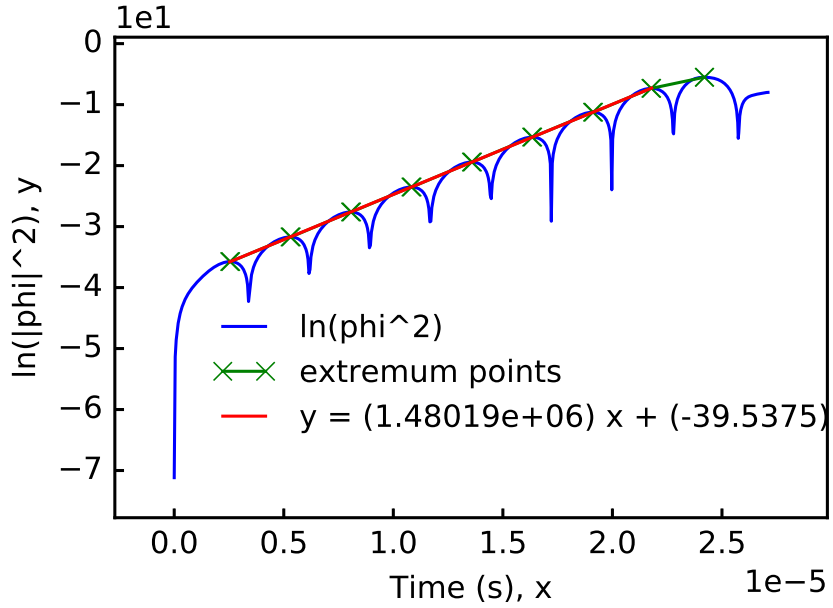


Figure 4.6: Evaluation of the linear growth rate (red line) from the potential perturbation history (blue curve) obtained in the COGENT simulations of the drift wave instability.

4.4 Result of numerical simulations

The verification of COGENT code was performed by comparing the growth rate and corresponding real frequency of the drift wave instability extracted from the simulation results with the approximate theoretical predictions for the maximum growth rate and corresponding real frequency from the wave dispersion relation (Eq.4.7). In order to obtain the linear drift-mode growth rate and frequency from the COGENT simulations, a post-processing of a potential perturbation time history is performed as shown in Fig. 4.6. Figures 4.7 and 4.8 illustrate excellent agreement with the approximate analytical results for the collisionless case and the case with the electron Krook collision model (see Sec. 3), respectively.

We note that collisionless drift-wave is driven unstable by the wave-particle interaction mechanism. Figures 4.9(a) and (b) show the deviation of the electron distribution function from the Maxwellian distribution. The kinetic particles with velocities near the drift wave phase speed

experience the Landau resonances. The width (Δv) of the perturbation of distribution function is consistent with strength of the instability, $\gamma \sim k_{\parallel} \Delta v$.

We also investigate the development of the collisionless drift wave instability on an isolated plasma filamentary structure extended along the magnetic field lines (Fig.4.10). The particle density is set to $1 \times 10^{19} \text{ m}^{-3}$, the species temperature is $T_i = T_e = 400 \text{ eV}$, and the magnetic field strength is $B = 1.5 \text{ T}$. The domain size along the magnetic field direction (z) is 1.6 m and the domain extent in the perpendicular directions (x, y) is 4 cm. The computation domain resolution is given by $(N_x, N_y, N_z, N_{v_{\parallel}}, N_{\mu}) \leftrightarrow 64 \times 64 \times 32 \times 36 \times 12$.

Exponential growth of helically-shaped potential perturbations is observed inside the filament. The perturbations spin around the filament axis with the electron drift frequency. For these simulations a random-noise perturbation [Figure 4.11(a)] is introduced to the filament equilibrium background and ($m_{\theta} = 2$) mode is observed to be dominant at early stages of the simulations. However, later in time, a higher-order unstable mode ($m_{\theta} = 3$) takes over [Fig. 4.11 (b)] and its nonlinear saturation is shown in Figure 4.10 (d).

4.5 Conclusion

We extended the capability of the COGENT code by extending the previous two dimensional configuration space to three dimensions. In order to verify the feasibility of the extended code, a simple 3D slab geometry was used to implement collisionless drift wave instability and collisional drift wave instability. The frequency and growth rate of the drift wave obtained from the simulation are consistent with solutions of dispersion relation derived from the Gyrokinetic Vlasov-Poisson model. The COGENT code shows that the distribution function deviation away from the Maxwellian distribution as a result of the wave-particle interactionss. This distribution fluctuation was shown to be correlated to the growth rate of collisionless drift wave instability. We also show that the Krook

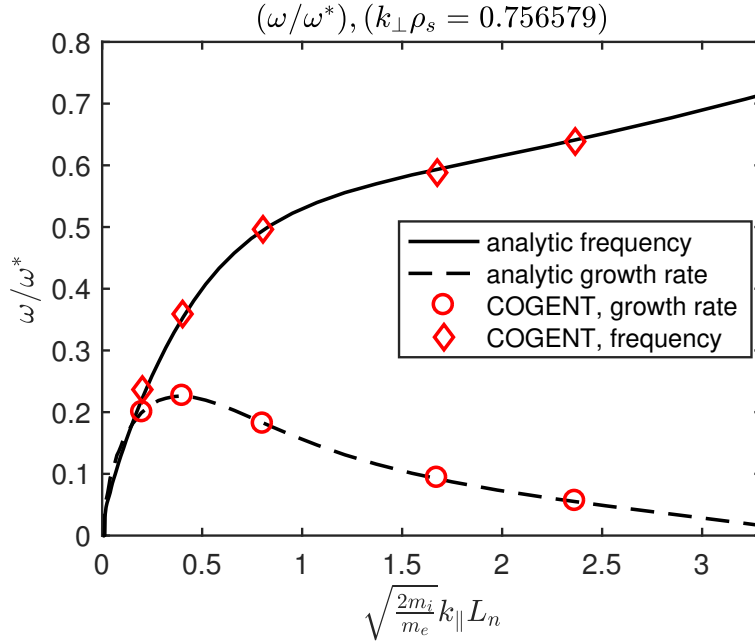


Figure 4.7: COGENT simulations results compared to the analytical predictions in Eq. (4.7) without collisions.

collision operator, which is one of the many collision operators included in the COGENT code, gives the result that the theoretical value and the simulation value. It suggests that the physics problem of the weakly collisional plasma can be solved by using the COGENT collision operator. As an example of application of this code, we investigated the collisionless drift wave instability in the blob-filamentary plasma structure in the boundary region. The filamentary plasma structure develops helical shape of potential perturbation due to the collisionless drift wave instability.

The work presented in this chapter is a reprint of the material as it appears in *Verification of 5D continuum gyrokinetic code COGENT: studies of kinetic drift wave instability* submitted in Contribution to Plasma Physics, 2017, by Wonjae Lee, M.A. Dorf, M.R. Dorr, R.H. Cohen, T.D. Rognlien, J.A. Hittinger, M.V. Umansky, and S.I. Krasheninnikov. The dissertation author was the primary investigator and author of this paper.

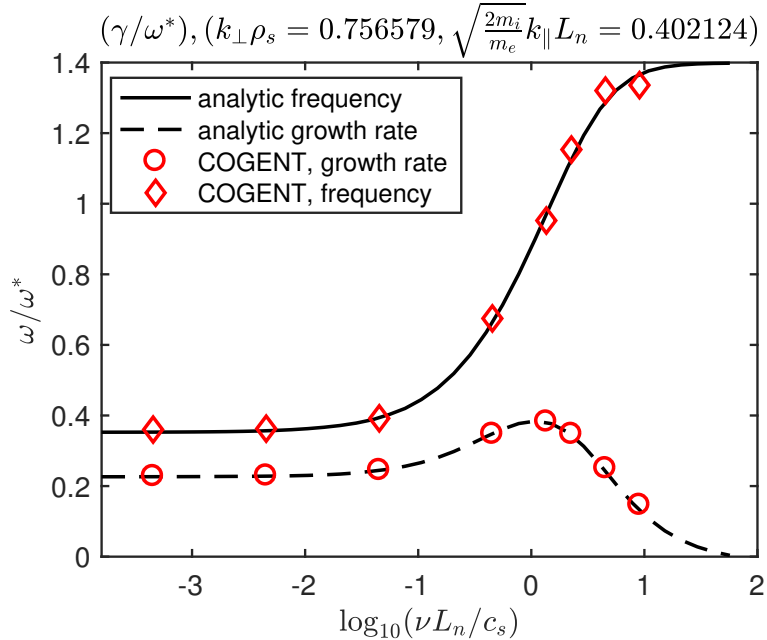


Figure 4.8: COGENT simulations results compared to the analytical predictions in Eq. (4.7): includes the effects of electron collisions described by the Krook model.

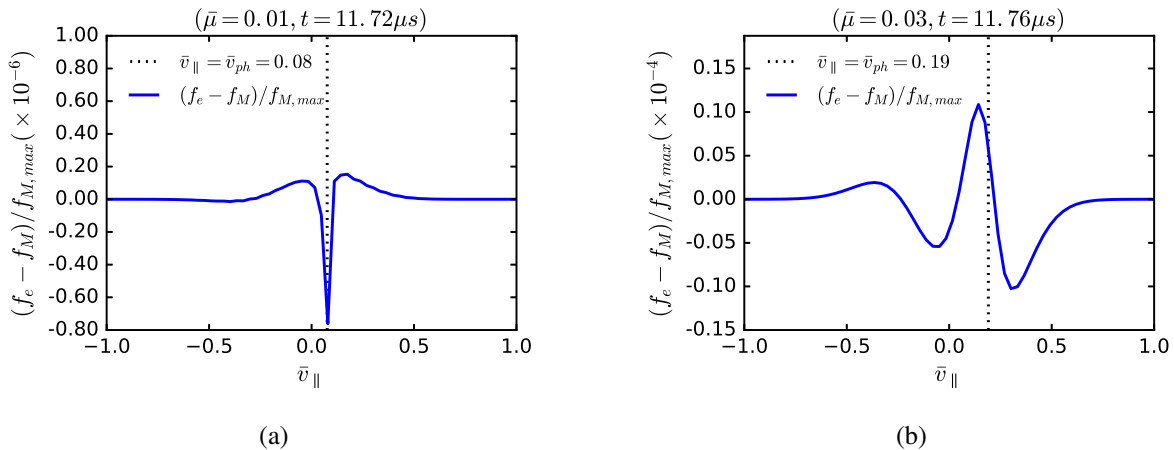


Figure 4.9: Pronounced deviations of the electron distribution function from the Maxwellian background are observed for the collisionless case near the drift-wave phase velocity due to wave-particle resonance. The normalized drift-wave phase velocity (v_{ph}) is illustrated by the dotted line. The results of the simulations in Frames (a) and (b) correspond to low ($\gamma/\omega^* = 0.1$) and high ($\gamma/\omega^* = 0.23$) values of the growth rate, respectively. \bar{v}_{\parallel} and $\bar{\mu}$ are the normalized parallel velocity and normalized magnetic moment, respectively.

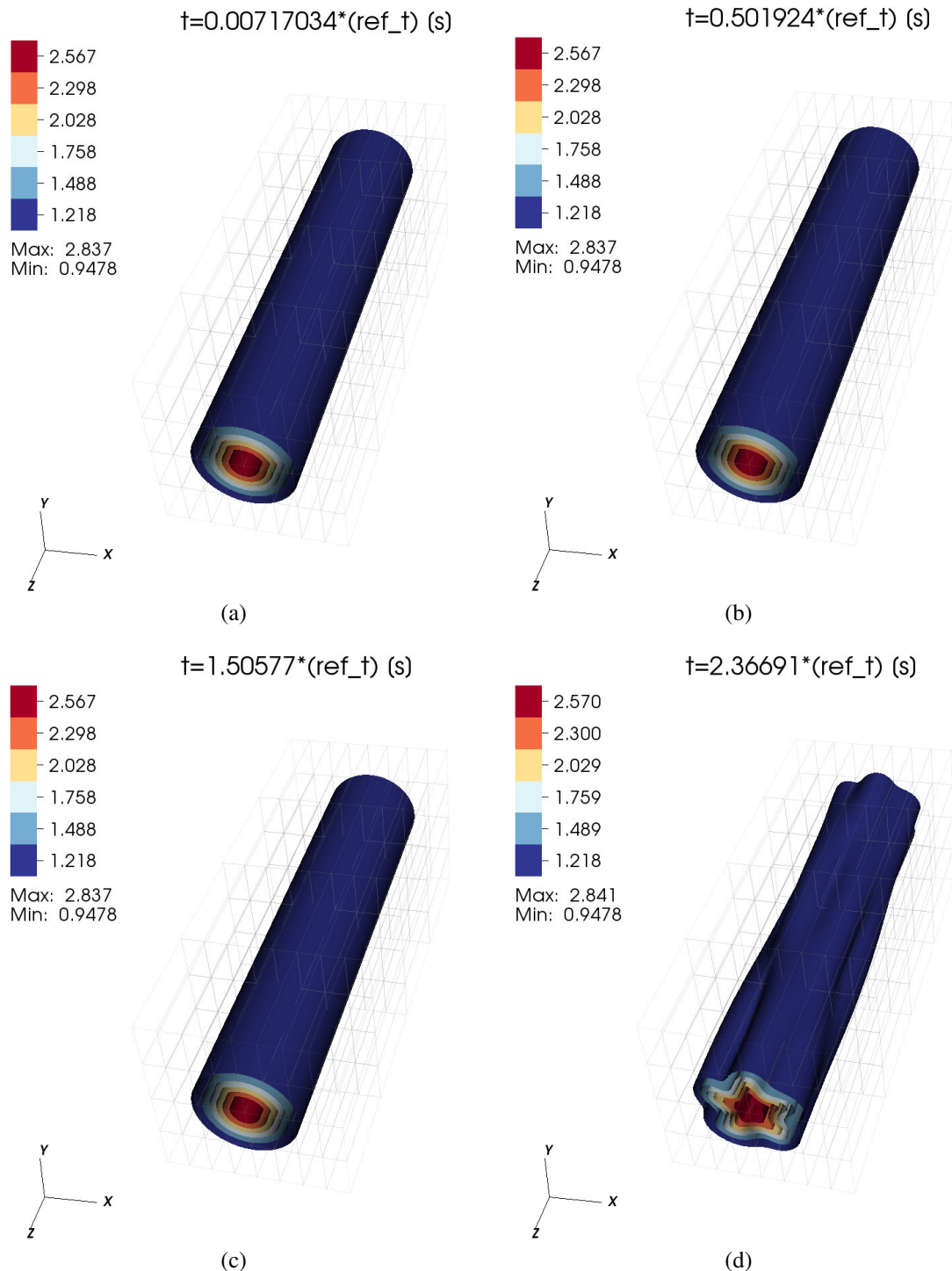


Figure 4.10: Development of the collisionless drift wave instability on a blob-filamentary plasma structure extended along the magnetic field lines. Plotted is the normalized plasma density iso surfaces. The time variable is normalized to the reference time ($\text{ref_t} = 5.11 \times 10^{-6}$ s). The filament structure is shown not to scale for the visualization purposes.

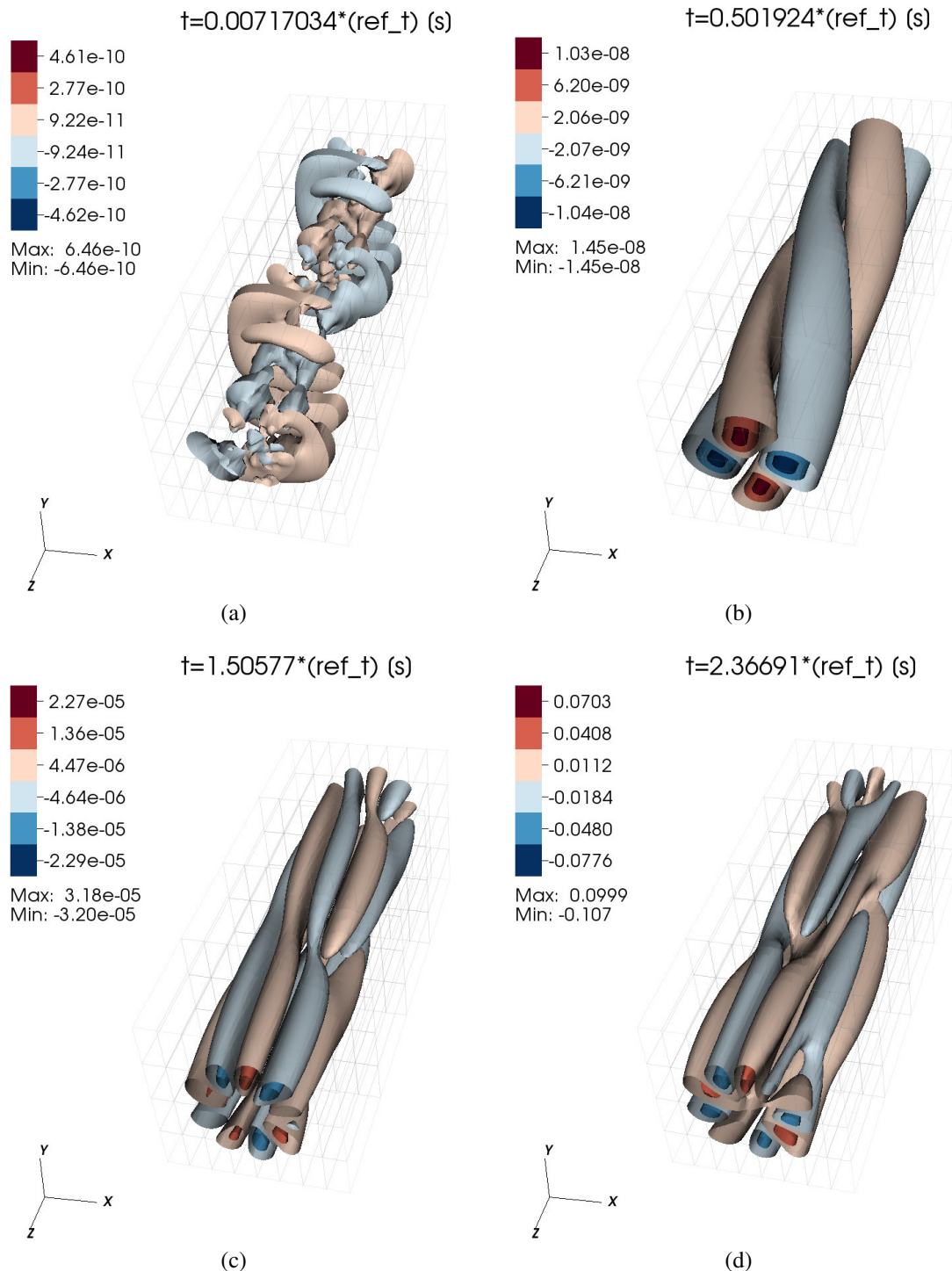


Figure 4.11: Development of helical electrostatic potential perturbations inside the blob-filamentary structure. The helical perturbations rotate around the blob axis with the electron drift speed. The time variable is normalized to the reference time ($\text{ref_t}=5.11 \times 10^{-6}$ s). The filament structure is shown not to scale for the visualization purposes.

Chapter 5

Summary

The main objective of this thesis is to understand the characteristics of a blob filament as an entity of plasma anomalous transport phenomena in the boundary region of a magnetic confinement machine. This was conducted through analytical work and numerical solution methods. More specifically, the influence of the electromagnetic effect, which is important in high-beta plasma, on the macroscopic transport properties and microscopic stability of blob filaments was studied, along with the drift wave instability of general plasmas satisfying weakly collisional conditions with high beta values. Full-f kinetic simulations were performed for weakly collisional drift waves using the Eulerian finite volume code COGENT.

A plasma blob filament is a coherent turbulent structure that is mainly found in the SOL of magnetic confinement devices and transports plasma particles and heat through the radial convective motion. In the conventional 3D electrostatic model, blob filaments were predicted to be dissipated with a shorter time scale than the advection time scale due to RDWI in plasma filaments.

The electromagnetic fluid model shows that both macroscopic advection characteristics of plasma filaments and microscopic stability are associated with drift wave instability variations. A reduced form of the Braginskii equation for electromagnetic high-beta plasma filaments consisting

of the vorticity, density, and parallel component of the vector potential equation was considered. Because of the time scale of the newly introduced Alfvén wave from the electromagnetic model, the cross-SOL advection time scale of a blob becomes shorter than the time for the polarization potential inside the blob propagating along the filament in the high-beta plasma. As a result, unlike conventional low-beta filaments, the influence of the plasma sheath connection is reduced in the case of the high-beta filaments. Moreover, it was demonstrated that an inhomogeneous magnetic curvature leads to the macroscopic bending of high-beta filaments. Through linear analysis and BOUT ++ simulation, the thesis also showed that the electromagnetic effects in the high-beta regime reduce the growth rate of RDWI when the plasma resistivity drops below a certain value. The results suggest that the high-beta filaments can enhance heat exchange between plasma facing materials and the inner region of edge plasma forming a parallel heat conduction channel with reduced dissipation.

However, in order to describe stability of SOL plasma filaments expected in future tokamaks, a general form of a model satisfying both kinetic and electromagnetic effects is required for describing the weakly collisional high-beta plasma. We considered a system consisting of the electromagnetic drift-kinetic equation containing a simple BGK-like collision operator for electrons and the general Vlasov-Maxwell equation for ions. The generalized dispersion relations obtained by the local linear analysis show that the newly developed electromagnetic kinetic model approaches the fluid model and the collisionless kinetic model, respectively, in the high- and low-collision limiting cases, and the characteristics corresponding to the electrostatic model result in the low-beta regime. In the electromagnetic fluid model, high-beta plasma showed a negligible growth rate owing to the electromagnetic effect when the collision frequency was small. However, it is shown that considering the kinetic effect, collisionless drift wave instability due to the Landau resonance effect becomes dominant in the weakly collisional high-beta regime. When the ion temperature is higher than the electron temperature owing to the finite ion temperature effect, the growth rate of the density gradient

driven drift wave decreases to the order of magnitude. In the case of the high-beta plasma, the reduction in the drift wave growth due to the finite ion temperature effect becomes even stronger.

In order to simulate a resistive/collisionless drift wave in the weakly collisional plasma in the tokamak SOL region, the COGENT Eulerian gyrokinetic code was extended from the existing 4D phase space to the 5D phase space. It was shown that the frequency and growth rate of collisionless drift wave simulations performed on a simple 3D slab geometry are consistent with those analytically derived. Particularly, the distribution function observed in the collisionless drift wave simulation is different from the Maxwellian distribution as a result of wave-particle interactions, and the fluctuation of this distribution is related to the growth rate of collisionless drift wave instability. Finally, the simulation demonstrates that the collisionless drift wave instability develops a helical shape of the perturbation structure inside of a plasma filament.

Appendix A

Derivation of Eq. (3.4)

The zeroth, second and first velocity moment of Eq. (3.2) are

$$\begin{aligned} \frac{\tilde{n}_e}{n_0} &= \frac{1}{n_0} \int \tilde{f} d\mathbf{v} \\ &= (1 + (\alpha - \check{\omega}_*)Z(\alpha)) \frac{e\tilde{\phi}}{T_e} - i\check{v}Z(\alpha) \frac{\tilde{n}_e}{n_0} - i\check{v} \left(\alpha + (\alpha^2 - \frac{1}{2})Z(\alpha) \right) \frac{\tilde{T}}{T_e} \\ &\quad - (\check{\omega} - \check{\omega}_*)[1 + \alpha Z(\alpha)] \frac{e\sqrt{2}v_e}{T_e c} \tilde{A}_{\parallel}, \end{aligned} \quad (\text{A.1})$$

$$\begin{aligned} \frac{3}{2} \left[\frac{\tilde{n}_e}{n_0} + \frac{\tilde{T}}{T_e} \right] &= \frac{1}{2v_e^2 n_0} \int v^2 \tilde{f} d\mathbf{v} \\ &= -i\check{v}[\alpha + (1 + \alpha^2)Z(\alpha)] \frac{\tilde{n}_e}{n_0} + \left[\frac{3}{2} + (\alpha - \check{\omega}_*) (\alpha + (1 + \alpha^2)Z(\alpha)) \right] \frac{e\tilde{\phi}}{T_e} \\ &\quad + i\check{v} \left[-\alpha - \alpha^3 - \frac{Z(\alpha)}{2} - \frac{\alpha^2}{2}Z(\alpha) - \alpha^4Z(\alpha) \right] \frac{\tilde{T}}{T_e} \\ &\quad - (\check{\omega} - \check{\omega}_*) \left[1 + \alpha Z(\alpha) + \frac{1}{2} + \alpha^2 + \alpha^3 Z(\alpha) \right] \frac{e\sqrt{2}v_e}{T_e c} \tilde{A}_{\parallel}, \end{aligned} \quad (\text{A.2})$$

$$\begin{aligned}
\frac{\frac{c}{4\pi e} \nabla_{\perp}^2 \tilde{A}_{\parallel}}{\sqrt{2} v_e n_0} &= \frac{1}{\sqrt{2} v_e n_0} \int v_{\parallel} \tilde{f} d\mathbf{v} \\
&= (1 + \alpha Z(\alpha)) \left[(\alpha - \check{\omega}_*) \frac{e \tilde{\Phi}}{T_e} - i \check{v} \frac{\tilde{n}_e}{n_0} + i \check{v} \frac{1}{2} \frac{\tilde{T}}{T_e} \right] - i \check{v} \left(\frac{1}{2} + \alpha^2 + \alpha^3 Z(\alpha) \right) \frac{\tilde{T}}{T_e} \\
&\quad - (\check{\omega} - \check{\omega}_*) (\alpha + \alpha^2 Z(\alpha)) \frac{e \sqrt{2} v_e}{T_e c} \tilde{A}_{\parallel}.
\end{aligned} \tag{A.3}$$

We have used following relation for calculation of the r -th order velocity moments, [84, 85]

$$\begin{aligned}
F_r &= \frac{1}{\sqrt{\pi} v_j} \int_{-\infty}^{\infty} \frac{v_z^r e^{v_z^2/v_j^2}}{\omega + p\omega_c - k_z v_z} dv_z \\
&= \frac{(-v_j)^{r-1} r!}{k_z 2^r} \sum_{k=0}^{r/2} \frac{1}{(r-2k)! k!} \frac{d^{(r-2k)}}{d\alpha_p^{r-2k}} Z(\alpha_p),
\end{aligned} \tag{A.4}$$

where $\alpha_p = (\omega + p\omega_c)/(\sqrt{2}k_z v_j)$.

Combining Eqs. (A.1), (A.2) and (A.3) together, we find

$$\frac{\tilde{n}_e}{n_0} = \frac{g_{1*} g_2 - i \check{v} g_3 g_{4*}}{g_1 g_2 - i \check{v} g_3 g_4} \frac{e \tilde{\Phi}}{T_e}, \quad (\text{EM Kinetic Collisional}), \tag{A.5}$$

where g_n ($n = 1, 2, 3, 4, 1_*, 4_*$) are defined in Eqs. (3.5-3.10).

Appendix B

Dispersion equation for electromagnetic fluid equations with Landau closure

We consider following set of fluid equation for density, momentum and energy conservation:

$$\frac{\partial n_e}{\partial t} + \mathbf{V}_E \cdot \nabla n_e = -\nabla_{\parallel}(n_e V_{\parallel}), \quad (\text{B.1})$$

$$\begin{aligned} m_e n_e \frac{\partial V_{\parallel}}{\partial t} + m_e n_e \mathbf{V}_E \cdot \nabla V_{\parallel} + m_e n_e V_{\parallel} \mathbf{b} \cdot \nabla V_{\parallel} \\ = e n_e \nabla_{\parallel} \phi + \frac{e n_e}{c} \frac{\partial A_{\parallel}}{\partial t} - \nabla_{\parallel} P_e - \alpha_{tm} n_e \nabla_{\parallel} T_e - \frac{\alpha_{fm} m_e n_e}{\tau_e} V_{\parallel}, \end{aligned} \quad (\text{B.2})$$

$$\alpha_0 n_e \frac{\partial T_e}{\partial t} + \alpha_1 n_e T_e \nabla_{\parallel} V_{\parallel} = -\nabla_{\parallel}(\alpha_2 n_e T_e V_{\parallel}) - \nabla_{\parallel} q, \quad (\text{B.3})$$

where $\kappa_{\parallel}^e = 3.16 n_e T_e \tau_e / m_e$. $\alpha_{tm} = 0.71$ is thermal force coefficient and $\alpha_{fm} = 0.51$ is frictional force coefficient in the momentum exchange. We also use following constants for convenience, $\alpha_0 = 3/2$, $\alpha_1 = 1$, $\alpha_2 = 0.71$, $\alpha_3 = 0.51$. The Landau fluid closure is applied in the Eq. (B.3) by

considering corrective heat flux [78, 86, 87],

$$q = -n_0 \chi_1 \frac{\sqrt{2} v_e i k T_k}{|k| + \alpha_3 v_{ei} / v_e}, \quad (\text{B.4})$$

where $\chi_1 = 2/\sqrt{\pi}$ is coefficients defined in Ref. [78]. Linearizing Eqs. (B.1-B.3), we get

$$-i\omega\tilde{n} - \frac{cik_{\perp}}{B}\tilde{\phi}\frac{dn_0}{dx} = -ik_{\parallel}n_0\tilde{V}_{\parallel}, \quad (\text{B.5})$$

$$-i\omega mn\tilde{V}_{\parallel} + vmn\tilde{V}_{\parallel} = enik_z\tilde{\phi} - i\frac{\omega en}{c}\tilde{A}_{\parallel} - ik_z\tilde{n}T - ik_zn\tilde{T} - \frac{ik_y\tilde{A}_{\parallel}}{B}\frac{dn_0}{dx}T_e - \alpha_{tm}nik_z\tilde{T}_e, \quad (\text{B.6})$$

$$-i\omega\alpha_0\tilde{T} + \alpha_1Tik_z\tilde{V}_{\parallel} = -ik_z\alpha_2T\tilde{V}_{\parallel} - k_z^2\frac{\chi\sqrt{2}v_e\tilde{T}_k}{|k| + \alpha_3v/v_e}. \quad (\text{B.7})$$

The linearized equations are used to get a density response equation,

$$\frac{\tilde{n}}{n_0} = \frac{(\omega_* + i\omega_{\parallel}^*)(\alpha_0\omega + i\chi_1\sqrt{2}\omega_{LF}) + i(1 + \alpha_{tm})(\alpha_1 + \alpha_2)\omega_*\omega_{\parallel}^*e\tilde{\phi}}{(\omega + i\omega_{\parallel}^*)(\alpha_0\omega + i\chi_1\sqrt{2}\omega_{LF}) + i(1 + \alpha_{tm})(\alpha_1 + \alpha_2)\omega\omega_{\parallel}^*}\frac{e\tilde{\phi}}{T_e}, \quad (\text{B.8})$$

where

$$\omega_* = \frac{k_y T_e c}{e B \delta}, \quad (\text{B.9})$$

$$\delta = \frac{d \ln n_0}{dx}, \quad (\text{B.10})$$

$$v_* = v - i\omega - i\omega \frac{\omega_{pe}^2}{c^2 k_{\perp}^2} + i\omega_* \frac{\omega_{pe}^2}{c^2 k_{\perp}^2}, \quad (\text{B.11})$$

$$\omega_{\parallel}^* = \frac{k_z^2 T_e}{m_e v_*}, \quad (\text{B.12})$$

$$\omega_{LF} = \frac{k_z^2 v_e}{|k| + \alpha_3 v/v_e}. \quad (\text{B.13})$$

Eq. (B.8) can be compared with a density response function from electromagnetic fluid

equation without Landau closure,

$$\frac{\tilde{n}}{n_0} = \frac{(\omega_* + i\omega_{\parallel}^*)(\frac{3}{2}\omega + i\kappa\omega_{\parallel}) + i\beta\omega_*\omega_{\parallel}^* e\tilde{\phi}}{(\omega + i\omega_{\parallel}^*)(\frac{3}{2}\omega + i\kappa\omega_{\parallel}) + i\beta\omega\omega_{\parallel}^*} \frac{e\tilde{\phi}}{T_e}. \quad (\text{B.14})$$

Comparing the coefficients of Eq. (B.8) with those of Eq. (B.14), we note following correspondence of coefficients:

$$\omega_{LF} \leftrightarrow \omega_{\parallel}, \quad (\text{B.15})$$

$$\chi_1\sqrt{2} \leftrightarrow \kappa = 1.61, \quad (\text{B.16})$$

$$(1 + \alpha_t m)(\alpha_1 + \alpha_2) \leftrightarrow \beta = 1.71^2 \quad (\text{B.17})$$

On the other hand, from Eq. (B.18), the ion density response is

$$\frac{\tilde{n}_i}{n_0} = -\frac{q\tilde{\phi}}{T_i} - (\omega - \omega_i^*) \frac{e^{-\Lambda_i} I_0(\Lambda_i)}{\sqrt{2}k_{\parallel}v_{T_i}} Z(\xi_i) \frac{q\tilde{\phi}}{T_i} + (\omega - \omega_i^*) \frac{e^{-\Lambda_i} I_0(\Lambda_i)}{\sqrt{2}k_{\parallel}v_{T_i}} (1 + \xi_i Z(\xi_i)) \frac{q}{T_i} \frac{\sqrt{2}v_{T_i}\tilde{A}_{\parallel}}{c}. \quad (\text{B.18})$$

The vector potential response function is calculated from Eqs. (B.1-B.3):

$$\frac{\sqrt{2}V_e e}{cT_e} \tilde{A}_{\parallel} = H_F \frac{e\tilde{\phi}}{T_e}, \quad (\text{B.19})$$

where

$$H_F = -\frac{\tilde{\beta}_e}{\chi^2 \hat{k}_{\parallel}} \frac{i(1 - 2\chi/\hat{\omega})}{\left(\frac{1}{\hat{\omega}_{\parallel}^*} + \frac{i}{\hat{\omega}} + \frac{i(1 + \alpha_t m)(\alpha_1 + \alpha_2)}{(\alpha_0 \hat{\omega} + i\chi_1 \sqrt{2}\hat{\omega}_{LF})} \right)}. \quad (\text{B.20})$$

The dispersion relation in normalized form is

$$\begin{aligned}
D(\hat{k}_\parallel, \chi, \hat{\omega}) = & 1 + \left(\hat{\omega} + 2\chi \frac{T_i}{T_e} \right) \frac{\hat{I}_0}{\hat{k}_\parallel} \left(\frac{\hat{\xi} \hat{k}_\parallel}{\hat{\omega}} Z(\hat{\xi}) - (1 + \hat{\xi} Z(\hat{\xi})) H_F \right) \\
& + \frac{T_i}{T_e} \frac{(2\chi + i\hat{\omega}_\parallel^*) \left(\frac{3}{2} \hat{\omega} + i\kappa \hat{\omega}_{LF} \right) + i\beta 2\chi \hat{\omega}_\parallel^*}{(\hat{\omega} + i\hat{\omega}_\parallel^*) \left(\frac{3}{2} \hat{\omega} + i\kappa \hat{\omega}_{LF} \right) + i\beta \hat{\omega} \hat{\omega}_\parallel^*},
\end{aligned} \tag{B.21}$$

where

$$\hat{\omega}_{LF} = \frac{\hat{k}_\parallel^2}{2 \left(\frac{|\hat{k}_\parallel|}{\sqrt{2}} + \alpha_3 \hat{v} \right)}. \tag{B.22}$$

Eq. (B.21) can be solved numerically for the maximum growth rate. Figure B.1 shows contour of maximum growth rate from the numerical solution of dispersion relations for various models. Especially, sub-figure (b) represent the solution of Eq. (B.21) from the electromagnetic fluid model with Landau fluid closure. Figure B.2 shows contours of maximum growth rate for electromagnetic fluid, electromagnetic fluid with Landau closure and collision operator containing electromagnetic kinetic model.

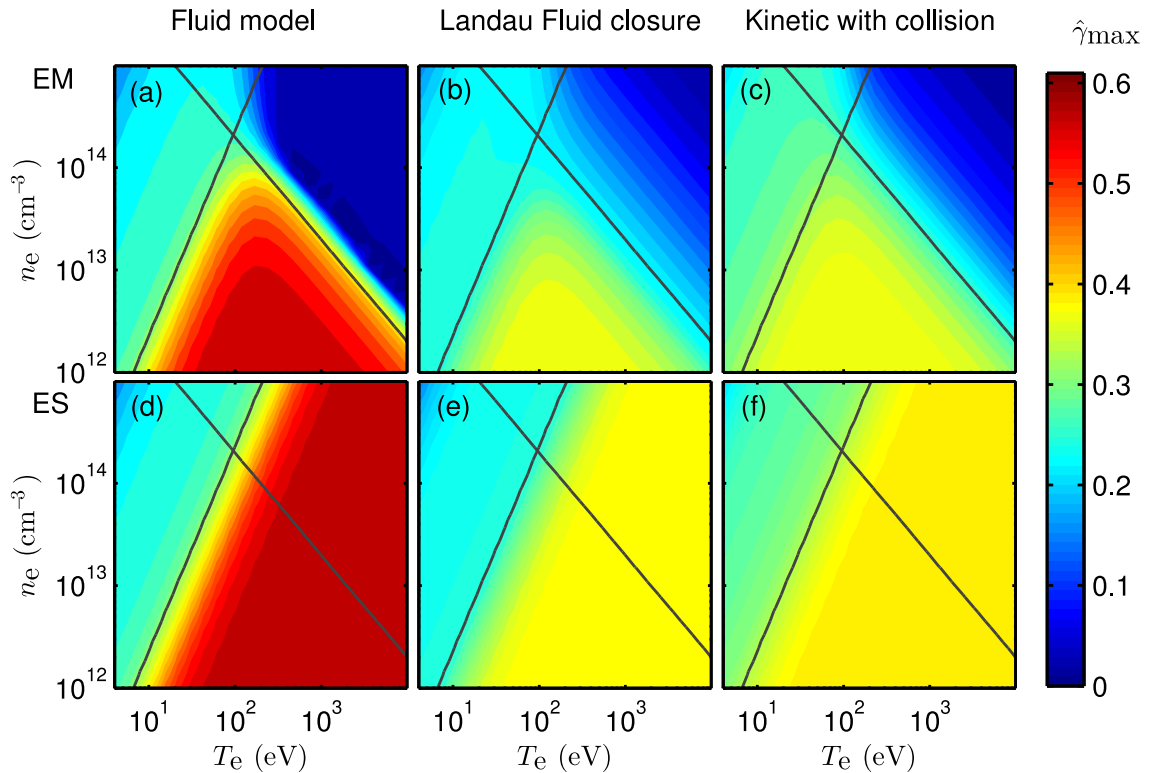


Figure B.1: Contour plots of maximum growth rate for (a) electromagnetic (EM) fluid model, (b) EM Landau fluid model, (c) EM kinetic with arbitrary collision model, (d) electrostatic (ES) fluid model, (e) ES Landau fluid model and (f) ES kinetic with arbitrary collision model. The finite ion temperature effect was suppressed here by setting $T_i/T_e = 0.0001$. The solid and dashed line represent the contours for $\hat{\nu} = 1$ and $\tilde{\beta}_e = 1$, respectively.

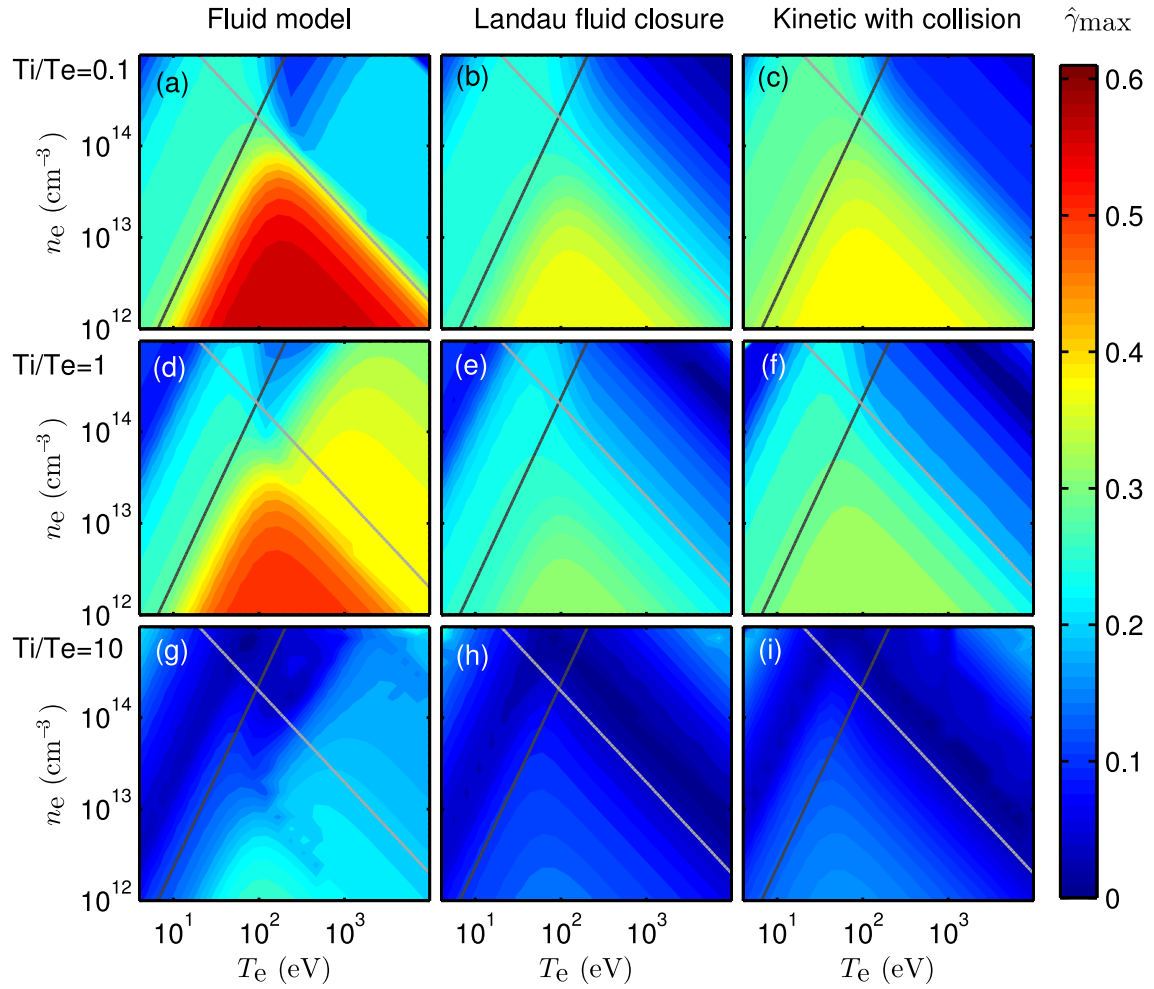


Figure B.2: Contour plots of normalized maximum growth rates, $\hat{\gamma}_{\max}$, for electromagnetic (EM) models. The first, second and third row of subplots are obtained for $T_i/T_e = 0.1$, $T_i/T_e = 1.0$ and $T_i/T_e = 10.0$, respectively. The black and gray line represent the contours for $\hat{v} = 1$ and $\tilde{\beta}_e = 1$, respectively.

Appendix C

Mass Dependent Normalization and Velocity Space Truncation

A numerical analysis of a physical system requires proper normalizations of physical variables and dimensional quantities of model equations. One possible choice of normalizing velocity of the Gyrokinetic equation is using a reference thermal velocity, $\tilde{v} = \sqrt{\tilde{T}/\tilde{m}}$, where \tilde{T} and \tilde{m} are reference normalizing temperature and mass. However, using the same normalizing velocity for all species with different masses and temperatures are inefficient in maintaining same level of parallel velocity grid resolution for each species. This problem can be solved by performing normalizations with temperature and mass dependent normalization factors (See Appendix E). However, current COGENT code is implemented with mass dependent normalization considering small temeperature variations across the physical domain. Here, we describe the mass dependent velocity normalizations. The fundamental parameter for normalizing parallel velocity coordinate for two kinetic species is:

$$v_{\parallel\alpha} = \hat{v}_{\parallel\alpha}\tilde{u}_{\alpha} = \hat{v}_{\parallel\alpha}\tilde{v}/(\sqrt{\hat{m}_{\alpha}}), \quad (C.1)$$

where $\alpha = \{i, e\}$ and $\hat{m}_\alpha = m_\alpha/\tilde{m}$.

We consider following normalization parameters:

$$t = \tilde{t}\tilde{\tau} = \tilde{t}\tilde{L}/\tilde{v}, \quad (\text{C.2})$$

$$\nabla = \hat{\nabla}/\tilde{L}, \quad (\text{C.3})$$

$$v_{\parallel\alpha} = \hat{v}_{\parallel\alpha}\tilde{u}_\alpha = \hat{v}_{\parallel\alpha}\tilde{v}/(\sqrt{\hat{m}_\alpha}), \quad (\text{C.4})$$

$$n_\alpha = \hat{n}_\alpha\tilde{n}, \quad (\text{C.5})$$

$$f_\alpha = \hat{f}_\alpha\tilde{f} = \hat{f}_\alpha\frac{\tilde{n}}{\pi\tilde{v}^3}, \quad (\text{C.6})$$

$$\Phi = \hat{\Phi}\tilde{\Phi} = \hat{\Phi}\tilde{T}/e, \quad (\text{C.7})$$

$$\mu = \hat{\mu}\tilde{\mu} = \hat{\mu}\tilde{T}/(2\tilde{B}), \quad (\text{C.8})$$

$$\mathbf{G}_\alpha = \hat{\mathbf{G}}_\alpha\tilde{G} = \hat{\mathbf{G}}_\alpha\tilde{T}/\tilde{L}, \quad (\text{C.9})$$

$$\omega_{ci} = \hat{\omega}_{ci}\tilde{\Omega} = \hat{\omega}_{ci}e\tilde{B}/\tilde{m}. \quad (\text{C.10})$$

Applying normalizations on Eq. (4.1), we get the normalized Gyrokinetic Vlasov equation:

$$\frac{\partial(\hat{B}_{\parallel\alpha}^*\hat{f}_\alpha)}{\partial\hat{t}} + \nabla_{\hat{\mathbf{R}}}\cdot\left(\dot{\hat{\mathbf{R}}}_\alpha\hat{B}_{\parallel\alpha}^*\hat{f}_\alpha\right) + \frac{\partial}{\partial\hat{v}_{\parallel\alpha}}\left(\dot{\hat{v}}_{\parallel\alpha}\hat{B}_{\parallel\alpha}^*\hat{f}_\alpha\right) = 0. \quad (\text{C.11})$$

where

$$\dot{\hat{\mathbf{R}}}_\alpha = \frac{\hat{v}_{\parallel\alpha}}{\sqrt{\hat{m}_\alpha}}\frac{\hat{\mathbf{B}}_\alpha^*}{\hat{B}_{\parallel\alpha}^*} + \frac{La}{Z_\alpha}\frac{\hat{\mathbf{b}}\times\hat{\mathbf{G}}_\alpha}{\hat{B}_{\parallel\alpha}^*}, \quad (\text{C.12})$$

$$\dot{\hat{v}}_{\parallel\alpha} = -\frac{\hat{\mathbf{B}}_\alpha^*\cdot\hat{\mathbf{G}}_\alpha}{\sqrt{\hat{m}_\alpha}\hat{B}_{\parallel\alpha}^*}, \quad (\text{C.13})$$

$$\hat{\mathbf{B}}_{\alpha}^* = \hat{\mathbf{B}} + \frac{La}{Z_{\alpha}} \sqrt{\hat{m}_{\alpha}} \hat{v}_{\parallel\alpha} \nabla_{\hat{\mathbf{R}}} \times \hat{\mathbf{b}}, \quad (C.14)$$

$$\hat{\mathbf{G}}_{\alpha} = Z_{\alpha} \nabla_{\hat{\mathbf{R}}} \hat{\Phi} + \frac{\hat{\mu}}{2} \nabla_{\hat{\mathbf{R}}} \hat{B} + \hat{v}_{\parallel\alpha}^2 \hat{\mathbf{k}}. \quad (C.15)$$

The normalized poisson equation is

$$\hat{\nabla} \cdot \left\{ \left[De^2 \mathbf{I} + La^2 \sum_i \frac{Z_i \hat{n}_i}{\hat{m}_i \hat{\omega}_{ci}^2} (\mathbf{I} - \mathbf{b} \mathbf{b}^T) \right] \hat{\nabla} \hat{\Phi} \right\} = \hat{n}_e - \sum_i Z_i \hat{n}_i, \quad (C.16)$$

where the Debye number and Larmor number are defined as

$$La = \tilde{v}/(\tilde{\Omega} \tilde{L}) = \tilde{v} \tilde{m}/(e \tilde{L} \tilde{B}), \quad (C.17)$$

$$De = \tilde{\lambda}_D / \tilde{L} = \sqrt{\epsilon_0 \tilde{T} / (\tilde{n} e^2)} / \tilde{L}. \quad (C.18)$$

In the mean time, the Maxwellian distribution function,

$$f_{M\alpha} = n_{\alpha} \left(\frac{m_{\alpha}}{2\pi T_{\alpha}} \right)^{3/2} \exp \left[-\frac{m_{\alpha} (v_{\parallel\alpha} - v_{\parallel\alpha s})^2 + m_{\alpha} v_{\perp\alpha}^2}{2T_{\alpha}} \right] \quad (C.19)$$

is normalized to

$$\hat{f}_{M\alpha} = \frac{\hat{n}_{\alpha}}{\sqrt{\pi}} \left(\frac{\hat{m}_{\alpha}}{2\hat{T}_{\alpha}} \right)^{3/2} \exp \left[-\frac{(\hat{v}_{\parallel\alpha} - \hat{v}_{\parallel\alpha s})^2 + \hat{\mu}_{\alpha} \hat{B}}{2\hat{T}_{\alpha}} \right]. \quad (C.20)$$

In a gyrokinetic code that uses a continuum method, the distribution function at each configuration grid point need to be deposited in the two dimensional (2D) velocity space (See Fig. C.1 and C.2). Because of finite number of discretized points in the 2D velocity space, the distribution function deposited in the velocity space will have a truncation of high-velocity components. In order to minimize the error from the truncation of the tail of the distribution function, one needs

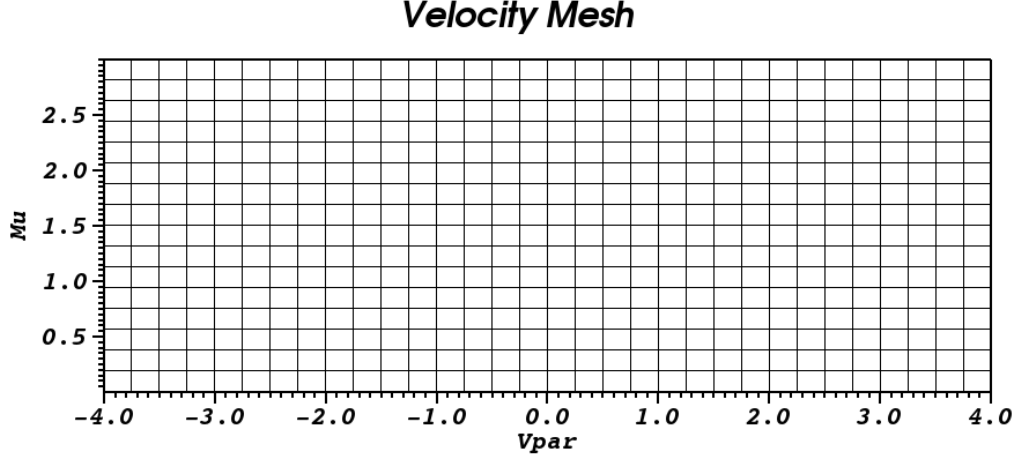


Figure C.1: A sample mesh of velocity space for a continuum gyrokinetic code.

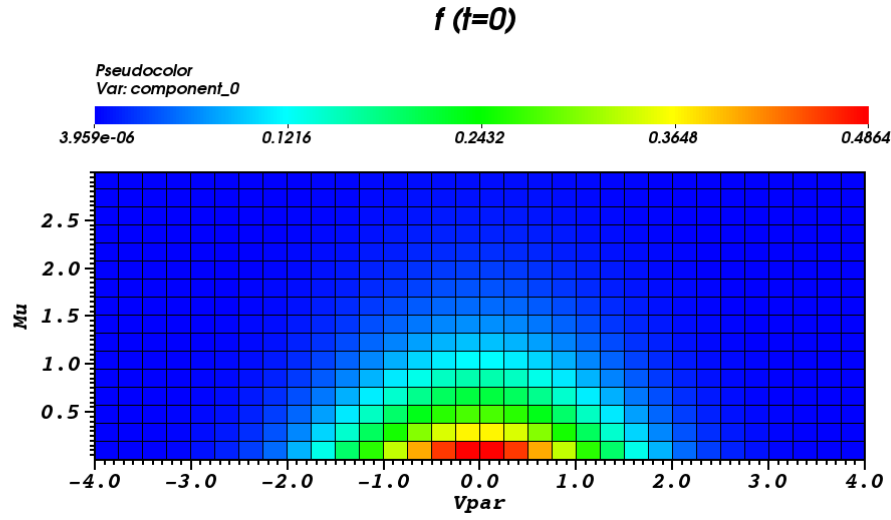


Figure C.2: A sample Maxwellian distribution function deposited in a velocity space grid.

to increase the maximum value of the domain in the velocity space. The velocity coordinate in μ direction does not depend on the mass of species but it only depends on the magnetic field and species temperature. If the temperatures are comparable, the different species will have similar maximum value in perpendicular direction regardless of the species mass. However, the parallel velocity coordinate will change for the different mass species for given temperature.

The velocity truncated grid can be a good approximation for discretized representation of distribution functions. For example, the error in calculating density from the truncated Maxwellian

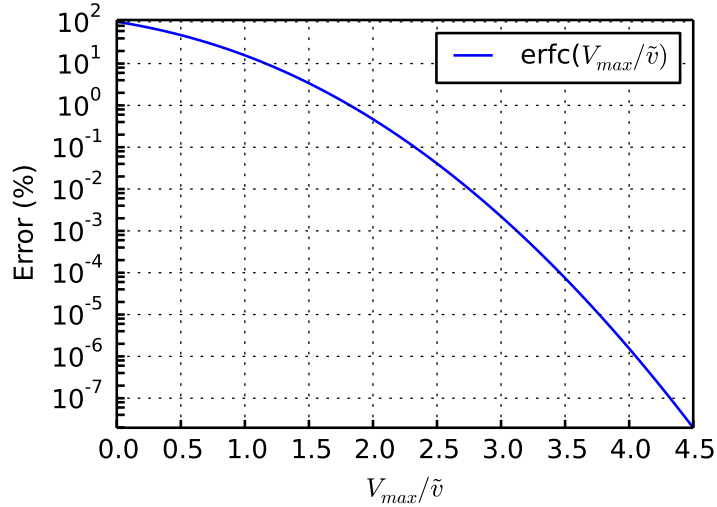


Figure C.3: The complementary error function from the truncated Maxwellian distribution function.

distribution function is rapidly decreased as the $\hat{V}_{||max}$ increased to several times of characteristic velocity, $\tilde{v} \sim \sqrt{(\tilde{T}/\tilde{m})}$. For the truncated Maxwellian distribution function, the analytic truncation error is represented by the complementary error function:

$$\frac{\int_{-\infty}^{\infty} \exp(-v^2/\tilde{v}^2) dv - \int_{-V_{max}}^{V_{max}} \exp(-v^2/\tilde{v}^2) dv}{\int_{-\infty}^{\infty} \exp(-v^2/\tilde{v}^2) dv} = \text{erfc}(V_{max}/\tilde{v}). \quad (\text{C.21})$$

If we set the $V_{max} = 2\tilde{v}$, the density obtained from the truncated distribution function shows about 0.5 % deviation from the non-truncated distribution function (See Fig. C.3). Moreover the truncation velocity $V_{max} = 4\tilde{v}$ gives only about $10^{-6}\%$ error. Therefore, the use of truncation velocity larger than characteristic velocity by twice is a good approximation of the original Maxwellian distribution function.

Appendix D

Derivation and numerical solution of dispersion relation, Eq. (4.7)

In order to derive the linear dispersion relation of the governing equations in the original 4D and new 5D COGENT code, we first consider magnetic field component aligned in the magnetic flux surfaces. Consider linear perturbation of gyrokinetic equation, Eq. (4.1), which magnetic field vectors are aligned in y-z surfaces. In the Gyrokinetic equation, the convective derivative terms,

$$\dot{\mathbf{R}}_\alpha \cdot \nabla_{\mathbf{R}} f_\alpha = \frac{\partial f_\alpha}{\partial x} \left(\frac{b_y}{B} \frac{\partial \Phi}{\partial z} - \frac{b_y}{B} \frac{\partial \Phi}{\partial y} \right) + \frac{b_z}{B} \frac{\partial \Phi}{\partial x} \frac{\partial f_\alpha}{\partial y} + v_{\parallel} b_y \frac{\partial f_\alpha}{\partial y} - \frac{b_y}{B} \frac{\partial \Phi}{\partial x} \frac{\partial f_\alpha}{\partial z} + v_{\parallel} b_z \frac{\partial f_\alpha}{\partial z} \quad (\text{D.1})$$

and

$$\dot{v}_{\parallel \alpha} \frac{\partial f_\alpha}{\partial v_{\parallel}} = - \frac{Z_\alpha e}{m_\alpha} b_z \frac{\partial \Phi}{\partial z} \frac{\partial f_\alpha}{\partial v_{\parallel}} - \frac{Z_\alpha e}{m_\alpha} b_y \frac{\partial \Phi}{\partial y} \frac{\partial f_\alpha}{\partial v_{\parallel}}, \quad (\text{D.2})$$

are written in terms of the decomposed magnetic field, $b_y = B_y/B$ and $b_z = B_z/B$ for $\mathbf{B} = B_y \hat{\mathbf{y}} + B_z \hat{\mathbf{z}}$ (see Fig. D.1). The distribution function, f_α , and electric potential, Φ , in the Eq. (4.1) is linearized by $f_\alpha = \tilde{f}_\alpha + F_\alpha$ and $\Phi = \tilde{\Phi} + \Phi_0$ where \tilde{f}_α and $\tilde{\Phi}$ are perturbed distribution and electric potential,

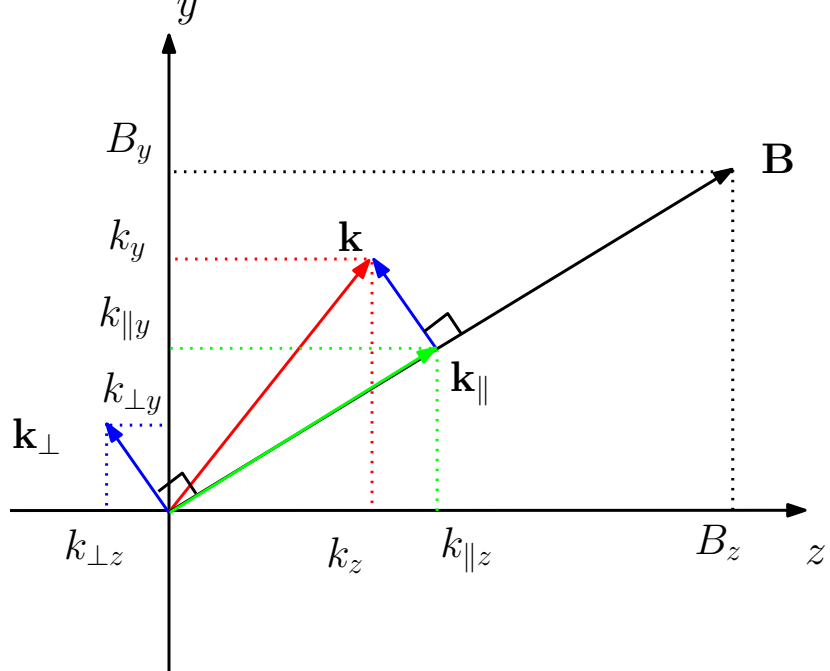


Figure D.1: Magnetic field vector, \mathbf{B} , and the decomposition of wave vector, \mathbf{k} .

respectively. The perturbed quantities assumed to have Fourier normal mode perturbations, such as, $\tilde{f}_\alpha \sim f_{\alpha 1} \exp(ik_x x + ik_y y + ik_z z - i\omega t)$ and $\tilde{\Phi} \sim \Phi_1 \exp(ik_x x + ik_y y + ik_z z - i\omega t)$. The background distribution function is assumed to be have a form of Maxwellian distribution and integrated over velocity space to be a background density of species α , i.e. $\bar{n}_\alpha = \int F_\alpha d\mathbf{v}_\perp d\mathbf{v}_\parallel$. The equilibrium or background electric potential, Φ_0 , is assumed to be zero. The linearized gyrokinetic equation, Eq. (4.1), becomes

$$f_{\alpha 1} = \frac{\frac{c(k_z b_y - k_y b_z)}{B} \Phi_1 \frac{\partial F_\alpha}{\partial x} - \frac{Z_\alpha e}{m_\alpha} (k_z b_z + k_y b_y) \frac{\partial F_\alpha}{\partial v_\parallel} \Phi_1}{\omega - v_\parallel (k_y b_y + k_z b_z) + i\nu_\alpha}. \quad (\text{gaussian}) \quad (\text{D.3})$$

Note that the equation is written in Gaussian unit system.

The linearized gyrokinetic Vlasov equation, Eq. (D.3), in the above subsection describes linear perturbation of distribution function for ions and electrons. The perturbed potential response

is calculated by the Gyrokinetic Poisson equation,

$$\nabla \cdot \left\{ \left(\epsilon_0 \begin{bmatrix} 1 & 0 & 0 \\ 0 & 1 & 0 \\ 0 & 0 & 1 \end{bmatrix} + \frac{m_i \bar{n}_i}{B^2} \begin{bmatrix} 1 & 0 & 0 \\ 0 & 1 - b_y^2 & -b_y b_z \\ 0 & -b_y b_z & 1 - b_z^2 \end{bmatrix} \right) \nabla \Phi \right\} = e \left(n_e - \sum_i Z_i \bar{n}_i \right). \quad (\text{D.4})$$

The Gyrokinetic Poisson equation is linearized considering an exponentially varying background density profile in radial (x) direction, $\frac{d\bar{n}_i}{\bar{n}_i dx} = -L_n^{-1}$. The linearized Gyrokinetic Poisson equation in Gaussian unit system is

$$\frac{m_i c^2}{B^2} \left[-L_n^{-1} i k_x \tilde{\Phi} - \left(\frac{k_x^2 B^2}{4\pi m_i c^2 \bar{n}_i} + k_x^2 \right) \tilde{\Phi} - \left(\frac{k_y^2 B^2}{4\pi m_i c^2 \bar{n}_i} + k_y^2 b_z^2 \right) \tilde{\Phi} + 2 b_y b_z k_y k_z \tilde{\Phi} - \left(\frac{k_z^2 B^2}{4\pi m_i c^2 \bar{n}_i} + k_z^2 b_y^2 \right) \tilde{\Phi} \right] = -\frac{e}{\bar{n}_i} \sum_{\alpha=i,e} Z_\alpha \int \tilde{f}_\alpha d\nu_\perp d\nu_\parallel. \quad (\text{D.5})$$

The RHS of Eq. (D.5) is coupled with linearized Gyrokinetic Vlasov equation, Eq. (D.3), for species α :

$$\begin{aligned} & -\frac{e}{\bar{n}_i} \sum_{\alpha=i,e} Z_\alpha \int \tilde{f}_\alpha d\nu_\perp d\nu_\parallel \\ &= -\frac{e}{\bar{n}_i} \sum_{\alpha=i,e} Z_\alpha \int \frac{\frac{c(k_z b_y - k_y b_z)}{B} \Phi_1 \frac{\partial F_\alpha}{\partial x} - \frac{Z_\alpha e}{m_\alpha} (k_z b_z + k_y b_y) \Phi_1 \frac{\partial F_\alpha}{\partial v_\parallel}}{\omega - v_\parallel (k_y b_y + k_z b_z) + i v_\alpha} d\nu_\perp d\nu_\parallel \end{aligned} \quad (\text{D.6})$$

where $F_\alpha = \bar{n}_\alpha(x) \frac{2}{\pi v_{\text{th},\alpha}^2} \exp(-(\nu_\perp^2 + \nu_\parallel^2)/v_{\text{th},\alpha}^2)$ and $\int F_\alpha d\nu_\perp d\nu_\parallel = \bar{n}_\alpha(x)$ and $\bar{n}_i = \bar{n}_e$. Let $m_\alpha v_{\text{th},\alpha}^2/2 = T_\alpha$ and $\frac{\omega + i v_\alpha}{(k_y b_y + k_z b_z) v_{\text{th},\alpha}} = \zeta_\alpha$, $Z_{(\alpha=i)} = 1$ and $v_i = 0$. Evaluation of the integration in the RHS of Eq. (D.5) yields the plasma dispersion function,

$$Z(\zeta) = \frac{1}{\sqrt{\pi}} \int_{-\infty}^{\infty} \frac{\exp[-t^2]}{t - \zeta} dt. \quad (\text{D.7})$$

Then we get a dispersion relation,

$$\begin{aligned}
& \frac{T_i}{m_i} \frac{1}{\omega_{ci}^2} \left[-L_n^{-1} ik_x - \left(\frac{k_x^2 B^2}{4\pi m_i c^2 \bar{n}_i} + k_x^2 \right) - \left(\frac{k_y^2 B^2}{4\pi m_i c^2 \bar{n}_i} + k_y^2 b_z^2 \right) \right. \\
& \quad \left. + 2b_y b_z k_y k_z - \left(\frac{k_z^2 B^2}{4\pi m_i c^2 \bar{n}_i} + k_z^2 b_y^2 \right) \right] \\
& = 1 + \left[- \frac{T_i}{T_e} \frac{\omega_{*e}}{(k_y b_y + k_z b_z) v_{th,i}} \frac{(k_z b_y - k_y b_z)}{k_y} \right. \\
& \quad \left. + \frac{\omega}{(k_y b_y + k_z b_z) v_{th,i}} \right] Z \left(\frac{\omega}{(k_y b_y + k_z b_z) v_{th,i}} \right) \\
& \quad + \frac{T_i}{T_e} + \left[\frac{T_i}{T_e} \frac{\omega_{*e}}{(k_y b_y + k_z b_z) v_{th,e}} \frac{(k_z b_y - k_y b_z)}{k_y} \right. \\
& \quad \left. + \frac{T_i}{T_e} \frac{\omega}{(k_y b_y + k_z b_z) v_{th,e}} \right] Z \left(\frac{\omega + i\nu_e}{(k_y b_y + k_z b_z) v_{th,e}} \right) \quad (D.8)
\end{aligned}$$

where $\omega_{*e} = k_y c T_e / (e B L_n)$. This dispersion relation can be simplified by applying normalization $\omega_s^* \equiv c_s / L_n$, $\omega = \hat{\omega} \omega_s^*$, $k_\perp = \hat{k}_\perp / \rho_s$, $k_\parallel = \hat{k}_\parallel c_s / (L_n v_{th,e})$, then we get the dispersion relation for electrostatic kinetic drift wave,

$$\begin{aligned}
& \frac{T_i}{m_i} \frac{1}{\omega_{ci}^2} \left[-ik_x \frac{1}{L_n} - \left(\frac{\omega_{ci}^2}{\omega_{pi}^2} + 1 \right) k_x^2 - \left(\frac{\omega_{ci}^2}{\omega_{pi}^2} + b_z^2 \right) k_y^2 + 2b_y b_z k_y k_z - \left(\frac{\omega_{ci}^2}{\omega_{pi}^2} + b_y^2 \right) k_z^2 \right] \\
& = 1 + \left[\frac{\hat{\omega}}{\hat{k}_\parallel} + \frac{T_i}{T_e} \frac{\hat{k}_\perp}{\hat{k}_\parallel} \right] \sqrt{\frac{m_i T_e}{m_e T_i}} Z \left(\frac{\hat{\omega}}{\hat{k}_\parallel} \sqrt{\frac{m_i T_e}{m_e T_i}} \right) + \frac{T_i}{T_e} + \left[\frac{T_i}{T_e} \frac{\hat{\omega}}{\hat{k}_\parallel} - \frac{T_i}{T_e} \frac{\hat{k}_\perp}{\hat{k}_\parallel} \right] Z \left(\frac{\hat{\omega} + i\nu_e}{\hat{k}_\parallel} \right) \quad (D.9)
\end{aligned}$$

where $k_\parallel = k_y b_y + k_z b_z$, $k_\perp = (k_y b_z - k_z b_y)$ and $k_y = ((\hat{k}_\perp / \rho_s) b_z + (\hat{k}_\parallel c_s / (L_n v_{th,e})) b_y) / (b_y^2 + b_z^2)$, $k_z = ((\hat{k}_\parallel c_s / (L_n v_{th,e})) b_z - (\hat{k}_\perp / \rho_s) b_y) / (b_y^2 + b_z^2)$.

The solution of the Eq. (D.9) can be found numerically. Fig. D.2 shows an example of the numerical procedure to find the solutions of dispersion relation for plasma density, $n = 10^{14} \text{ cm}^{-3}$, and electron and ion temperature, $T_e = T_i = 400 \text{ eV}$. Two contour lines (in blue and green) represent $\text{Im}(D) = 0$ and $\text{Re}(D) = 0$, for independent variables $\text{Im}(\hat{\omega})$ and $\text{Re}(\hat{\omega})$ at fixed $\hat{k}_\parallel = 0.09409$ and $\hat{k}_\perp = 0.7566$. Where the two contour lines intersect each other, we get solution points that satisfy

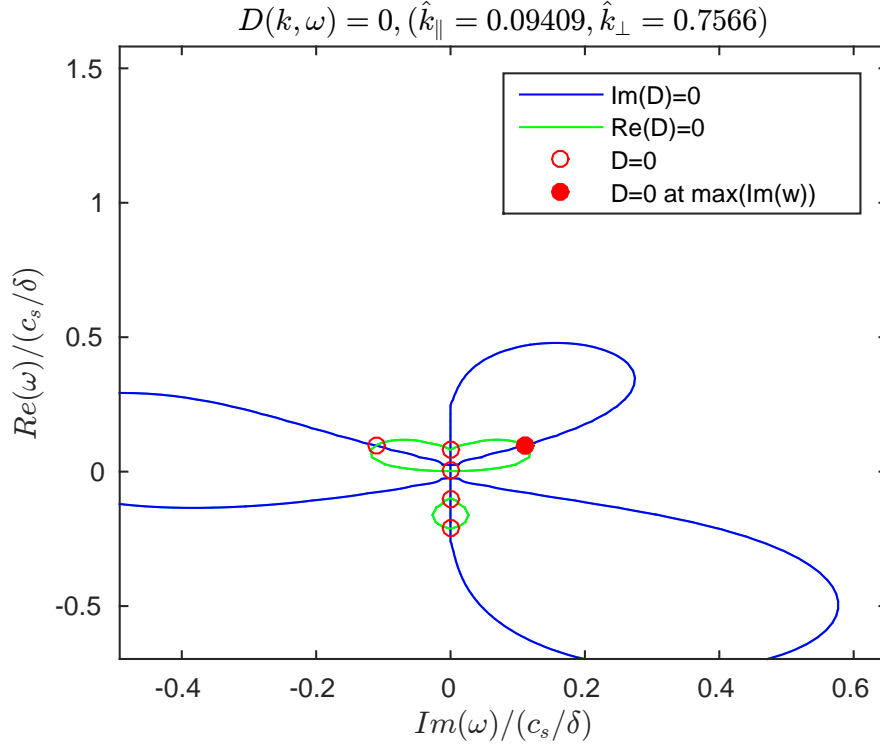


Figure D.2: An example of root finding for dispersion relation. The positions of the circles represent complex solutions of the dispersion relation for given wave numbers. The closed circle corresponds to the solution with the highest growth rate.

dispersion relation Eq. (D.9) ($D(k, \omega) = 0$) and the closed circle represent the most unstable solution. One can obtain a map of maximum growth rate as function of wave numbers for given plasma status by collecting the largest growth rate for various parallel and perpendicular wave numbers. Fig. D.3 is an example of the contour lines of growth rate.

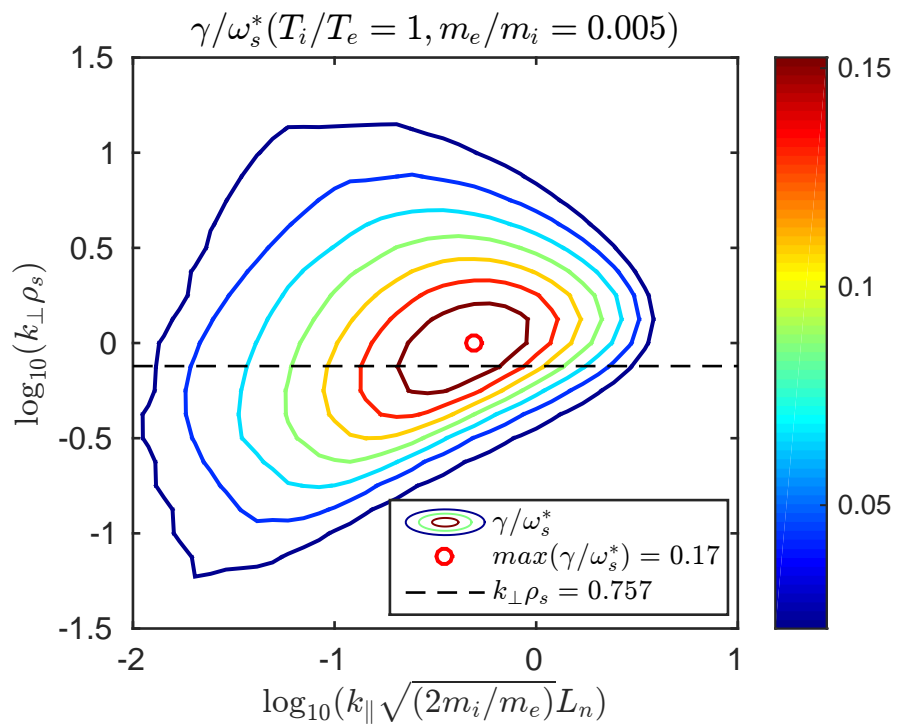


Figure D.3: A contour plot depicts imaginary roots of dispersion relation for given perpendicular and parallel wave numbers.

Appendix E

Temperature dependent normalization for COGENT

Now we perform a temperature dependent normalization by converting velocity coordinates to dimensionless coordinates independent of species temperature and mass, i.e. $(v_{\parallel}, \mu) \rightarrow (\hat{v}_{\parallel mT}, \hat{\mu}_{mT})$, where $\hat{v}_{\parallel mT}$ and $\hat{\mu}_{mT}$ refers to mass and temperature normalized parallel velocity and magnetic moment. Conserved form of Gyrokinetic equation is

$$\frac{\partial(B_{\parallel\alpha}^* f_{\alpha})}{\partial t} + \nabla_{\mathbf{R}} \cdot (\dot{\mathbf{R}}_{\alpha} B_{\parallel\alpha}^* f_{\alpha}) + \frac{\partial}{\partial v_{\parallel\alpha}} (\dot{v}_{\parallel\alpha} B_{\parallel\alpha}^* f_{\alpha}) = 0. \quad (\text{E.1})$$

We consider following normalization parameters:

$$t = \hat{t}\tilde{\tau} = \hat{t}\tilde{L}/\tilde{v}, \quad (\text{E.2})$$

$$\nabla = \hat{\nabla}/\tilde{L}, \quad (\text{E.3})$$

$$v_\alpha = \hat{v}_{\alpha mT} \tilde{v}_{\alpha mT}(\hat{R}) = \hat{v}_{\alpha mT} \sqrt{\frac{\hat{T}_\alpha(R)}{\hat{m}_\alpha}} \tilde{v}, \quad (\text{E.4})$$

$$v_{\parallel\alpha} = \hat{v}_{\parallel\alpha mT} \tilde{v}_{\alpha mT}(\hat{R}) = \hat{v}_{\parallel\alpha mT} \sqrt{\frac{\hat{T}_\alpha(R)}{\hat{m}_\alpha}} \tilde{v}, \quad (\text{E.5})$$

$$v_{\perp\alpha} = \hat{v}_{\perp\alpha mT} \tilde{v}_{\alpha mT}(\hat{R}) = \hat{v}_{\perp\alpha mT} \sqrt{\frac{\hat{T}_\alpha(R)}{\hat{m}_\alpha}} \tilde{v}, \quad (\text{E.6})$$

$$n_\alpha = \hat{n}_\alpha \tilde{n}, \quad (\text{E.7})$$

$$f_\alpha = \hat{f}_\alpha \tilde{f}, \quad (\text{E.8})$$

$$\Phi = \hat{\Phi}\tilde{\Phi} = \hat{\Phi}\tilde{T}/e, \quad (\text{E.9})$$

$$\mu_\alpha = \hat{\mu}_{\alpha mT} \tilde{\mu}_{\alpha mT} = \left(\frac{\hat{v}_{\perp mT}^2}{\hat{B}}\right) \left(\frac{\tilde{T}\hat{T}_\alpha}{2\tilde{B}}\right), \quad (\text{E.10})$$

$$\mathbf{G}_\alpha = \hat{\mathbf{G}}_\alpha \tilde{G} = \hat{\mathbf{G}}_\alpha \tilde{T}/\tilde{L}, \quad (\text{E.11})$$

$$\omega_{ci} = \hat{\omega}_{ci} \tilde{\Omega} = \hat{\omega}_{ci} e \tilde{B}/\tilde{m}. \quad (\text{E.12})$$

where $\hat{v}^{mT} = \sqrt{\hat{m}_\alpha/\hat{T}_\alpha} \hat{v}$, $\hat{\mu}_{\alpha mT} = \hat{v}_{\perp mT}^2/\hat{B} = \hat{\mu}/\hat{T}_\alpha$, $\hat{\mu} = \hat{m}_\alpha \hat{v}_\perp^2/\hat{B}$. Then, the normalized form of Gyrokinetic equation is

$$\frac{\partial(\hat{B}_{\parallel\alpha}^* \hat{f}_\alpha)}{\partial \hat{t}} + \nabla_{\hat{\mathbf{R}}} \cdot \left(\hat{\mathbf{R}}_\alpha \hat{B}_{\parallel\alpha}^* \hat{f}_\alpha \right) + \frac{\partial}{\partial \hat{v}_{\parallel\alpha}} \left(\dot{\hat{v}}_{\parallel\alpha} \hat{B}_{\parallel\alpha}^* \hat{f}_\alpha \right) = 0, \quad (\text{E.13})$$

with

$$\hat{\mathbf{R}}_\alpha = \sqrt{\frac{\hat{T}_\alpha(\hat{R})}{\hat{m}_\alpha}} \hat{v}_{\parallel\alpha mT} \hat{\mathbf{B}}_\alpha^* + \frac{La}{Z_\alpha} \frac{\hat{\mathbf{b}} \times \hat{\mathbf{G}}_\alpha}{\hat{B}_{\parallel\alpha}^*}, \quad (\text{E.14})$$

$$\dot{\hat{v}}_{\parallel\alpha mT} = -\frac{1}{\hat{m}_\alpha} \sqrt{\frac{\hat{m}_\alpha}{\hat{T}_\alpha(\hat{R})}} \frac{\hat{\mathbf{B}}_\alpha^* \cdot \hat{\mathbf{G}}_\alpha}{\hat{B}_{\parallel\alpha}^*}, \quad (\text{E.15})$$

and

$$\hat{\mathbf{B}}_\alpha^* = \hat{\mathbf{B}} + \frac{La}{Z_\alpha} \sqrt{\frac{\hat{T}_\alpha(\hat{R})}{\hat{m}_\alpha}} \hat{m}_\alpha \hat{v}_{\parallel\alpha mT} \nabla_{\hat{\mathbf{R}}} \times \hat{\mathbf{b}}, \quad (\text{E.16})$$

$$\hat{\mathbf{G}}_\alpha = Z_\alpha \nabla_{\hat{\mathbf{R}}} \hat{\Phi} + \frac{\hat{T}_\alpha \hat{\mu}_{mT}}{2} \nabla_{\hat{\mathbf{R}}} \hat{B} + \hat{T}_\alpha(\hat{R}) \hat{v}_{\parallel\alpha mT}^2 \hat{\kappa}. \quad (\text{E.17})$$

Normalized Maxwellian distribution shows the following form

$$\hat{f}_M = \frac{\hat{n}_\alpha}{\sqrt{\pi}} \left(\frac{\hat{m}_\alpha}{2\hat{T}_\alpha} \right)^{3/2} \exp \left[-\frac{(\hat{v}_{\parallel\alpha mT} - \hat{v}_{\parallel\alpha smT})^2 + \hat{\mu}_{\alpha mT} \hat{B}}{2} \right]. \quad (\text{E.18})$$

Bibliography

- [1] WJ Nuttall. Fusion as an energy source: Challenges and opportunities. *IOP Report*, (9), 2008.
- [2] Garry McCracken and Peter Stott. *Fusion: the Energy of the Universe*. Academic Press, 2012.
- [3] Jeffrey P Freidberg. *Plasma physics and fusion energy*. Cambridge university press, 2008.
- [4] R. Pichs-Madruga Y. Sokona E. Farahani S. Kadner K. Seyboth A. Adler I. Baum S. Brunner P. Eickemeier B. Kriemann J. Savolainen S. Schlmer C. von Stechow T. Zwickel Edenhofer, O. and J.C. Minx (eds.). *Climate Change 2014: Mitigation of Climate Change*. Cambridge Press, 2014.
- [5] Terese (T.C.) Richmond Gary W. Yohe Eds. Melillo, Jerry M. Climate change impacts in the united states: The third national climate assessment. *U.S. Global Change Research Program*, page 841, 2014.
- [6] F Chen Francis. Introduction to plasma physics and controlled fusion. *Plasma Physics*, 1984.
- [7] Robert J Goldston and Paul Harding Rutherford. *Introduction to plasma physics*. CRC Press, 1995.
- [8] Paul M Bellan. *Fundamentals of plasma physics*. Cambridge University Press, 2006.
- [9] Michael A Lieberman and Alan J Lichtenberg. *Principles of plasma discharges and materials processing*. John Wiley & Sons, 2005.
- [10] John Wesson and David J Campbell. *Tokamaks*, volume 149. Oxford university press, 2011.
- [11] JP Friedberg. Ideal magnetohydrodynamics plenum press. *New York*, 1987.
- [12] Peter C Stangeby. *The plasma boundary of magnetic fusion devices*, volume 224. Institute of Physics Publishing Bristol, 2000.
- [13] ASDEX Team. The h-mode of asdex. *Nuclear Fusion*, 29(11):1959, 1989.
- [14] PM Valanju, M Kotschenreuther, SM Mahajan, and John Canik. Super-x divertors and high power density fusion devices a. *Physics of Plasmas*, 16(5):056110, 2009.

- [15] DD Ryutov. Geometrical properties of a snowflake divertor. *Physics of Plasmas*, 14(6):064502, 2007.
- [16] S.I. Krasheninnikov. On scrape off layer plasma transport. *Physics Letters A*, 283(56):368 – 370, 2001.
- [17] S. I. Krasheninnikov, D. A. DiIppolito, and J. R. Myra. Recent theoretical progress in understanding coherent structures in edge and sol turbulence. *Journal of Plasma Physics*, 74:679–717, 10 2008.
- [18] D. A. DiIppolito, J. R. Myra, and S. J. Zweben. Convective transport by intermittent blob-filaments: Comparison of theory and experiment. *Physics of Plasmas*, 18(6):060501, 2011.
- [19] Y Sarazin and Ph Ghendrih. Intermittent particle transport in two-dimensional edge turbulence. *Physics of Plasmas*, 5(12):4214–4228, 1998.
- [20] O Grulke, JL Terry, B LaBombard, and SJ Zweben. Radially propagating fluctuation structures in the scrape-off layer of alcator c-mod. *Physics of Plasmas*, 13(1):012306, 2006.
- [21] P Devynck, J Brotankova, Peter Peleman, M Spolaore, H Figueiredo, M Hron, G Kirnev, E Martines, J Stockel, Guido Van Oost, and V Weinzettl. Dynamics of turbulent transport in the scrape-off layer of the castor tokamak. *Physics of plasmas*, 13(10):102505, 2006.
- [22] R Sánchez, B Ph van Milligen, DE Newman, and BA Carreras. Quiet-time statistics of electrostatic turbulent fluxes from the jet tokamak and the w7-as and tj-ii stellarators. *Physical review letters*, 90(18):185005, 2003.
- [23] TA Carter. Intermittent turbulence and turbulent structures in a linear magnetized plasma. *Physics of plasmas*, 13(1):010701, 2006.
- [24] R.J. Maqueda, D.P. Stotler, and S.J. Zweben. Intermittency in the scrape-off layer of the national spherical torus experiment during h-mode confinement. *Journal of Nuclear Materials*, 415(1, Supplement):S459 – S462, 2011. Proceedings of the 19th International Conference on Plasma-Surface Interactions in Controlled Fusion.
- [25] MV Umansky, SI Krasheninnikov, B LaBombard, and JL Terry. Comments on particle and energy balance in the edge plasma of alcator c-mod. *Physics of Plasmas*, 5(9):3373–3376, 1998.
- [26] Jose A Boedo, D Rudakov, R Moyer, S Krasheninnikov, D Whyte, G McKee, G Tynan, M Schaffer, P Stangeby, Philip West, S Allen, T Evans, R Fonck, E Hollmann, A Leonard, A Mahdavi, G Porter, M Tillack, and G Antar. Transport by intermittent convection in the boundary of the diii-d tokamak. *Physics of Plasmas*, 8(11):4826–4833, 2001.
- [27] DL Rudakov, JA Boedo, RA Moyer, S Krasheninnikov, AW Leonard, MA Mahdavi, GR McKee, GD Porter, PC Stangeby, JG Watkins, WP West, DG Whyte, and G Antar. Fluctuation-driven transport in the diii-d boundary. *Plasma physics and controlled fusion*, 44(6):717, 2002.

- [28] Justin R. Angus, Sergei I. Krasheninnikov, and Maxim V. Umansky. Effects of parallel electron dynamics on plasma blob transport. *Physics of Plasmas*, 19(8):082312, 2012.
- [29] W Horton. Drift waves and transport. *Reviews of Modern Physics*, 71(3):735, 1999.
- [30] Mitsuru Kikuchi. *Frontiers in fusion research: physics and fusion*. Springer Science & Business Media, 2011.
- [31] GQ Yu and SI Krasheninnikov. Dynamics of blobs in scrape-off-layer/shadow regions of tokamaks and linear devices. *Physics of Plasmas*, 10(11):4413–4418, 2003.
- [32] DA D’Ippolito, JR Myra, SI Krasheninnikov, GQ Yu, and A Yu Pigarov. Blob transport in the tokamak scrape-off-layer. *Contributions to Plasma Physics*, 44(1-3):205–216, 2004.
- [33] AY Aydemir. Convective transport in the scrape-off layer of tokamaks. *Physics of plasmas*, 12(6):062503, 2005.
- [34] OE Garcia, NH Bian, and W Fundamenski. Radial interchange motions of plasma filaments. *Physics of plasmas*, 13(8):082309, 2006.
- [35] OE Garcia, V Naulin, AH Nielsen, and J Juul Rasmussen. Turbulence simulations of blob formation and radial propagation in toroidally magnetized plasmas. *Physica Scripta*, 2006(T122):89, 2006.
- [36] D Jovanović, PK Shukla, and F Pegoraro. Effects of the parallel electron dynamics and finite ion temperature on the plasma blob propagation in the scrape-off layer. *Physics of Plasmas*, 15(11):112305, 2008.
- [37] NR Walkden, BD Dudson, and Geoff Fishpool. Characterization of 3d filament dynamics in a mast sol flux tube geometry. *Plasma Physics and Controlled Fusion*, 55(10):105005, 2013.
- [38] F Militello, NR Walkden, T Farley, WA Gracias, J Olsen, F Riva, L Easy, N Fedorczak, I Lupelli, Jens Madsen, AH Nielsen, P Ricci, P Tamain, and J Young. Multi-code analysis of scrape-off layer filament dynamics in mast. *Plasma Physics and Controlled Fusion*, 58(10):105002, 2016.
- [39] Justin R. Angus and Sergei I. Krasheninnikov. Drift wave dispersion relation for arbitrarily collisional plasma. *Physics of Plasmas*, 19(5):052504, 2012.
- [40] P. L. Bhatnagar, E. P. Gross, and M. Krook. A model for collision processes in gases. i. small amplitude processes in charged and neutral one-component systems. *Phys. Rev.*, 94:511–525, May 1954.
- [41] S Krasheninnikov, D Ryutov, and G Yu. Large plasma pressure perturbations and radial convective transport in a tokamak. *J. Plasma Fusion Res.*, 6:139, 2004.
- [42] J. R. Myra and D. A. D’Ippolito. Edge instability regimes with applications to blob transport and the quasicoherent mode. *Physics of Plasmas*, 12(9):092511, 2005.

- [43] G. S. Xu, V. Naulin, W. Fundamenski, J. Juul Rasmussen, A. H. Nielsen, and B. N. Wan. Intermittent convective transport carried by propagating electromagnetic filamentary structures in nonuniformly magnetized plasma. *Physics of Plasmas*, 17(2):022501, 2010.
- [44] J. R. Myra. Current carrying blob filaments and edge-localized-mode dynamics. *Physics of Plasmas*, 14(10):102314, 2007.
- [45] P. Manz, D. Carralero, G. Birkenmeier, H. W. Mller, S. H. Mller, G. Fuchert, B. D. Scott, and U. Stroth. Filament velocity scaling laws for warm ions. *Physics of Plasmas*, 20(10):102307, 2013.
- [46] P Ricci, F D Halpern, S Jolliet, J Loizu, A Mosetto, A Fasoli, I Furno, and C Theiler. Simulation of plasma turbulence in scrape-off layer conditions: the gbs code, simulation results and code validation. *Plasma Physics and Controlled Fusion*, 54(12):124047, 2012.
- [47] B. I. Cohen, M. V. Umansky, W. M. Nevins, M. A. Makowski, J. A. Boedo, D. L. Rudakov, G. R. McKee, Z. Yan, and R. J. Groebner. Simulations of drift resistive ballooning l-mode turbulence in the edge plasma of the dIII-D tokamak. *Physics of Plasmas*, 20(5):055906, 2013.
- [48] B.D. Dudson, M.V. Umansky, X.Q. Xu, P.B. Snyder, and H.R. Wilson. Bout++: A framework for parallel plasma fluid simulations. *Computer Physics Communications*, 180(9):1467 – 1480, 2009.
- [49] Justin R. Angus and Maxim V. Umansky. Modeling of large amplitude plasma blobs in three-dimensions. *Physics of Plasmas*, 21(1):012514, 2014.
- [50] D. Jovanovi, P. K. Shukla, and F. Pegoraro. Effects of the parallel electron dynamics and finite ion temperature on the plasma blob propagation in the scrape-off layer. *Physics of Plasmas*, 15(11):112305, 2008.
- [51] M.V. Umansky, X.Q. Xu, B. Dudson, L.L. LoDestro, and J.R. Myra. Status and verification of edge plasma turbulence code bout. *Computer Physics Communications*, 180(6):887 – 903, 2009.
- [52] X. Q. Xu, R. H. Cohen, T. D. Rognlien, and J. R. Myra. Low-to-high confinement transition simulations in divertor geometry. *Physics of Plasmas*, 7(5):1951–1958, 2000.
- [53] A.S. Kukushkin, H.D. Pacher, V. Kotov, G.W. Pacher, R.A. Pitts, and D. Reiter. Iter divertor performance in the low-activation phase. *Nuclear Fusion*, 53(12):123025, 2013.
- [54] I Furno, C Theiler, D Lanon, A Fasoli, D Iraji, P Ricci, M Spolaore, and N Vianello. Blob current structures in torpex plasmas: experimental measurements and numerical simulations. *Plasma Physics and Controlled Fusion*, 53(12):124016, 2011.
- [55] J. R. Angus and S. I. Krasheninnikov. Inviscid evolution of large amplitude filaments in a uniform gravity field. *Physics of Plasmas*, 21(11):112504, 2014.

- [56] A Kirk, N Ben Ayed, G Counsell, B Dudson, T Eich, A Herrmann, B Koch, R Martin, A Meakins, S Saarelma, R Scannell, S Tallents, M Walsh, H R Wilson, and the MAST team. Filament structures at the plasma edge on mast. *Plasma Physics and Controlled Fusion*, 48(12B):B433, 2006.
- [57] P. Migliucci, V. Naulin, and JET EFDA Contributors. Magnetic signature of current carrying edge localized modes filaments on the joint european torus tokamak. *Physics of Plasmas*, 17(7):072507, 2010.
- [58] N. Vianello, V. Naulin, R. Schrittwieser, H. W. Müller, M. Zuin, C. Ionita, J. J. Rasmussen, F. Mehlmann, V. Rohde, R. Cavazzana, M. Maraschek, and the ASDEX Upgrade Team. Direct observation of current in type-i edge-localized-mode filaments on the asdex upgrade tokamak. *Phys. Rev. Lett.*, 106:125002, 2011.
- [59] Sergei Krasheninnikov. Multifaceted physics of edge plasma in magnetic fusion devices. *Plasma Physics and Controlled Fusion*, 53(7):074017, 2011.
- [60] Richard J Buttery and the DIII-D Team. Diii-d research to address key challenges for iter and fusion energy. *Nuclear Fusion*, 55(10):104017, 2015.
- [61] Justin R. Angus, Maxim V. Umansky, and Sergei I. Krasheninnikov. Review and limitations of 3d plasma blob modeling with reduced collisional fluid equations. *Journal of Nuclear Materials*, 438, Supplement(0):S572 – S575, 2013. Proceedings of the 20th International Conference on Plasma-Surface Interactions in Controlled Fusion Devices.
- [62] Wonjae Lee, J.R. Angus, Maxim V. Umansky, and Sergei I. Krasheninnikov. Electromagnetic effects on plasma blob-filament transport. *Journal of Nuclear Materials*, (0), 2014.
- [63] Wonjae Lee, Maxim V. Umansky, J. R. Angus, and Sergei I. Krasheninnikov. Electromagnetic effects on dynamics of high-beta filamentary structures. *Physics of Plasmas*, 22(1):012505, 2015.
- [64] N. Bisai, A. Das, S. Deshpande, R. Jha, P. Kaw, A. Sen, and R. Singh. Formation of a density blob and its dynamics in the edge and the scrape-off layer of a tokamak plasma. *Physics of Plasmas*, 12(10):102515, 2005.
- [65] D. A. Russell, D. A. DiIppolito, J. R. Myra, B. LaBombard, J. L. Terry, and S. J. Zweben. Numerical investigation of edge plasma phenomena in an enhanced d-alpha discharge at alcator c-mod: Parallel heat flux and quasi-coherent edge oscillations. *Physics of Plasmas*, 19(8):082311, 2012.
- [66] SI Braginskii. Transport processes in a plasma. *Reviews of plasma physics*, 1:205, 1965.
- [67] A Hirose. Drift instabilities in magnetically confined plasmas: A brief overview, 2005. Lecture Notes, Autumn College on Plasma Physics International Centre for Theoretical Physics, Trieste, Italy.

- [68] J. A. Boedo, D. Rudakov, R. Moyer, S. Krasheninnikov, D. Whyte, G. McKee, G. Tynan, M. Schaffer, P. Stangeby, P. West, S. Allen, T. Evans, R. Fonck, E. Hollmann, A. Leonard, A. Mahdavi, G. Porter, M. Tillack, and G. Antar. Transport by intermittent convection in the boundary of the dIII-d tokamak. *Physics of Plasmas (1994-present)*, 8(11):4826–4833, 2001.
- [69] D.L. Rudakov, J.A. Boedo, R.A. Moyer, P.C. Stangeby, J.G. Watkins, D.G. Whyte, L. Zeng, N.H. Brooks, R.P. Doerner, T.E. Evans, M.E. Fenstermacher, M. Groth, E.M. Hollmann, S.I. Krasheninnikov, C.J. Lasnier, A.W. Leonard, M.A. Mahdavi, G.R. McKee, A.G. McLean, A.Yu. Pigarov, W.R. Wampler, G. Wang, W.P. West, and C.P.C. Wong. Far sol transport and main wall plasma interaction in dIII-d. *Nuclear Fusion*, 45(12):1589, 2005.
- [70] J. L. Terry, S. J. Zweben, K. Hallatschek, B. LaBombard, R. J. Maqueda, B. Bai, C. J. Boswell, M. Greenwald, D. Kopon, W. M. Nevins, C. S. Pitcher, B. N. Rogers, D. P. Stotler, and X. Q. Xu. Observations of the turbulence in the scrape-off-layer of alcator c-mod and comparisons with simulation. *Physics of Plasmas*, 10(5):1739–1747, 2003.
- [71] M. Agostini, S. J. Zweben, R. Cavazzana, P. Scarin, G. Serianni, R. J. Maqueda, and D. P. Stotler. Study of statistical properties of edge turbulence in the national spherical torus experiment with the gas puff imaging diagnostic. *Physics of Plasmas*, 14(10):102305, 2007.
- [72] G.S. Xu, V. Naulin, W. Fundamenski, C. Hidalgo, J.A. Alonso, C. Silva, B. Goncalves, A.H. Nielsen, J. Juul Rasmussen, S.I. Krasheninnikov, B.N. Wan, M. Stamp, and JET EFDA Contributors. Blob/hole formation and zonal-flow generation in the edge plasma of the jet tokamak. *Nuclear Fusion*, 49(9):092002, 2009.
- [73] Y. Xu, R. R. Weynants, S. Jachmich, M. Van Schoor, M. Vergote, P. Peleman, M. W. Jakubowski, M. Mitri, D. Reiser, B. Unterberg, and K. H. Finken. Influence of the static dynamic ergodic divertor on edge turbulence properties in textor. *Phys. Rev. Lett.*, 97:165003, Oct 2006.
- [74] B Nold, G D Conway, T Happel, H W Mller, M Ramisch, V Rohde, U Stroth, and the ASDEX Upgrade Team. Generation of blobs and holes in the edge of the asdex upgrade tokamak. *Plasma Physics and Controlled Fusion*, 52(6):065005, 2010.
- [75] P.A. Schneider, E. Wolfrum, R.J. Groebner, T.H. Osborne, M.N.A. Beurskens, M.G. Dunne, B. Kurzan, T. Pitterich, E. Viezzzer, the ASDEX Upgrade Team, the DIII-D Team, and the JET EFDA Contributors. Analysis of temperature and density pedestal gradients in aug, dIII-d and jet. *Nuclear Fusion*, 53(7):073039, 2013.
- [76] Boris Borisovich Kadomtsev. Plasma turbulence. *New York: Academic Press*, 1965, 1, 1965.
- [77] J Citrin, J Garcia, T Grler, F Jenko, P Mantica, D Told, C Bourdelle, D R Hatch, G M D Hogeweij, T Johnson, M J Pueschel, and M Schneider. Electromagnetic stabilization of tokamak microturbulence in a high- regime. *Plasma Physics and Controlled Fusion*, 57(1):014032, 2015.
- [78] Gregory W. Hammett and Francis W. Perkins. Fluid moment models for landau damping with application to the ion-temperature-gradient instability. *Phys. Rev. Lett.*, 64:3019–3022, Jun 1990.

- [79] M. A. Dorf, M. R. Dorr, J. A. Hittinger, R. H. Cohen, and T. D. Rognlien. Continuum kinetic modeling of the tokamak plasma edge. *Physics of Plasmas*, 23(5):056102, 2016.
- [80] M. A. Dorf, R. H. Cohen, M. Dorr, J. Hittinger, and T. D. Rognlien. Progress with the cogent edge kinetic code: Implementing the fokker-planck collision operator. *Contributions to Plasma Physics*, 54(4-6):517–523, 2014.
- [81] M. A. Dorf, R. H. Cohen, M. Dorr, T. Rognlien, J. Hittinger, J. Compton, P. Colella, D. Martin, and P. McCorquodale. Simulation of neoclassical transport with the continuum gyrokinetic code cogent. *Physics of Plasmas*, 20(1):012513, 2013.
- [82] M. A. Dorf, R. H. Cohen, J. C. Compton, M. Dorr, T. D. Rognlien, J. Angus, S. Krasheninnikov, P. Colella, D. Martin, and P. McCorquodale. Progress with the cogent edge kinetic code: Collision operator options. *Contributions to Plasma Physics*, 52(5-6):518–522, 2012.
- [83] T. S. Hahm. Nonlinear gyrokinetic equations for turbulence in core transport barriers. *Physics of Plasmas*, 3(12):4658–4664, 1996.
- [84] Donald Gary Swanson. *Plasma waves*. Academic Press, 1989.
- [85] Anatolii Borisovich Mikhailovskii. *Electromagnetic instabilities in an inhomogeneous plasma*, volume 1. CRC Press, 1992.
- [86] PB Snyder, GW Hammett, and W Dorland. Landau fluid models of collisionless magnetohydrodynamics. *Physics of Plasmas*, 4(11):3974–3985, 1997.
- [87] MV Umansky, AM Dimits, I Joseph, JT Omotani, and TD Rognlien. Modeling of tokamak divertor plasma for weakly collisional parallel electron transport. *Journal of Nuclear Materials*, 463:506–509, 2015.